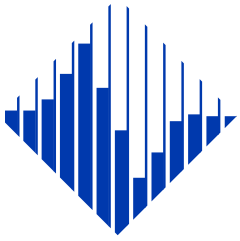

PACIFIC EARTHQUAKE ENGINEERING
RESEARCH CENTER

Correlation of Ground Motion Duration with Spectral Acceleration and Implications for Expected Bridge Performance

Maria Camila Lopez Ruiz
Department of Civil and Environmental Engineering
University of California, Berkeley, California

Micaela Largent
Slate Geotechnical Consultants, Inc.

Tracy Becker
Department of Civil and Environmental Engineering
University of California, Berkeley, California

Jennie Watson-Lamprey
Slate Geotechnical Consultants, Inc.

PEER Report No. 2024/09
Pacific Earthquake Engineering Research Center
Headquarters at the University of California, Berkeley
October 2024

PEER 2024/09
October 2024

Correlation of Ground Motion Duration with Spectral Acceleration and Implications for Expected Bridge Performance

Maria Camila Lopez Ruiz

Department of Civil and Environmental Engineering
University of California, Berkeley, California

Micaela Largent

Slate Geotechnical Consultants, Inc.

Tracy Becker

Department of Civil and Environmental Engineering
University of California, Berkeley, California

Jennie Watson-Lamprey

Slate Geotechnical Consultants, Inc.

PEER Report 2024/09
Pacific Earthquake Engineering Research Center
Headquarters at the University of California, Berkeley

October 2024

ABSTRACT

Construction or detailed evaluation of transportation infrastructure requires site-specific ground motions for input into nonlinear structural models. These site-specific ground motions are generally selected based on the magnitude, distance, and site condition of the recorded ground motion. A preliminary study performed by Slate Geotechnical Consultants found that duration and spectral acceleration are negatively correlated for large-magnitude earthquakes recorded on soft-soil sites (Vs30<360 m/s). This means that if the target spectral acceleration is above average, then the average duration associated with that ground motion should be below average for the scenario magnitude and distance. This ground motion duration correlation implies that the current state of the practice is overestimating the probability of collapse for structures. This project aims to improve the characterization of ground motion duration and evaluate how the improved characterization affects bridge fragilities used in the Performance-Based Earthquake Engineering (PBEE) framework. Numerical models for two prototype structures, a major toll bridge and a typical highway overpass, are developed using OpenSees. Using these models, the effect of ground motion duration is evaluated quantitatively following the PEER PBEE methodology.

Keywords: bridge performance, damage probability, hazard intensity, ground motion duration.

ACKNOWLEDGMENTS AND DISCLAIMER

This research study was funded by the State of California through the Transportation System Research Program of the Pacific Earthquake Engineering Research Center (PEER). The opinions, findings, conclusions, and recommendations expressed in this publication are those of the author(s) and do not necessarily reflect the view of PEER or the Regents of the University of California.

CONTENTS

LIST OF TABLES

LIST OF FIGURES

1 INTRODUCTION

The PEER performance-based earthquake engineering (PBEE) methodology has increasingly been used to evaluate the seismic risk to structural systems and link the use of structural demand parameters, typically used by designers, to desirable performance goals such as life-safety, economic losses and post-earthquake downtime (Moehle and Deierlein, 2004). Agencies and researchers have used PBEE to develop decision-making plans based on probabilistic analysis techniques such as fragility curves, which describe probabilities of exceeding design or performance criteria at different seismic intensity levels. The PBEE methodology begins by using the location and structural information (D) to do a site-specific probabilistic hazard analysis to find the probability of an intensity measure (IM). The resulting hazard information, sometimes in the form of ground motion time series, is used for structural analysis to determine the probability of an engineering demand parameter (EDP), like drifts or stresses, given the intensity measures. Then a damage analysis is conducted to relate the EDPs to a set of damage measures (DM). Finally, a loss analysis relates the DMs to a decision variable (DV) such as repair costs or downtime. Each stage of the framework influences the resulting prediction of the performance of a structure, e.g., a bridge, and, thus, the accuracy of the hazard analysis is a basis for the accuracy of the structural performance predictions. This report uses the PBEE methodology up to the damage analysis stage as shown in Figure 1.1 to evaluate the effects of accounting for ground motion duration in the hazard analysis on the structural performance of two cases study bridges: (1) a major toll bridge, and (2) a typical highway overpass.

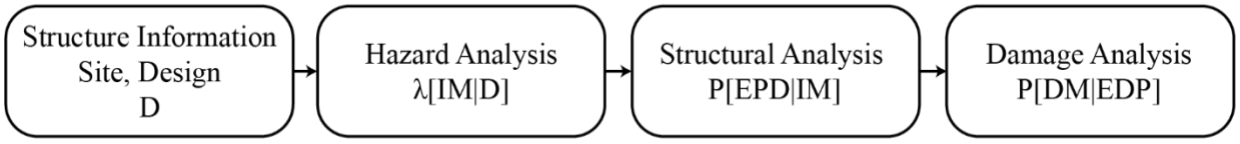

Figure 1.1 PBEE Methodology schematic up to damage analysis.

Current procedures for typical site-specific hazard analysis do not account for the effects of ground motion duration, and there are no requirements in design codes. Long-duration ground motions, however, can subject a structure to a large number of cycles and can result in accumulated damage when nonlinear behavior is present. Effects of ground motion duration on structural performance have been of interest to researchers for some time. Individual papers have found mixed results regarding the significance of ground motion duration on the structural response (Shome et al., 1998, Tremblay, 2003, Iervolino et al., 2006, Hancock and Bommer, 2007). Raghunandan and Liel (2013) found that ground motion duration has a measurable effect on the collapse capacity of reinforced concrete buildings, with longer duration leading to higher collapse probability when accounting for degradation in the numerical model. Barbosa et al. (2017) found that long-duration ground motions in steel frames tend to induce larger damage than short-duration ground motions

at high values of spectral acceleration based on a combined damage index that considers deformation and hysteretic energy dissipated. Chandramohan et al. (2016) investigated the effect of duration on the collapse capacity of a concrete bridge pier. They used two sets of records, both spectrally matched to the same response spectrum but with different average durations. They found that the collapse capacity was reduced by 17% for the concrete pier when long-duration ground motions were used. Hassan and Billah (2020) found that long-duration ground motions lead to higher damage of isolated bridges because the residual displacement increases.

Hancock and Bommer (2006) provide a thorough review of studies involving ground motion duration effects on structural damage. They found that the effect of duration is dependent on the damage metric used such as peak response, cumulative damage, or energy dissipated. The adequacy of a damage metric is dependent on the failure mode that is expected from the structure. While cumulative damage measures are recommended to capture all failure modes, peak response is simpler to implement and is often adequate if the failure mode expected is plastic hinge formation. Using peak responses results in higher expected damage when long duration ground motions are considered.

In cases where duration is deemed to be significant for the structural response, the state of the practice is to check the duration of the selected records against existing duration prediction models. Current duration prediction equations (DPE) describe the mean and variability of a duration metric (for a certain amount of energy released) given a set of predictor variables such as moment magnitude (Mw) and distance (R_{rup}, R_{jb}, R_x, etc.). These methods, such as Abrahamson and Silva (1996), Bommer et al. (2009), and Afshari and Stewart (2016), consider these predictor variables from the earthquake but do not consider the correlation between spectral acceleration and duration. Chapter 2 of this report presents the development of a ground motion duration correlation to spectral acceleration model that shows that duration and spectral acceleration are negatively correlated. This means that if the target spectral acceleration is above average (i.e. the ground motion is above the median deterministic scenario) then the average duration associated with that ground motion should be below average for the scenario magnitude and distance. Thus, the current state of the practice may be overestimating the probability of collapse for structures by introducing long-duration ground motions at high intensity measures. This is particularly true when methods such as incremental dynamic analysis, in which ground motions are scaled to larger and larger intensities, are used to generate damage or collapse fragility curves.

The main objective of this report is to answer two questions. (1) Does considering duration correlation in ground motion selection appreciably change the hazard input for analysis? (2) Does considering duration correlation change the predicted performance of bridges especially when doing incremental dynamic analysis? Chapters 3 and 4 of this report focus on developing the fragility curves, with and without considering duration correlation, for the major toll bridge and typical overpass following the PBEE methodology steps.

The major toll bridge has lead rubber bearing isolators on top of flexible piers, located in Southern California and a natural period of around 1.6 seconds. This bridge was selected because it can be affected by near fault conditions which are related to ground motion duration. The typical highway

overpass is a single-pier, two-span bridge located in Northern California with a period of about 0.5 seconds. A site-specific hazard analysis is done to obtain two sets of ground motions; one ignoring duration correlation and implementing an incremental dynamic analysis (IDA) (FEMA-P695, 2009, Vamvatsikos and Cornell, 2002), and one considering the duration correlation in the scaling using correlation coefficients presented in this report. Then a structural model is developed capturing material deterioration which is a critical feature to understand the effect of duration. Finally, damage states are determined based on pier drift and bearing shear strain to develop structural fragility curves for both sets of ground motions and used to compare the predicted performance at moderate and major damage levels.

2 GROUND MOTION DURATION CORRELATION

This study found that duration and spectral acceleration are negatively correlated. This means that if the target spectral acceleration is above average, then the average duration associated with that ground motion should be below average for the scenario magnitude and distance. As an example, and using the source characteristics in this study, an earthquake with a moment magnitude (Mw) of 7.0, a distance of 1 km, located on a soft-soil site with a target spectral acceleration 2.45 standard deviations from the median (ε of 2.45), Bommer et al. (2009) would predict a median 5 to 95% duration ($D_{5\text{-}95\%}$) of 13 sec without accounting for correlations. For a structure with a natural period of 0.2 sec and accounting for the correlations, the median $D_{5\text{-}95\%}$ becomes 9.5 sec. For comparison, a $D_{5\text{-}95}$ of 9.5 sec is approximately the mean value for a magnitude 6.6 Mw earthquake. If the correlation is ignored, the durations are overpredicted by the same amount as overpredicting the magnitude by 0.4 magnitude units.

The following sections outline the process of calculating the correlation between different duration parameters and pseudo-spectral acceleration (PSA) and applying this correlation through the selection of time histories. Ground motion prediction equations (GMPEs) and duration prediction equations (DPEs) describe the distribution of spectral acceleration and duration given a set of predictor variables such as Mw and distance (R_{rup}, R_{jb}, R_x, etc.), but do not address the correlation between pseudo-spectral acceleration and duration. This study calculates the correlations between four of the NGA-West2 GMPEs and three recent DPEs that estimate both $D_{5\text{-}75\%}$ (5-75% of normalized Arias Intensity) and $D_{5\text{-}95\%}$ (5-95% of normalized Arias Intensity).

2.1 CORRELATION

The following section outlines how the correlation between PSA and ground motion duration (both 5-75% and 5-95%) is calculated, using Equation (2.1). This study utilizes the NGA-West2 database (Ancheta et al., 2014) to calculate residuals for both PSA and ground motion duration. The NGA-West2 database consists of data from active crustal regions including California, Taiwan, Europe, China, and Japan. 21,539 records from approximately 600 earthquakes were used to assess the duration correlation. The database ranges from Mw of 2.99 to 7.9, and distance from 0.05 to approximately 1500 km. Figure 2.1 shows the database magnitude and distance ranges. Finally, the database has records from sites with V_{s30} values ranging from approximately 90 to 2100 m/s; Figure 2.2 shows the data dispersion. Most of the data falls in approximately the 200 to 500 m/s bins.

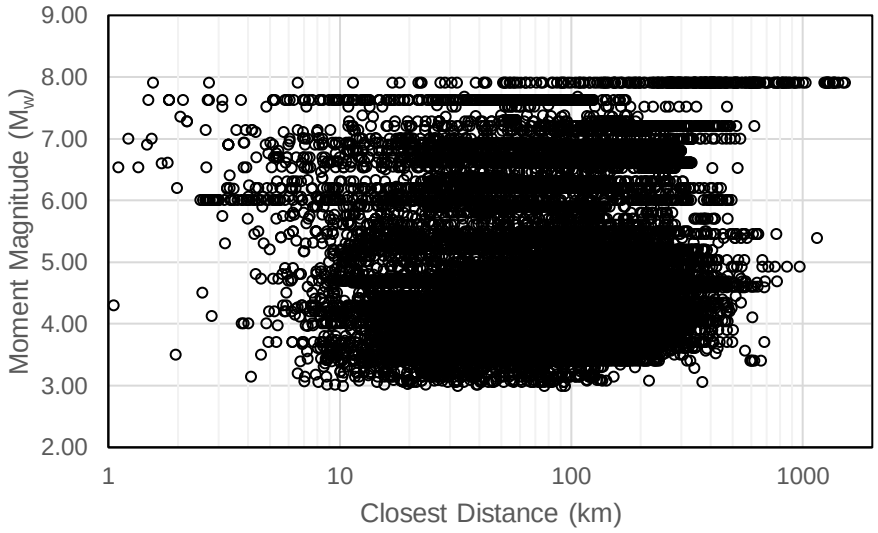

Figure 2.1 Magnitude Distance plot of available data in the NGA-West2 database

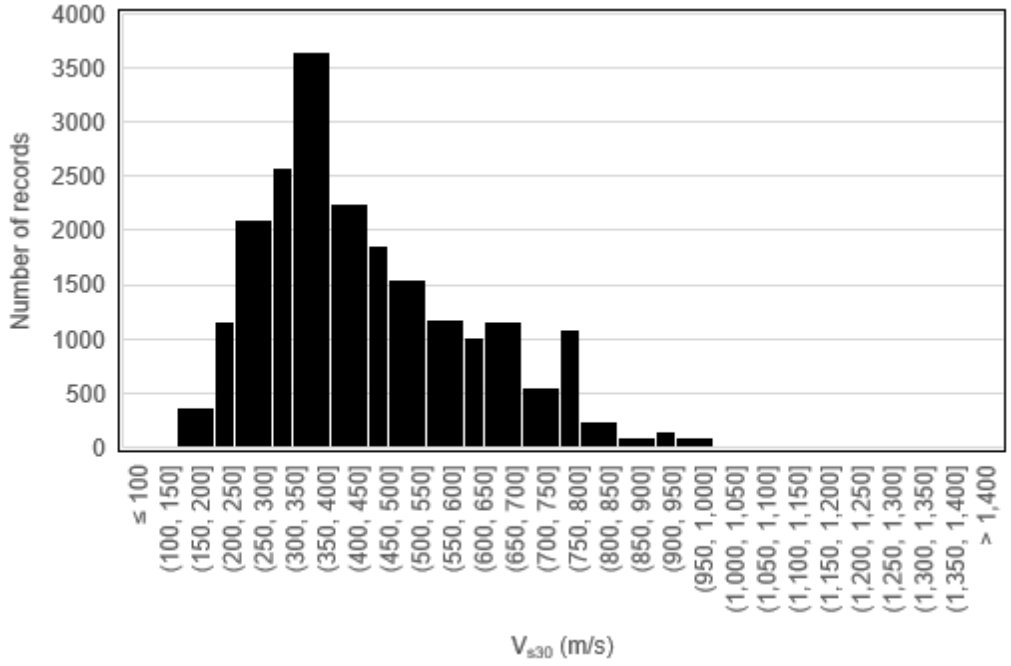

Figure 2.2 Range of V_{s30} values in the NGA-West2 database

In order to calculate correlation between two parameters, we need the residuals of the prediction equations for the two parameters. The PSA residuals were provided by the developers of the NGA-West2 GMPEs[1].

An important byproduct of the NGA-West2 relationships are the within-event and between-event residuals [2] which include an event term for each earthquake that estimates the degree to which the average parameter for a single earthquake falls above or below the median prediction. Separating the correlations between within-event and between-event residuals provides a better understanding of the mechanism producing the correlation. The intraevent (within-event) residuals, as given by the developers, were used to calculate the correlation between PSA and duration when available. The Afshari and Stewart (2016) DPE is the only one where the intraevent duration residuals were provided by the developers.[3]

The remaining residuals for duration need to be calculated. The NGA-West2 database of duration values was provided to us by the developers.[4] The mean duration values were first calculated for the NGA-West2 database using two DPEs: Abrahamson and Silva (1996) (AS96) and Bommer et al. (2009) (B09). Residuals were then calculated by taking the difference between the duration values provided in the NGA-West2 database and the mean duration values from the DPEs. An example of these residuals is shown in Figure 2.3

[1] Personal communication with Yousef Bozorgnia, 2021; Jon Stewart, 2021; Norm Abrahamson, 2021; Robert Youngs, 2021
[2] Personal communication with Abrahamson, 2020
[3] Personal communication with Jon Stewart, 2021
[4] Personal communication Yousef Bozorgnia, 2021

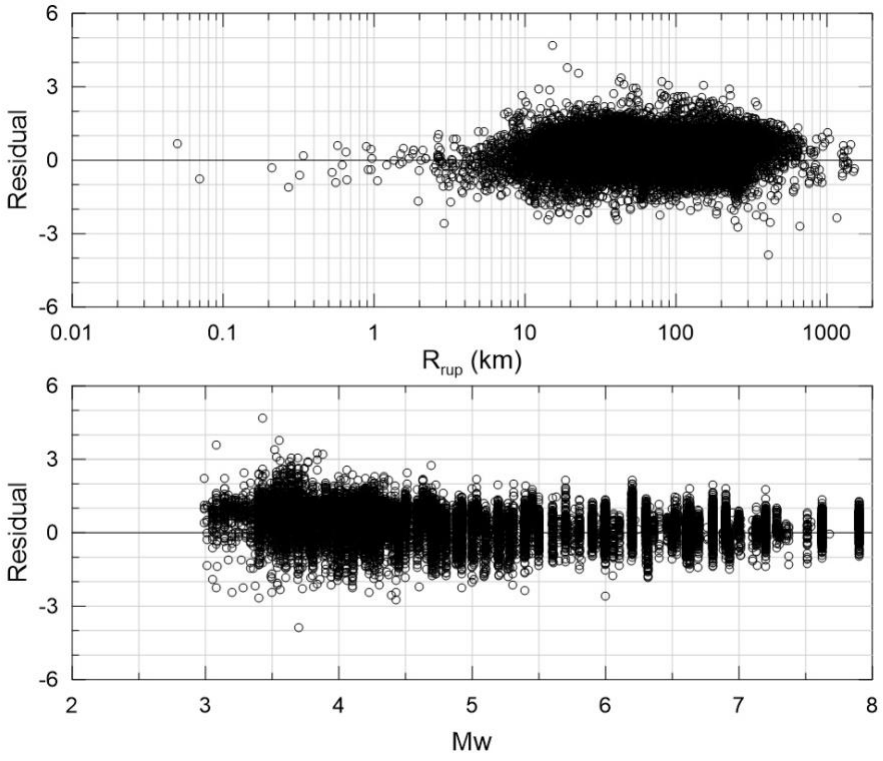

Figure 2.3 Residuals from Abrahamson and Silva, 1996, $D_{5\text{-}75\%}$ as a function of (a) rupture distance and (b) moment magnitude.

The correlation coefficient, ρ, was then calculated using Equation (2.1):

$$\boldsymbol{\rho} = \frac{\boldsymbol{n}\sum \boldsymbol{xy} - \sum \boldsymbol{x}\sum \boldsymbol{y}}{\sqrt{(\boldsymbol{n}\sum \boldsymbol{x^2} - (\sum \boldsymbol{x})^2)(\boldsymbol{n}\sum \boldsymbol{y^2} - (\sum \boldsymbol{y})^2)}} \tag{2.1}$$

where:
x is the intraevent residual for the GMPE;
y is the intraevent or total residual of the duration and;
n is the number of samples.

This calculation was performed for four GMPEs, three DPEs and two duration measures resulting in 24 sets of results. These correlation sets are calculated for periods between 0.01 sec and 10 sec. The 24 correlation sets are presented as a function of period in Figure 2.4 to Figure 2.6.

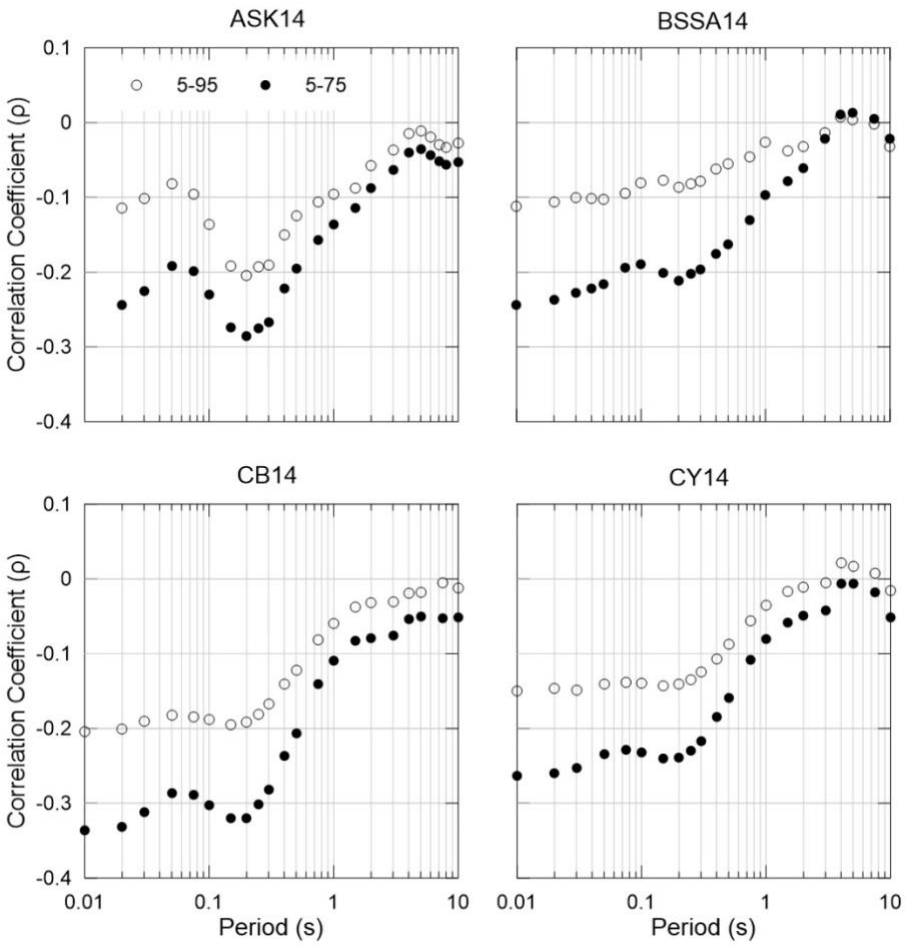

Figure 2.4 The correlation coefficients of the pseudo-spectral acceleration calculated using the four NGA-West2 relationships with the Abrahamson and Silva, 1996 duration model.

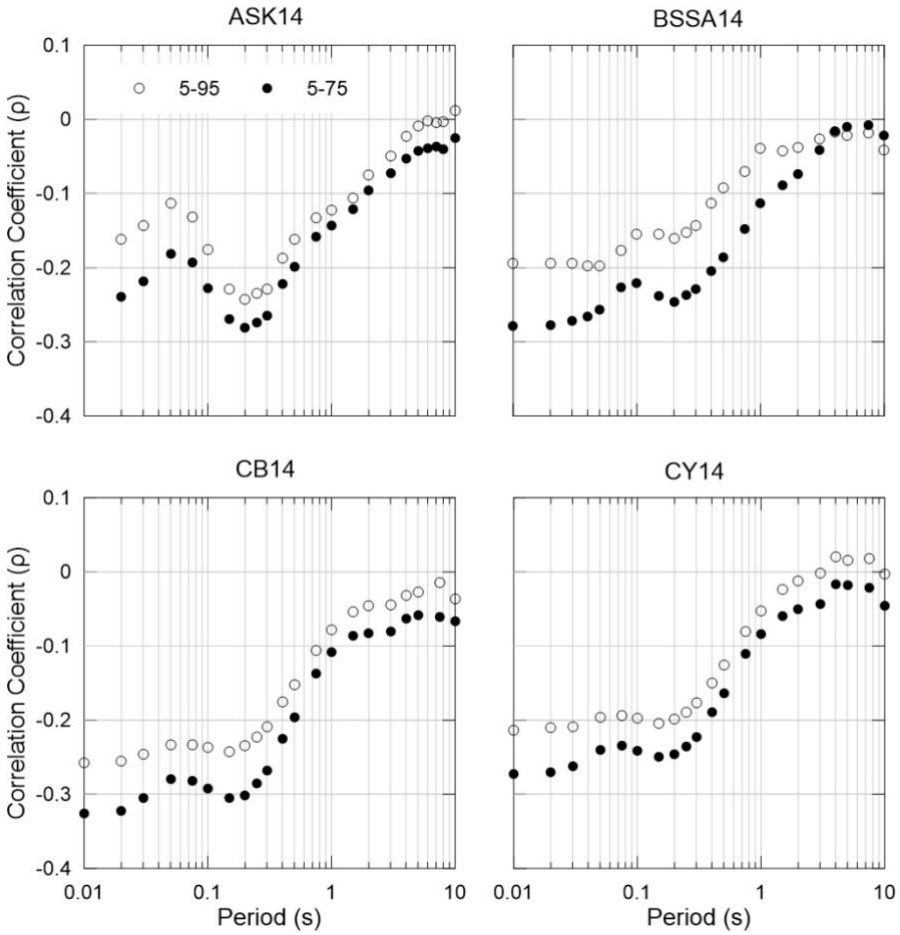

Figure 2.5 The correlation coefficients of the pseudo-spectral acceleration calculated using the four NGA-West2 relationships with the Bommer et al., 2009 duration model.

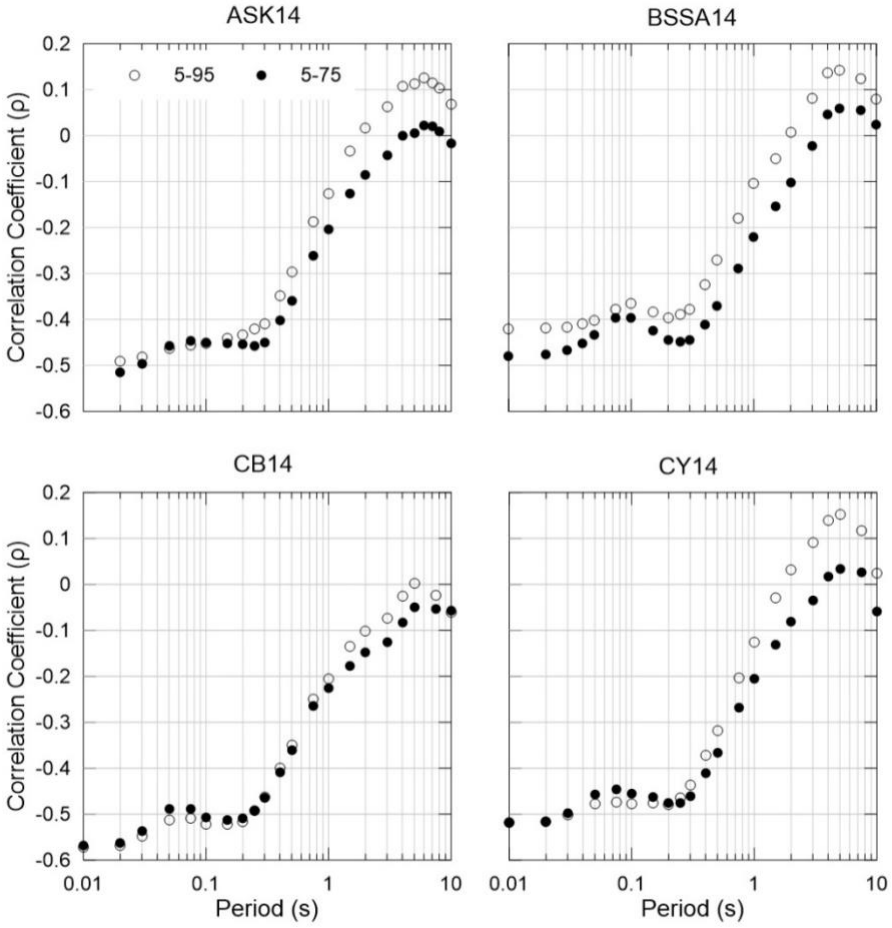

Figure 2.6 The correlation coefficients of the pseudo-spectral acceleration calculated using the four NGA-West2 relationships with the Afshari and Stewart, 2016 duration model.

Figure 2.7 and Figure 2.8 show the comparison of the three DPE's for $D_{5\text{-}75\%}$ and $D_{5\text{-}95\%}$ respectively. Overall, the $D_{5\text{-}75\%}$ relationships have a stronger negative correlation to PSA. The short periods were found to have the strongest correlation (largest absolute value of ρ), with the magnitude decreasing towards zero in the longer periods. The two earlier duration relationship (AS96 and B09), for which total duration residuals were used, have a smaller maximum correlation that the newer relationship for which intraevent residuals were used. Specifically, the two earlier relationships between PGA and 0.2 seconds, have correlation coefficients range from -0.19 to -0.3. At about 0.2 seconds these two DPE comparisons show a steady decrease (smaller magnitude ρ), moving to a correlation coefficient of zero. At 2.0 seconds there is little to no correlation between duration and pseudo-spectral acceleration in these two comparisons.

For the most recent duration relationship (AS16), for which intraevent residuals were used, there was a much stronger correlation. There is an almost constant ρ = -0.5 below 0.3 seconds and then the ρ slowly moves towards zero until about 2.0 seconds. Finally, there is a slightly positive correlation in the higher periods.

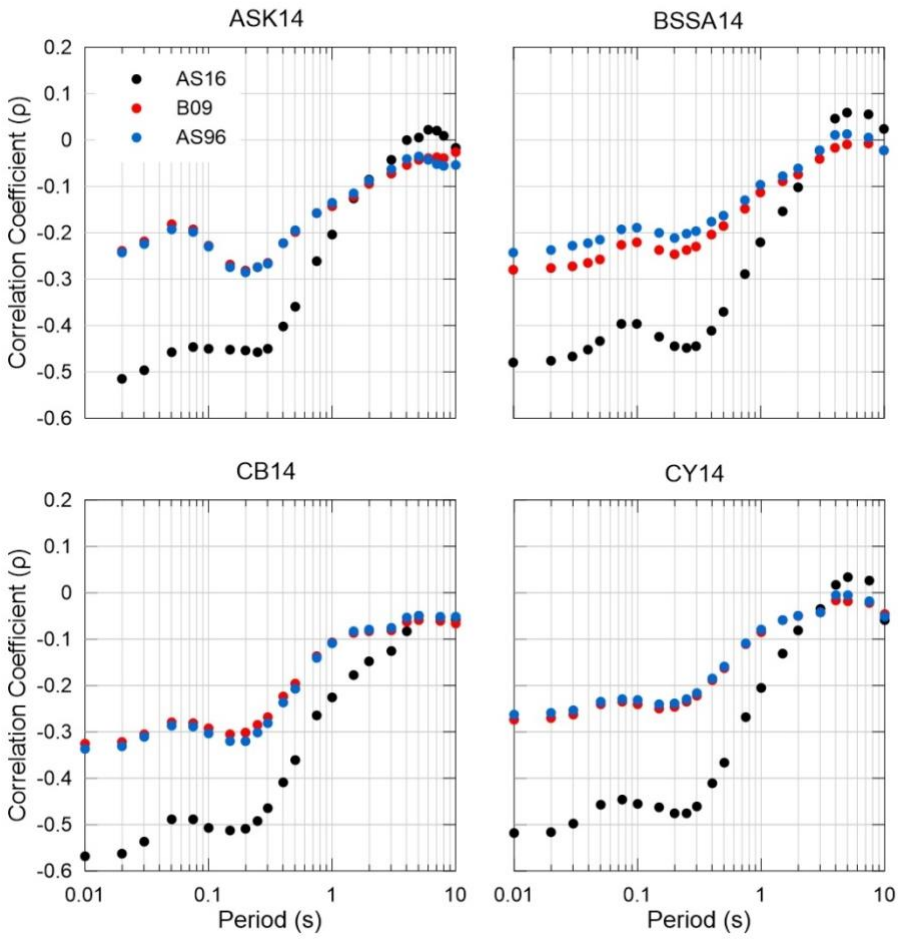

Figure 2.7. $D_{5\text{-}75\%}$ correlation coefficient comparison

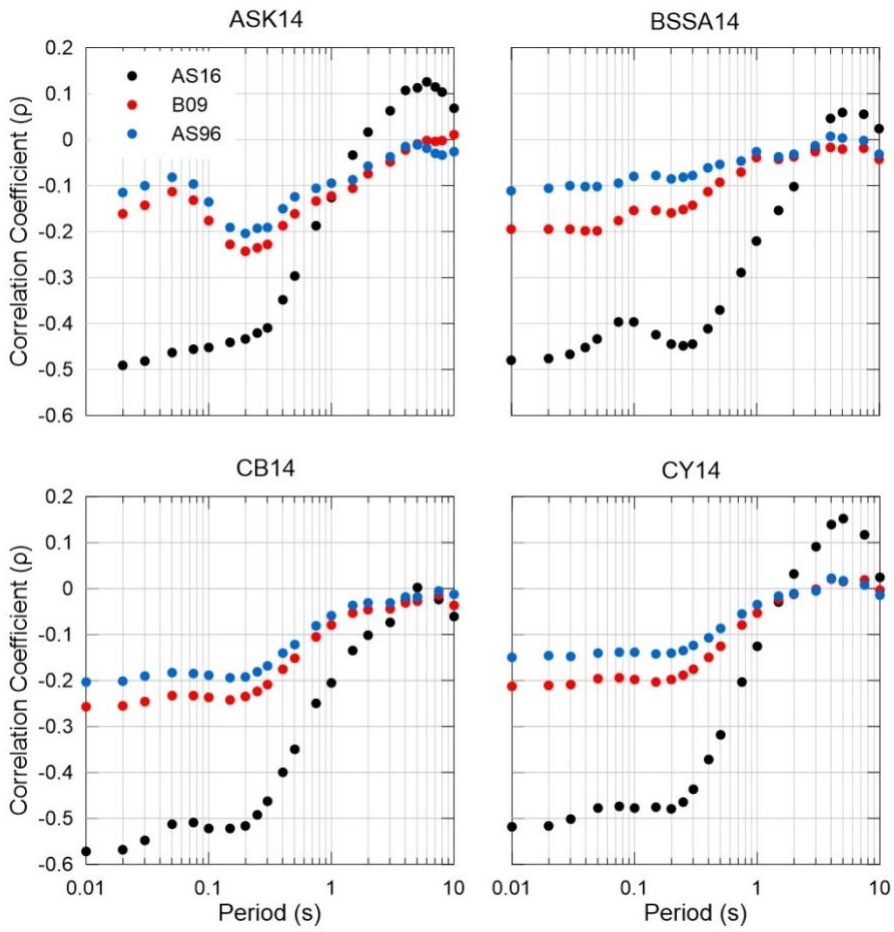

Figure 2.8. $D_{5\text{-}95\%}$ correlation coefficient comparison

To make the correlation values simpler to implement, the correlations are fit to an equation. A slightly modified version of the functional form from Baker and Jayaram (2008) was used as a starting point and least squares regression was used to solve for the coefficients. The functional form of the equation is given in Equations 2.2 through 2.6 below.

$$C_1 = 1 - \cos\left(\frac{\pi}{2} - x_1 \ln\left(\frac{T_{max}}{\max(T_{min}, x_2)}\right)\right) \tag{2.2}$$

$$C_2 = \begin{cases} 1 - x_3\left(1 - \frac{1}{1 + e^{x_4 T_{max}^{x_5}}}\right)\left(\frac{T_{max} - T_{min}}{T_{max} - x_5}\right) & if\ T_{max} < x_7 \\ 0 & otherwise \end{cases} \tag{2.3}$$

$$C_3 = \begin{cases} C_2 & T_{max} < x_1 \\ C_1 & otherwise \end{cases} \tag{2.4}$$

$$C_4 = C_1 + x_8(\sqrt{C_3} - C_3)(1 + \cos\left(\frac{\pi T_{min}}{x_1}\right)) \tag{2.5}$$

$$\rho = \begin{cases} \rho_0 \max(C_1, C_2, C_4) & T < T_3 \\ \rho_0 \min(C_1, C_2, C_4) & otherwise \end{cases} \tag{2.6}$$

*if C_1, C_2, or $C_4 > 1$ they are ignored in Equation 2.6

Where x_1 through x_8 are defined for each model in Table 2.1 and Appendix B. T_{max} and T_{min} are found by comparing T and T_2. T_2 is the period at which the correlation coefficient reaches its maximum magnitude (defined in Table 2.1) and T is the period for which the user is solving for. T_3 is the period at which the correlation changes from a maximum to a minimum to account for the change in slope. It is important to note that if C_1, C_2, and C_4 are above 1 they are ignored in the maximum or minimum in Equation 2.6.

Equations 2.2 through 2.5 are from Baker and Jayaram (2008), and the piecewise function in 2.6 was modified to fit the correlation coefficients within this study. In the original form, the authors present a larger piecewise depending on T_{min} and T_{max}. For this study a modified version is presented in Equation 2.6 where ρ is dependent on T_3 where the equation switches from taking a maximum value of the calculated coefficients to a minimum.

The curve fitting was performed for all 24 combinations and can be found in Appendix A.1. The four GMPE relationships are commonly equally weighted, and as such a regression was performed to provide the average of these correlations as shown in Table 1. These correlations are also shown in Figure 2.9 to Figure 2.14 When using the normalized coefficients, the correlation coefficient at T_2 (ρ_0) should then be multiplied by the normalized coefficient, to get the actual correlation at T. Figure 2.15 and Figure 2.16 show comparisons of the normalized correlation coefficients for $D_{5\text{-}75\%}$ and $D_{5\text{-}95\%}$ respectively. When the four GMPE comparisons are combined the trends between the three DPE normalized coefficients are similar.

It should be noted that this correlation is only applicable for shallow crustal earthquakes due to the use of the NGAWest2 database. This correlation may not be applicable to subduction earthquakes which are typically greater in magnitude and duration.

Table 1 Coefficients for the average correlation coefficients for the three DPE's

Coefficient	AS96			B09			AS16		
	$D_{5\text{-}75\%}$	$D_{5\text{-}95\%}$ (T ≤ 0.2 sec)	$D_{5\text{-}95\%}$ (T > 0.2 sec)	$D_{5\text{-}75\%}$	$D_{5\text{-}95\%}$ (T ≤ 0.2 sec)	$D_{5\text{-}95\%}$ (T > 0.2 sec)	$D_{5\text{-}75\%}$	$D_{5\text{-}95\%}$ (T ≤ 0.2 sec)	$D_{5\text{-}95\%}$ (T > 0.2 sec)
T_2	0.01	0.2		0.01	0.2	0.2	0.01	0.01	0.01
T_3	0.4			10	0.4		10	0.4	
ρ_0	-0.2726	-0.1558		-0.2807	-0.2090		-0.5217	-0.5008	
x_1	0.270	0.1752	0.4075	0.4499	0.1175	0.4000	0.477	0.08	0.3266
x_2	0.110	0.07	0.1297	0.1795	0.07	0.165	0.25	0.12	0.2
x_3	0.15	0.0883		0.094	0.0676		0.1077	0.07	
x_4	300	538.1269		853.357	847.9955		345.3948	100	
x_5	9.00	16.4533		26.42	26.011		17.3465	5	
x_6	0.015	0.0199		0.0199	0.02		0.0252	0.0099	

x_7	0.60	0.1476		0.2	0.2		0.2001	0.0951	
x_8	0.60	0.7719	0.4495	0.321	1.0000	-0.1091	0.0225	-0.7	-0.5393

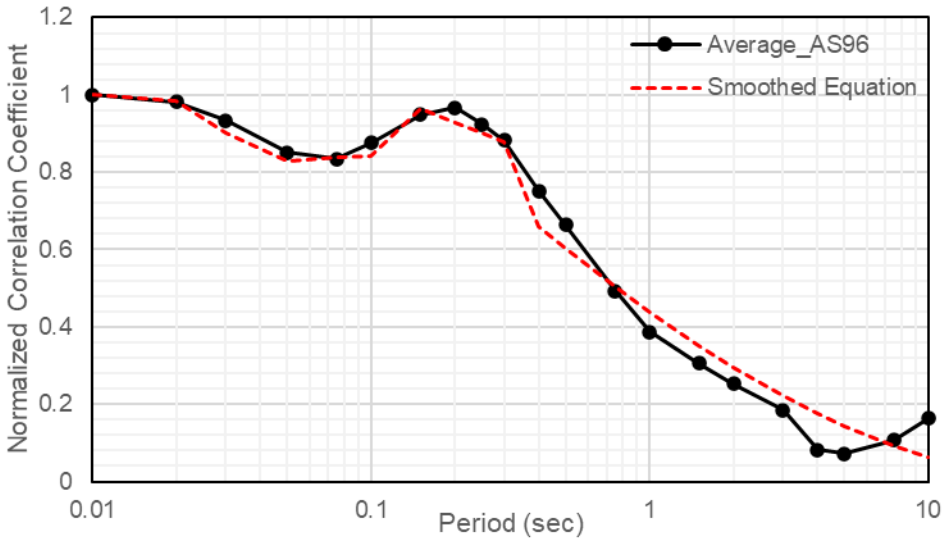

Figure 2.9 Normalized Correlation Coefficients for the Average of the four GMPEs and AS96, for the D_{5-75}

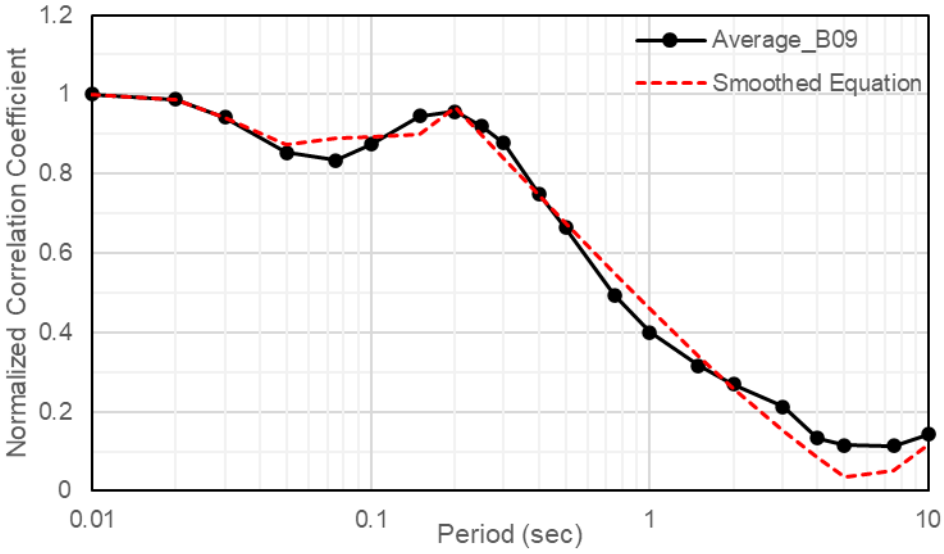

Figure 2.10 Normalized Correlation Coefficients for the Average of the four GMPEs and B09, for the D_{5-75}

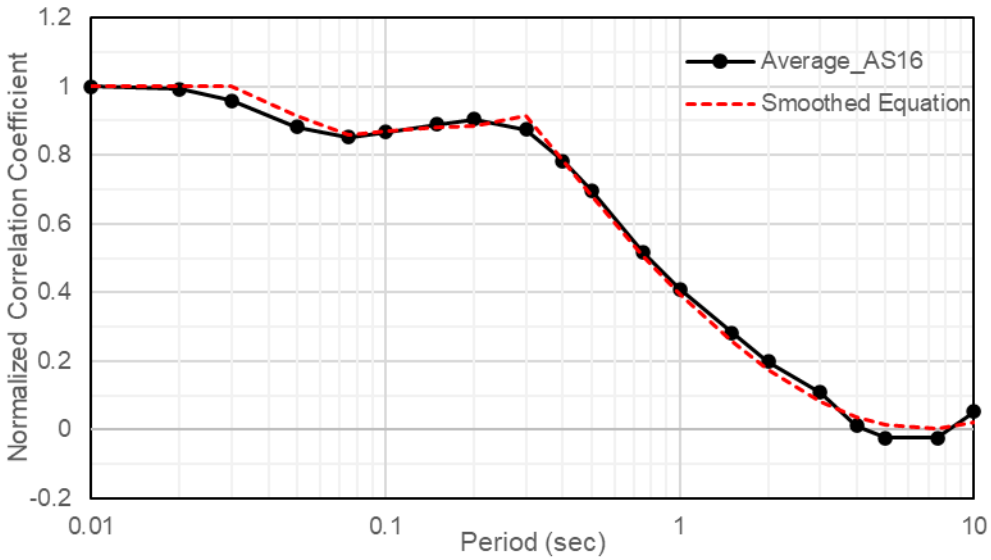

Figure 2.11 Normalized Correlation Coefficients for the Average of the four GMPEs and AS16, for the D_{5-75}

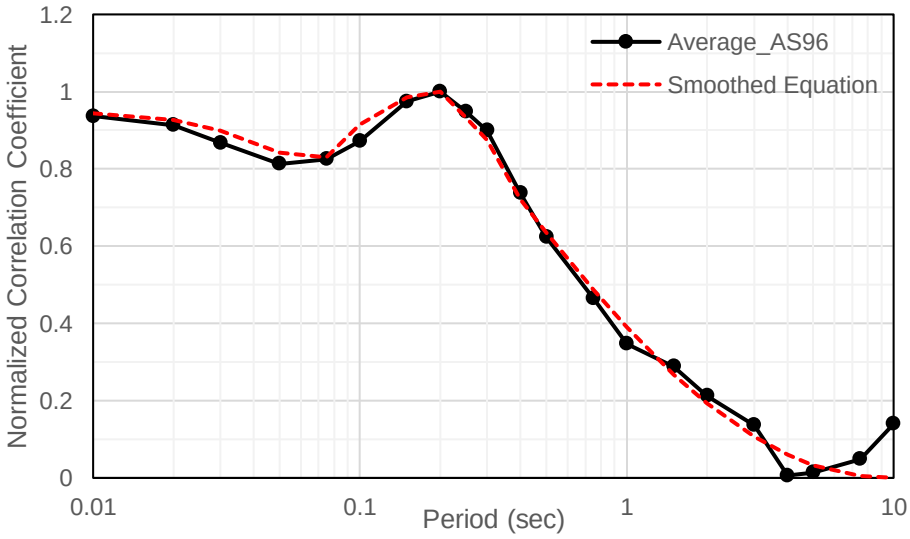

Figure 2.12 Normalized Correlation Coefficients for the Average of the four GMPEs and AS96, for the D_{5-95}

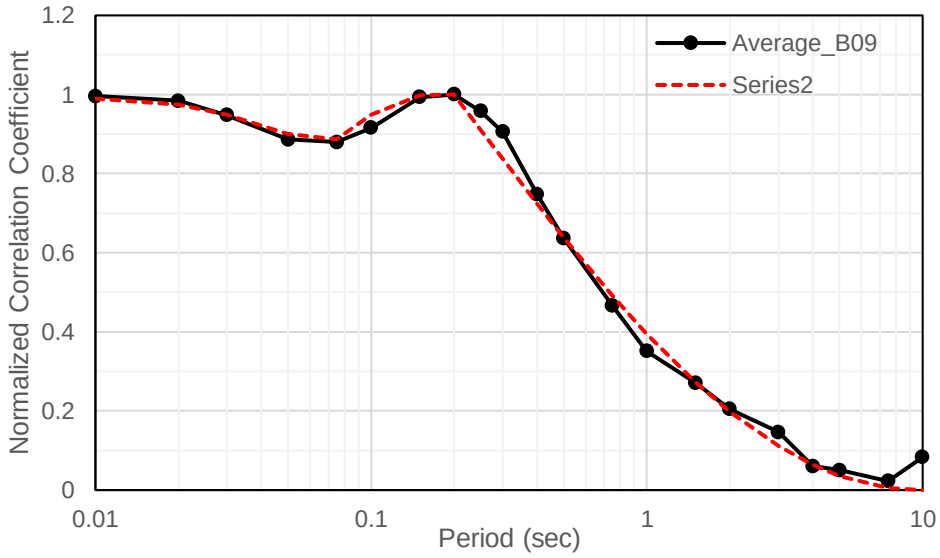

Figure 2.13 Normalized Correlation Coefficients for the Average of the four GMPEs and B09, for the D5-95

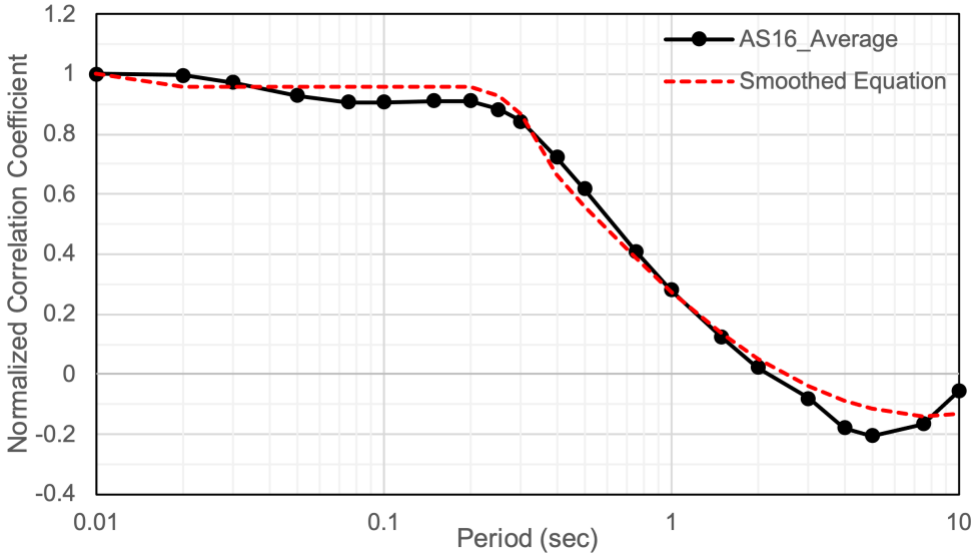

Figure 2.14 Normalized Correlation Coefficients for the Average of the four GMPEs and AS16, for the D5-95

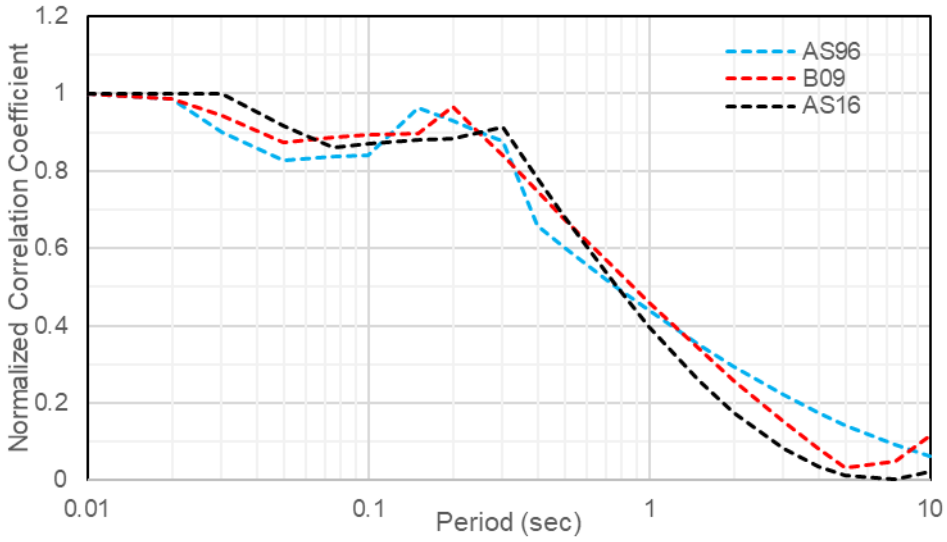

Figure 2.15 Comparison of three DPE smoothed correlation coefficients for D5-75%

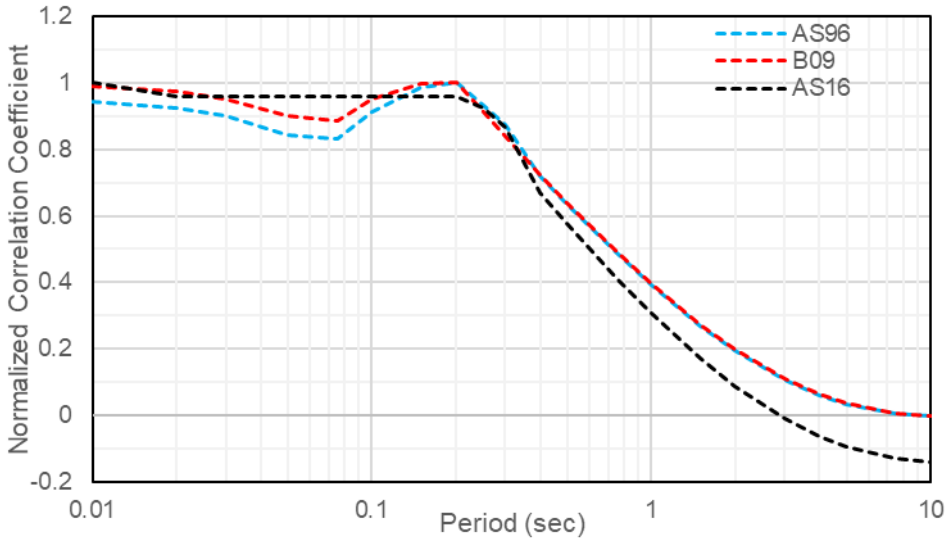

Figure 2.16. Comparison of three DPE smoothed correlation coefficients for D5-95%

3 GROUND MOTION SELECTION METHODOLOGY

Within this study, two sites were used to explore the impact of the duration correlation on structural fragility. The first site is a major toll bridge in Southern California and the second is a smaller highway overpass in Northern California. For each site, a probabilistic hazard analysis was performed and suites of time histories selected (both correlated to duration and not correlated). These time histories were then used in structural models explained further in Chapters 4 and 5.

3.1 HAZARD ANALYSIS

A probabilistic seismic hazard analysis (PSHA) was performed to characterize earthquake ground motions that have a likelihood of being exceeded at the project site at specific time intervals. The PSHA for this study generally follows the approach first developed by (Cornell, 1968) with the inclusion of parameters for randomization and the consideration of epistemic uncertainty.

A Poisson process is used to compute how often a specified level of ground motion will be exceeded at a site. The PSHA computes the annual number of events that produce a ground motion parameter, *Z*, that exceeds a specified level, *z*. This number of events per year, *n*, is also called the "annual frequency of exceedance," the inverse of which is called the "return period". The calculation of the annual frequency of exceedance, n, considers the rate of earthquakes of magnitudes 5 or greater, the rupture dimension of the earthquakes, the distance of the site relative to the earthquake source, and the attenuation of the ground motion from the earthquake rupture source to the site.

The annual rate of exceedance of a ground motion test value, z, from a source, I, for a given earthquake that occurred on the source, i, is given by the equation:

$$\nu_i(Z > z) = N_i(E_i)P(Z > z|E_i) \quad (1)$$

where:

E_i is the given earthquake from source *i*, with a known magnitude and distance; and
$N_i(E_i)$ is the annual rate of the given earthquake per year from source *i*

The PSHA calculations were performed using the computer program Haz45.2 developed by Norm Abrahamson[5] and modified by Slate to include the Third Uniform California Earthquake Rupture Forecast (UCERF3) (Field et al., 2013). This program was validated as part of the Pacific Earthquake Engineering Research (PEER) Center Probabilistic Seismic Hazard Analysis Code Verification Project (Hale et al., 2018).

[5] Abrahamson, N. (2017). "HAZ" v45.2. Contributors: Hale, C.; Kottke, A.; Hsieh, P.S.; Murphy, D.G. and Gregor, N.J.

3.1.1 Seismic Source Characterization

The seismic source characterization is based on UCERF3 (Field et al., 2013). The UCERF3 project was a multi-year initiative to provide an authoritative estimate of the magnitude, location, and time-averaged frequency of potentially damaging earthquakes in California. This project addresses important issues not previously implemented such as relaxing fault segmentation assumptions and multi-fault ruptures.

The UCERF3 model defines the long-term rate of all possible earthquake ruptures above a minimum magnitude of 5. Two alternative fault models give the spatial geometry of the larger, active faults throughout the region, with the alternative models representing the epistemic uncertainty in the fault system geometry. Each model comprises three types of sources: supraseismogenic, subseismogenic, and off-fault sources. Supraseismogenic sources have rupture dimensions that are larger than the seismogenic depth occurring on explicitly modeled faults, subseismogenic sources have rupture dimensions that are smaller than the seismogenic thickness, and off-fault ruptures are those not associated with any known fault. Supraseismogenic sources are modeled using fault segments with lengths that are approximately equal to the seismogenic depth. These fault segments are then linked to create larger fault ruptures. The subseismogenic sources and off-fault sources are modeled using gridded seismicity. The two alternative UCERF3 source models, referred to as Fault Model 3-1 and 3-2 in the UCERF3 documentation, are implemented in this analysis and have 253,706 and 305,709 unique "scenario" ruptures respectively. Input files for these models were provided via personal email communication with Kevin Milner (2018).[6]

3.1.2 Ground Motion Model

The ground motion is characterized by using a suite of four ground motion prediction equations (GMPEs) from the Next Generation Attenuation Relationships for Western US (NGA-West2) Project. The NGA-West2 models were developed as part of a multi-year effort to improve attenuation models for active tectonic regions such as California. This project addressed important issues such as: modeling of directionality, verification for recent small, moderate and large magnitude events, and evaluation of soil amplification factors.

The GMPEs selected for this analysis were Abrahamson et al. (2014), Boore et al. (2014), Campbell and Bozorgnia (2014) and Chiou and Youngs (2014). The GMPEs were given equal weight. The NGA-West2 models use the average shear wave over the top thirty meters (V_{S30}) as an index of site response. Basin response is included in the model by the depth to a shear wave velocity of 1,000 m/s ($Z_{1.0}$) and 2,500 m/s ($Z_{2.5}$).

[6] Personal communication with Kevin Milner, 2018.

3.2 GENERAL SELECTION OF SEED TIME HISTORIES

The specific earthquake source parameters that represent the dominant earthquake scenarios in the seismic hazard were used in the selection of seed time histories. Criteria used to sort, prioritize, and select seed time histories for the bedrock analysis spectra from the PEER Center NGA-West2 Ground Motion Database are specified in Chapters 4 and 5.

The magnitude and distance ranges presented are based on the deaggregation results from the PSHA. The predicted duration parameters were used to select the time histories and will be described in further detail later in subsequent sections of this report.

Fourteen (14) sets (two uncorrelated and twelve correlated) of two-component seed time histories were selected from the PEER Center NGA-West2 Ground Motion Database at their as-recorded orientations. The seed time histories were selected to roughly match the dominant scenarios from the PSHA deaggregation using the selection criteria listed above, and with consideration of overall spectral shape and scaling factor. Descriptions of how duration was accounted for in these suites can be found in the following sections.

To test the impact that these correlation coefficients have on the probability of collapse, multiple suites of time histories were chosen using both the state of practice for accounting for duration and using the correlation models in this report. The first suite was chosen using non-correlated durations, magnitude, distance, and other secondary earthquake parameters. Then six additional suites were selected based on a scaled uniform hazard spectra scaled to different scale factors. These suites are then used in a structural model to predict the probability of collapse. This framework was repeated for two sites, one in Northern California and another in Southern California.

3.3 SPECTRAL MATCHING - HORIZONTAL

Spectral modification was performed by amplitude scaling and spectrally-matching over a period range of PGA to 5.0 sec. By performing spectral matching, we are able to isolate the difference between the suites of records to those of their non-stationary properties (aka duration).

Each suite of eleven pairs of two-component horizontal recorded time histories (as-recorded) were scaled to the target PGA and then spectrally matched to the Uniform Hazard Spectra (UHS) using RSPMatch.[7] RSPMatch was originally developed by Abrahamson (1992) as a modification to the method by Lilhanand and Tseng (1988). The approach developed by Lilhanand and Tseng (1988) makes small wavelet adjustments to the time history; those adjustments are used to make non-stationary modifications to the seed time history. The introduction of non-stationary modifications allows for modification of the time history while maintaining non-stationary properties.

[7] 2018 release, executable received from N. Abrahamson via email November 12, 2018

The 2018 release of RSPMatch allows for the component-to-component variability of the two horizontal components to be maintained. This is accomplished within the program by calculating the ratio of each component to the geomean of the time series and multiplying this ratio by the target to achieve a component-specific target.

Following the spectral matching process, each time history was baseline corrected. Baseline correction is used to remove any long period drift that might be added to the time history during the spectral matching process. To perform the baseline correction, a polynomial is fit to the acceleration record such that the acceleration, velocity, and displacement resolve to zero at the end of the record. Final response spectra were calculated for each time history component once spectral matching was complete.

4 CASE STUDY 1: MAJOR TOLL BRIDGE

The first bridge considered is based on the design and location of the San Diego-Coronado bridge which underwent a structural seismic retrofit in 1999. As part of this retrofit, lead rubber bearings (LRBs) were installed on 13 of its piers while the remaining piers have rigid connections to the deck. The Coronado bridge has spans of about 200 ft over the isolated span, and the piers have heights of up to 160 ft. This bridge was selected for the case study as a major toll bridge due to its long spans and tall piers making it more flexible than a typical highway bridge. The major toll bridge with flexible piers and a natural period of around 1.6 seconds. The location of the bridge is shown in Figure 4.1. An overview photo of the bridge and a close-up of a top of a pier with a lead rubber bearing are shown in Figure 4.2.

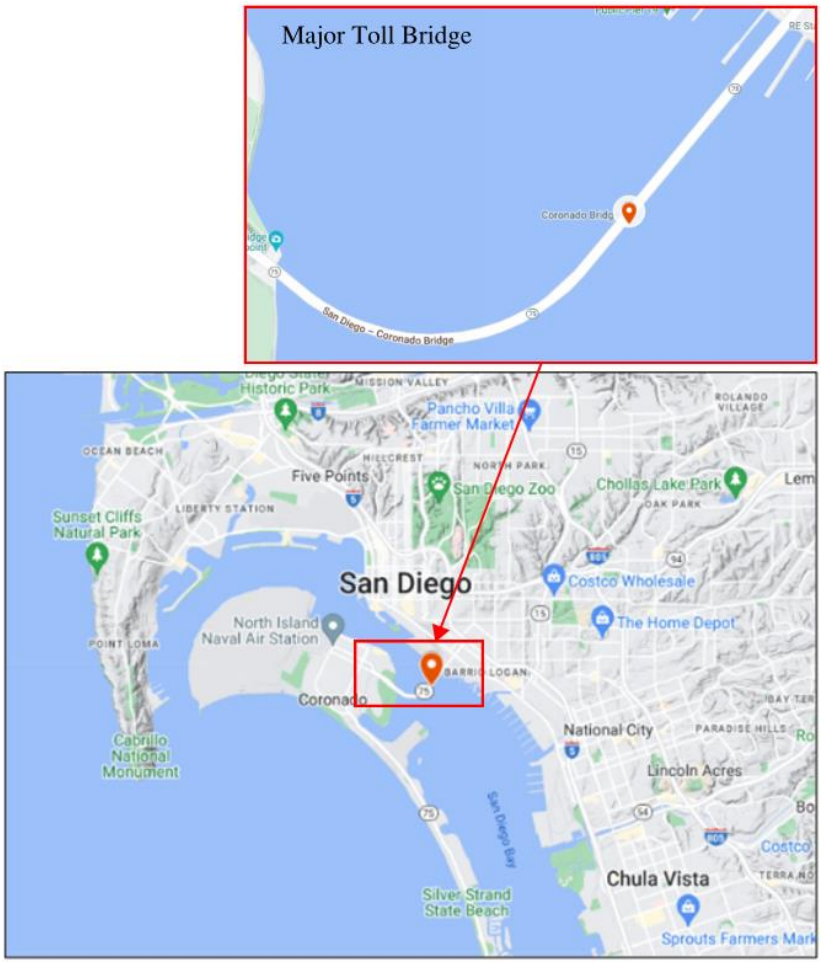

Figure 4.1 Major toll bridge location in Southern California showing curved span on plan view.[8]

[8] Google Maps. 2023. [Coronado bridge] [Online]. Available: https://www.google.com/maps/@32.6950075,-.

The PBEE methodology is followed through to the damage analysis phase to evaluate the performance of two bridge models to compare the performance of each structure using more traditional IDA and the proposed hazard selection methodology using a correlated spectral duration and acceleration. Fragility curves for each case are presented to compare the expected bridge performance under both ground motion selection methods.

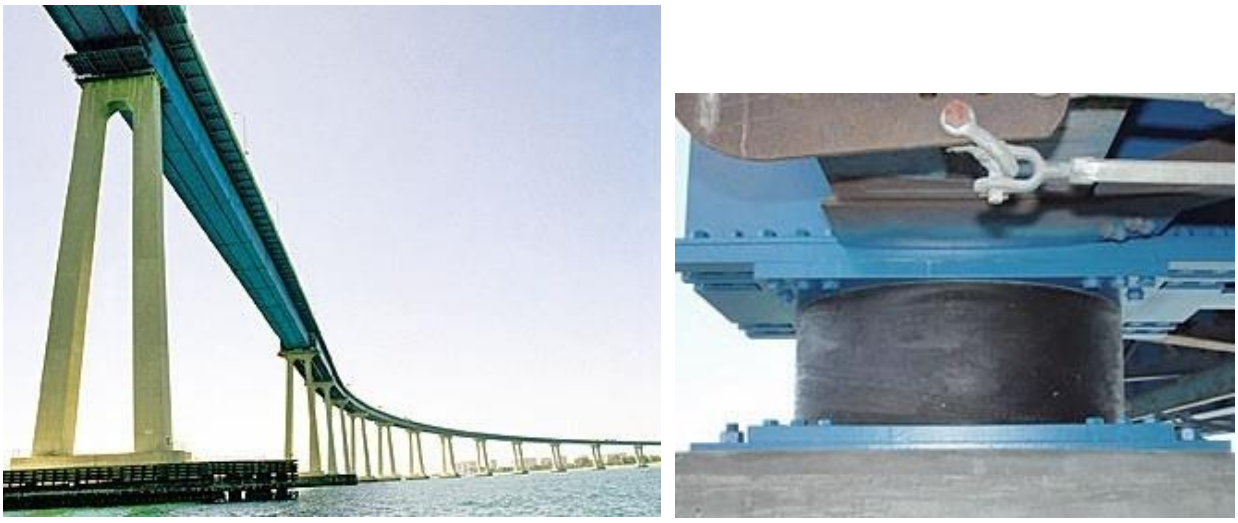

Figure 4.2 Major toll bridge picture of flexible piers and top of pier lead rubber bearing.[9]

4.1 GROUND MOTION SELECTION

4.1.1 Hazard Analysis

The UHS for a return period of 2,475 years (corresponding to a 2% probability of exceedance in 50 years) was developed using the method outlined in Section 3.1 and is shown in Figure 4.3. Figure 4.4. depicts the deaggregation of the PSHA results for a V_{S30} of 300 m/s for the period of the bridge (1.6 seconds). The major toll bridge is dictated by a Mw 7.1 at 1 km according to the deaggregation results. These values were used in the deterministic analysis to calculate the ε for the duration correlation analysis (discussed later).

[9] Forell | Elsesser Engineers. San Diego Coronado Bay Bridge Seismic Retrofit [Online]. Available: https://forell.com/projects/transportation/coronado-bay-bridge-seismic-retrofit/ [Accessed May 23, 2023].

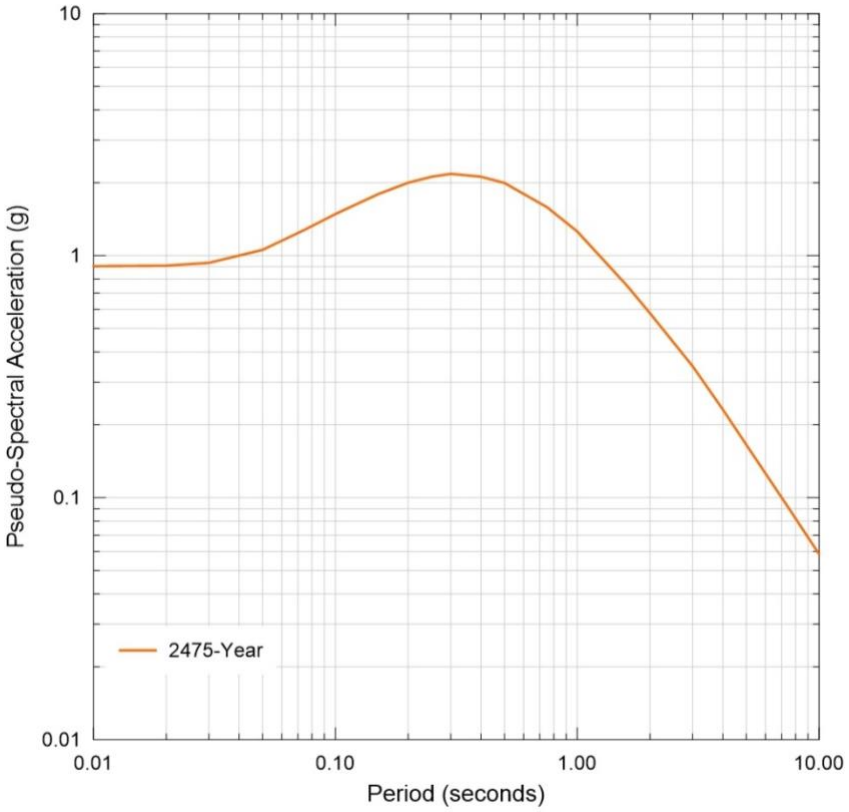

Figure 4.3. Uniform hazard spectra for a return period of 2,475 years (corresponding to a 2% probability of exceedance in 50 years, Maximum Considered Earthquake) for the major toll bridge location.

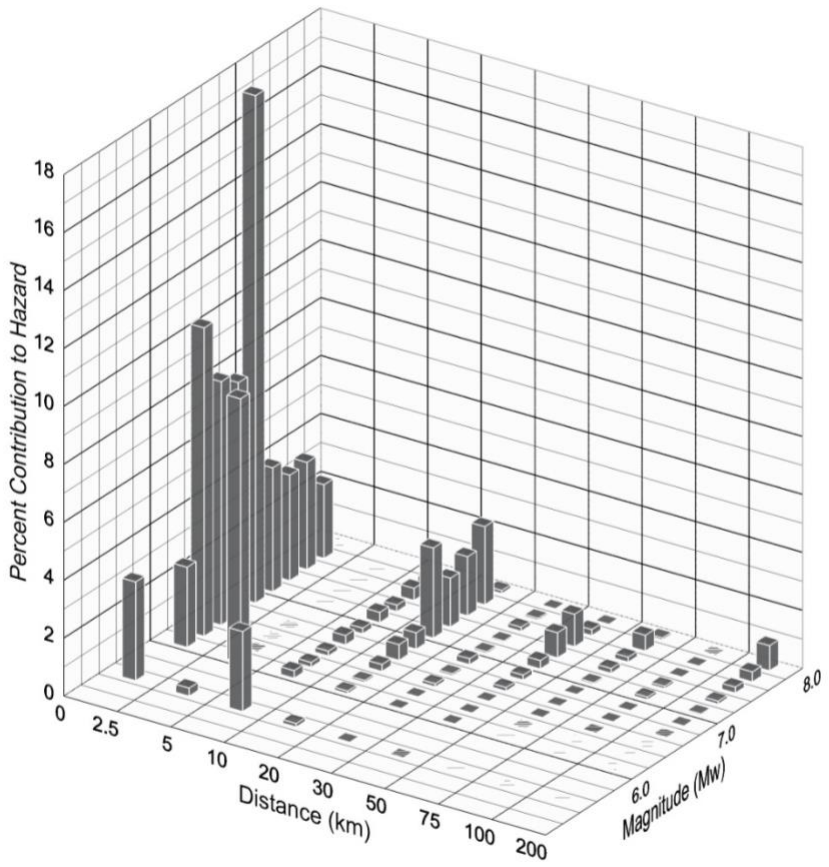

Figure 4.4. 2475-year return period hazard deaggregation at a period of 1.6 second showing near fault contribution.

4.1.2 General Selection of Seed Time Series

The specific earthquake source parameters that represent the dominant earthquake scenario in the seismic hazard were used in the selection of seed time series. Criteria used to sort, prioritize, and select seed time series for the bedrock analysis spectra from the PEER Center NGA-West2 Ground Motion Database included the following for all suites:

- Magnitude (M_w): 7.0 – 8.6;
- Rupture distance: 0 – 50 km;

4.1.3 Selection of Non-correlated Suite

The first suite was selected based on the mean duration values from the DPEs and the other parameters listed above. For the site the mean duration values from the DPEs are as follows:

- $D_{5\text{-}75}$: 6.0 seconds
- $D_{5\text{-}95}$: 13.0 seconds

The suite using these duration bounds is shown in Table 2.

Table 2 Non-correlated suite of time histories

RSN	Earthquake Name	Station Name	Mw	$D_{5\text{-}75\%}$ (sec)	$D_{5\text{-}95\%}$ (sec)
828	Cape Mendocino	Petrolia	7.0	6.5	17.7
1158	Kocaeli, Turkey	Duzce	7.5	6.1	11.8
1509	Chi-Chi, Taiwan	TCU074	7.6	13.3	19.7
1787	Hector Mine	Hector	7.1	7.6	11.7
3748	Cape Mendocino	Ferndale Fire Station	7.0	6.2	13.6
3934	Tottori, Japan	SMN002	6.6	6.7	15.6
3965	Tottori, Japan	TTR008	6.6	6.2	18.5
4031	San Simeon, CA	Templeton - 1-story Hospital	6.5	3.3	10.3
5818	Iwate, Japan	Kurihara City	6.9	6.5	15.1
6890	Darfield, New Zealand	Christchurch Cashmere High School	7.0	9.0	20.0
8063	Christchurch, New Zealand	Christchurch Botanical Gardens	6.2	4.8	11.4

4.1.4 Selection of Correlated Suites

The next six suites for each site were selected based on correlated duration bounds and scaled versions of the UHS. The correlation coefficient at the fundamental period of each bridge was used and applied through Equation (**4.1**), below.

$$\mu_{dur|Sa} = \mu_{dur} + \varepsilon\rho_{os}\sigma_{dur} \tag{4.1}$$

where,
$\mu_{dur}$is the mean duration from the DPE;
σ_{dur} is the standard deviation of the DPE;
ρ_{os} is the correlation coefficient at the period of the bridge (calcluated in Section 2);
ε is the number of standard deviations of the scaled UHS (at the period of the bridge) from the median ground motion; and
$\mu_{dur|Sa}$ is the correlated mean duration.

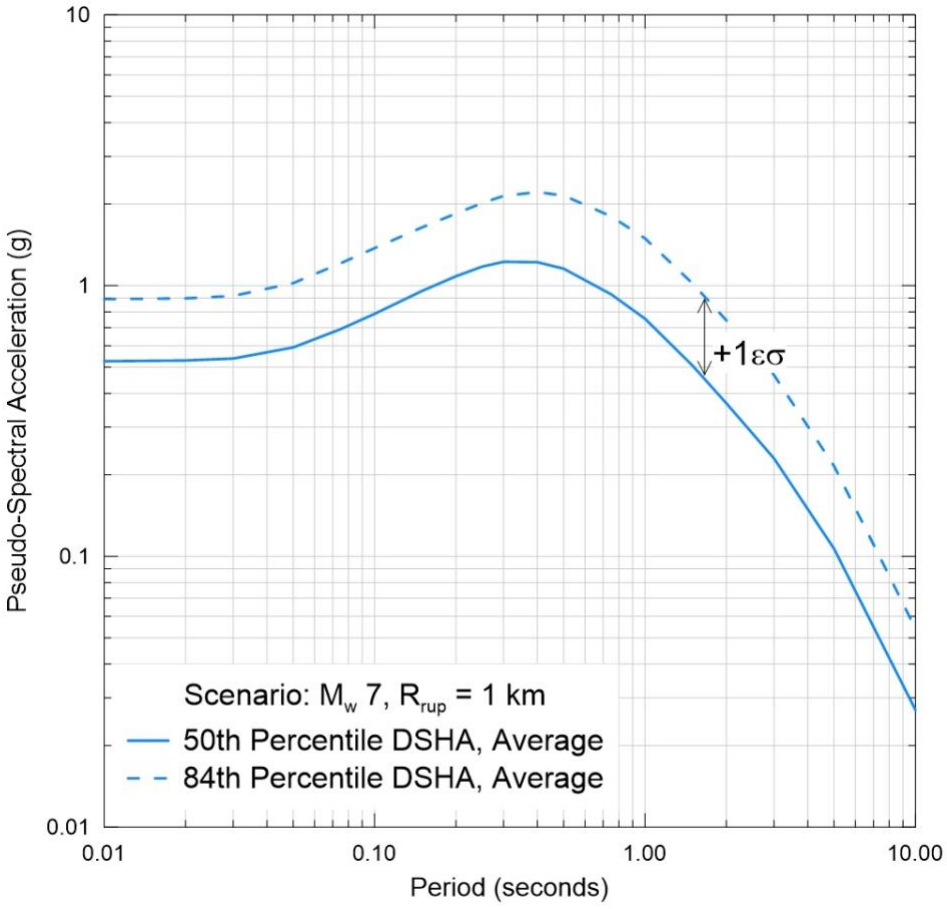

Figure 4.5. Deterministic spectra and depiction of epsilon for the Toll Bridge site

ε is calculated using the deaggregation results from the PSHA to calculate a deterministic median pseudo-spectral acceleration and standard deviation using the four NGA-West2 GMPEs (shown in Figure 4.5). An example of one ε is depicted between the median and 84th percentile deterministic spectra. The UHS (and scaled UHS) are compared to this deterministic scenario to calculate the number of standard deviations from the median to get the actual ε.

To develop the fragility curves scale factors of 2, 2.5, 3, 3.5, 4, and 4.5 were applied to the UHS, the correlated $D_{5\text{-}75\%}$ and $D_{5\text{-}95\%}$ were calculated, and additional time histories selected. The values of ε used for the correlated duration can be found in Table 3 and the correlated duration values are in Table 4. The time series for each of the scale factors and sites are outlined in Table 5 through

Table 10. The main focus of this selection process was the duration values, so the magnitudes and other parameters of the suites are not as close to the deaggregation results. The difference between the mean duration used for the uncorrelated suite and the mean durations used for the correlated suite increases as scale factor increases.

Table 3. ε values (number of standard deviations from deterministic median ground motion) for the Toll Bridge (1.6 sec)

Scale Factor	ε
1	0.68
2	1.67
2.5	1.99
3	2.25
3.5	2.47
4	2.67
4.5	2.83

Table 4 Correlated Duration values for the Toll Bridge site

Toll Bridge		
Scale Factor	**$D_{5\text{-}75\%}$ (sec)**	**$D_{5\text{-}95\%}$ (sec)**
1	5.79	12.78
2	5.49	12.46
2.5	5.39	12.36
3	5.32	12.28
3.5	5.25	12.21
4	5.20	12.16
4.5	5.15	12.12

Table 5 Suite of time histories for the UHS scale factor of 2, Toll Bridge

RSN	Earthquake Name	Station Name	Mw	$D_{5\text{-}75\%}$ (sec)	$D_{5\text{-}95\%}$ (sec)
173	Imperial Valley-06	El Centro Array #10	6.5	5.3	12.8
1116	Kobe, Japan	Shin-Osaka	6.9	4.5	11.6
1120	Kobe, Japan	Takatori	6.9	6.0	11.3
1158	Kocaeli, Turkey	Duzce	7.5	6.1	11.8
1492	Chi-Chi, Taiwan	TCU052	7.6	5.7	16.7
3748	Cape Mendocino	Ferndale Fire Station	7.0	6.2	13.6
4874	Chuetsu-oki, Japan	Oguni Nagaoka	6.8	5.6	12.2
4894	Chuetsu-oki, Japan	Kashiwazaki NPP Unit 1: ground surface	6.8	6.0	10.4
6962	Darfield, New Zealand	ROLC	7.0	7.1	11.4
8063	Christchurch, New Zealand	Christchurch Botanical Gardens	6.2	4.8	11.4

8118	Christchurch_ New Zealand	Papanui High School	6.2	5.9	13.9

Table 6 Suite of time histories for the UHS scale factor of 2.5, Toll Bridge

RSN	Earthquake Name	Station Name	Mw	$D_{5-75\%}$ (sec)	$D_{5-95\%}$ (sec)		
173	Imperial Valley-06	El Centro Array #10	6.5	5.3	12.8		
1116	Kobe_ Japan	Shin-Osaka	6.9	4.5	11.6		
1120	Kobe_ Japan	Takatori	6.9	6.0	11.3		
1158	Kocaeli_ Turkey	Duzce	7.5	6.1	11.8		
1492	Chi-Chi_ Taiwan	TCU052	7.6	5.7	16.7		
3748	Cape Mendocino	Ferndale Fire Station	7.0	6.2	13.6		
4229	Niigata_ Japan	NIGH12	6.6	5.4	10.1		
4874	Chuetsu-oki_ Japan	Oguni Nagaoka	6.8	5.6	12.2		
4894	Chuetsu-oki_ Japan	Kashiwazaki NPP_ Unit 1: ground surface	6.8	6.0	10.4		
8063	Christchurch_ New Zealand	Christchurch Botanical Gardens	6.2	4.8	11.4		
8118	Christchurch_ New Zealand	Papanui High School	6.2	5.9	13.9		

Table 7 Suite of time histories for the UHS scale factor of 3, Toll Bridge

RSN	Earthquake Name	Station Name	Mw	$D_{5-75\%}$ (sec)	$D_{5-95\%}$ (sec)
173	Imperial Valley-06	El Centro Array #10	6.5	5.3	12.8
1116	Kobe_ Japan	Shin-Osaka	6.9	4.5	11.6
1120	Kobe_ Japan	Takatori	6.9	6.0	11.3
1158	Kocaeli_ Turkey	Duzce	7.5	6.1	11.8
1492	Chi-Chi_ Taiwan	TCU052	7.6	5.7	16.7
3964	Tottori_ Japan	TTR007	6.6	4.9	12.7
4229	Niigata_ Japan	NIGH12	6.6	5.4	10.1
4874	Chuetsu-oki_ Japan	Oguni Nagaoka	6.8	5.6	12.2
4894	Chuetsu-oki_ Japan	Kashiwazaki NPP_ Unit 1: ground surface	6.8	6.0	10.4
8063	Christchurch_ New Zealand	Christchurch Botanical Gardens	6.2	4.8	11.4
8118	Christchurch_ New Zealand	Papanui High School	6.2	5.9	13.9

Table 8 Suite of time histories for the UHS scale factor of 3.5, Toll Bridge

Record Number	Earthquake Name	Station Name	Mw	$D_{5\text{-}75\%}$ (sec)	$D_{5\text{-}95\%}$ (sec)
173	Imperial Valley-06	El Centro Array #10	6.5	5.3	12.8
1116	Kobe, Japan	Shin-Osaka	6.9	4.5	11.6
1120	Kobe, Japan	Takatori	6.9	6.0	11.3
1158	Kocaeli, Turkey	Duzce	7.5	6.1	11.8
1492	Chi-Chi, Taiwan	TCU052	7.6	5.7	16.7
3964	Tottori, Japan	TTR007	6.6	4.9	12.7
4117	Parkfield-02, CA	Parkfield - Fault Zone 15	6.0	5.3	11.7
4228	Niigata, Japan	NIGH11	6.6	3.9	12.2
4874	Chuetsu-oki, Japan	Oguni Nagaoka	6.8	5.6	12.2
4894	Chuetsu-oki, Japan	Kashiwazaki NPP_ Unit 1: ground surface	6.8	6.0	10.4
8063	Christchurch, New Zealand	Christchurch Botanical Gardens	6.2	4.8	11.4

Table 9 Suite of time histories for the UHS scale factor of 4, Toll Bridge

Record Number	Earthquake Name	Station Name	Mw	$D_{5\text{-}75\%}$ (sec)	$D_{5\text{-}95\%}$ (sec)
173	Imperial Valley-06	El Centro Array #10	6.5	5.3	12.8
1111	Kobe, Japan	Nishi-Akashi	6.9	4.5	11.2
1116	Kobe, Japan	Shin-Osaka	6.9	4.5	11.6
1158	Kocaeli, Turkey	Duzce	7.5	6.1	11.8
1492	Chi-Chi, Taiwan	TCU052	7.6	5.7	16.7
3964	Tottori, Japan	TTR007	6.6	4.9	12.7
4117	Parkfield-02, CA	Parkfield - Fault Zone 15	6.0	5.3	11.7
4228	Niigata, Japan	NIGH11	6.6	3.9	12.2
4874	Chuetsu-oki, Japan	Oguni Nagaoka	6.8	5.6	12.2
4894	Chuetsu-oki, Japan	Kashiwazaki NPP_ Unit 1: ground surface	6.8	6.0	10.4
8063	Christchurch, New Zealand	Christchurch Botanical Gardens	6.2	4.8	11.4

Table 10 Suite of time histories for the UHS scale factor of 4.5, Toll Bridge

Record Number	Earthquake Name	Station Name	Mw	$D_{5\text{-}75\%}$ (sec)	$D_{5\text{-}95\%}$ (sec)
173	Imperial Valley-06	El Centro Array #10	6.5	5.3	12.8
768	Loma Prieta	Gilroy Array #4	6.9	5.4	14.8
1111	Kobe, Japan	Nishi-Akashi	6.9	4.5	11.2
1116	Kobe, Japan	Shin-Osaka	6.9	4.5	11.6
1158	Kocaeli, Turkey	Duzce	7.5	6.1	11.8
3964	Tottori, Japan	TTR007	6.6	4.9	12.7
4117	Parkfield-02, CA	Parkfield - Fault Zone 15	6.0	5.3	11.7
4228	Niigata, Japan	NIGH11	6.6	3.9	12.2
4874	Chuetsu-oki, Japan	Oguni Nagaoka	6.8	5.6	12.2
4894	Chuetsu-oki, Japan	Kashiwazaki NPP_ Unit 1: ground surface	6.8	6.0	10.4
8063	Christchurch, New Zealand	Christchurch Botanical Gardens	6.2	4.8	11.4

4.2 STRUCTURAL ANALYSIS

A 2D schematic of the bridge profile is shown in Figure 4.6 including modeling details. However, it is important to note that a full 3D model was developed using OpenSees (McKenna et al., 2010) to capture the behavior due to the 90-degree bend on the span and considering bidirectional ground motion loading. Each pier consists of two reinforced concrete columns. The first 14 piers (see Figure 4.6 for numbering) are isolated using four LRBs located on top of each capping beam. The pier height and span length along the centerline are listed in Table 11.

The pier dimensions increase with increasing height but maintain an assumed reinforcement ratio of 1%. To simplify the model, piers with similar geometric characteristics are grouped together. The piers were divided into 7 sets with geometric characteristics summarized in Table 12 including Column Width, B; Column Depth, D; number of longitudinal bars at top and bottom (#14), number longitudinal bars at the sides (#14), and plastic hinge length, L_p. The sets are Pier 2 through Pier 6, Pier 7 – Pier 11, Pier 12 and 13, and Pier 14 – 17, Pier 18 and 21, Pier 19 and 20, and Pier 22 – 26. A schematic of column section is provided in Figure 4.7. The piers are modeled using beam-with-hinges elements with Concrete02 and Steel02 materials to capture the nonlinear behavior of piers and the concrete degradation of the pier with cyclic loading. A confined core and unconfined concrete fiber section was defined. The compressive strength of concrete is assumed to be 5 ksi and the expected yield strength of the steel rebar is defined as 69 ksi., The plastic hinge length was calculated using Priestley and Park (1987) equation based on pier length (L) and reinforcement diameter ($\boldsymbol{D_{bl}}$) and adapted by Caltrans (2019): P-Delta effects are considered for all piers to account for geometric nonlinearity.

$$L_p = 0.08L + 0.15 f_y D_{bl} \geq 0.3 f_y D_{bl} \quad (4.2)$$

Contrary to buildings, bridges are designed with a "strong beam – weak column" philosophy. As such, damage to bridges is often concentrated on the formation of plastic hinges in the pier while the deck remains elastic. Given the knowledge of this design practice, the pier caps and deck are modeled using elastic beam elements. The deck masses are lumped at the top of each bearing node, and the pier beam cap masses are lumped at the top of each pier. A consistent mass matrix is formulated for the distributed mass of the piers along their height. The structural damping is estimated using Rayleigh damping proportional to mass and the tangent stiffness with coefficients based on the first two modes and a damping ratio of 3% per Caltrans (2019) Section 4. The boundary conditions are simplified by assuming fixed pier bases and a pinned abutment connection. The model ends at pier 26 where the approach ramps begin.

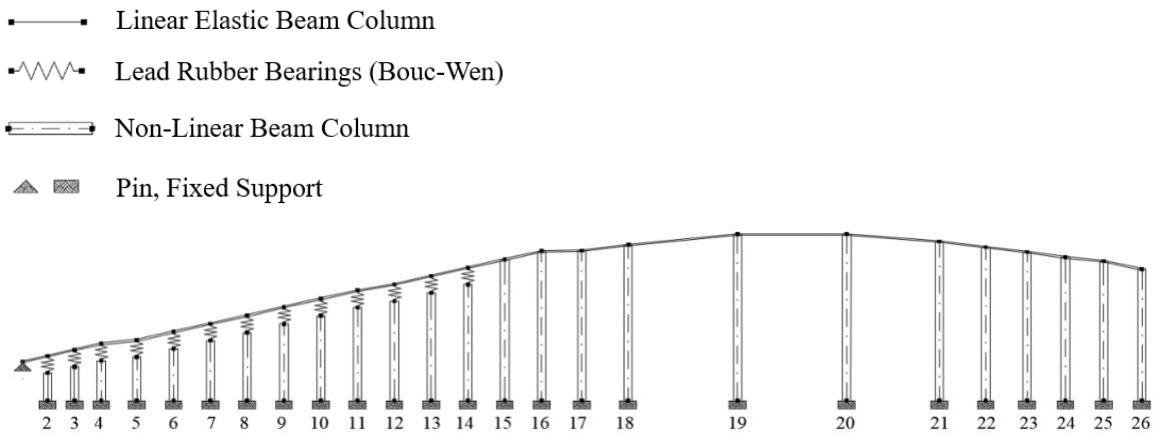

Figure 4.6 Major toll bridge model in profile view.

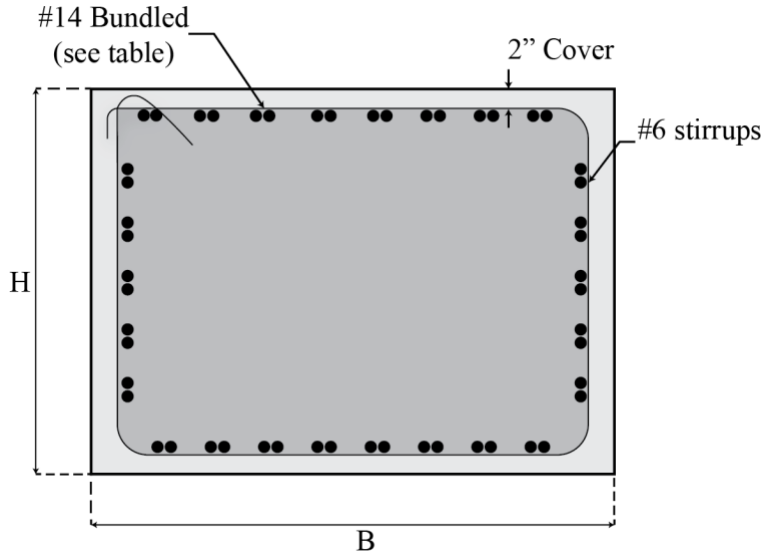

Figure 4.7 Major toll bridge pier cross-section.

The design of the lead rubber bearings is the same across all piers. The geometric and mechanical properties are summarized in Table 13. The LRB is modeled using a two node link element with a hysteretic model including energy degradation in the shear and linear behavior in axial and rotational degrees-of-freedom. Using the geometric properties the mechanical properties of the isolator are calculated following Kelly and Konstantinidis (2011). The vertical and rotational stiffness, K_V and K_θ, are calculated using Equation 4.3 and 4.4 respectively, where E_c is the instantaneous compression modulus of rubber, A is the loaded rubber area, t_r is the total thickness of rubber, and EI_{eff} is the bending stiffness of the annular bearing. The hysteretic behavior of the bearing including degradation is shown in Figure 4.8. The Opensees hysteretic material parameters that control hysteretic degradation is $damage_2$, δ_A, and has a value of 0.005.

$$K_v = \frac{E_c A}{t_r} \tag{4.3}$$

$$K_\theta = \frac{EI_{eff}}{t_r} \tag{4.4}$$

Table 11 Pier properties.

Pier	Height (ft)	Span Length (ft)
1	-	150
2	28.0	162
3	35.0	162
4	42.6	215’-3”
5	50.4	222’-4”
6	65.3	222’-4”
7	75.7	222’-4”
8	85.7	222’-4”
9	96.4	222’-4”
10	106.8	222’-4”
11	117.2	222’-4”
12	125.1	222’-4”
13	135.5	222’-4”
14	145.9	222’-4”
15	156.2	222
16	166.7	242
17	167.5	280
18	174.6	660
19	187.9	660
20	187.9	560
21	178.8	280
22	171.9	250
23	165.7	231
24	159.0	231
25	154.0	231
26	144.0	-

Table 12 Column properties.

Pier Set	B (ft)	D (ft)	N_{l_topbot}	N_{l_side}	L_p (in)
Piers 2 – 6	8.5	8.0	16	8	80
Piers 7 – 11	9.0	9.0	20	8	130
Piers 12 – 13	10.5	11.0	28	10	150
Pier 14 – 17	11.0	12.0	30	14	160
Pier 18 & Pier 21	11.5	13.5	34	16	160
Pier 19 – 20	14.5	14.5	36	32	160
Pier 22 – 26	11.0	12.5	30	14	160

Table 13 Lead Rubber Bearing Properties.

Bearing Property	
Bearing Diameter, $D_{bearing}$ (in)	45.0
Lead core diameter, D_{lead} (in)	9.0
Number of layers, n	20
Total rubber thickness, t_r (in)	15.0
Yield stiffness, K_1 (kip/in)	51.25
Post-yield stiffness ratio, α (kip/in)	0.119
Characteristic strength, Q_d (kip)	87.75
Vertical Stiffness, K_V (kip/in)	3,664
Rotational Stiffness, K_θ (kip-in)	321,200

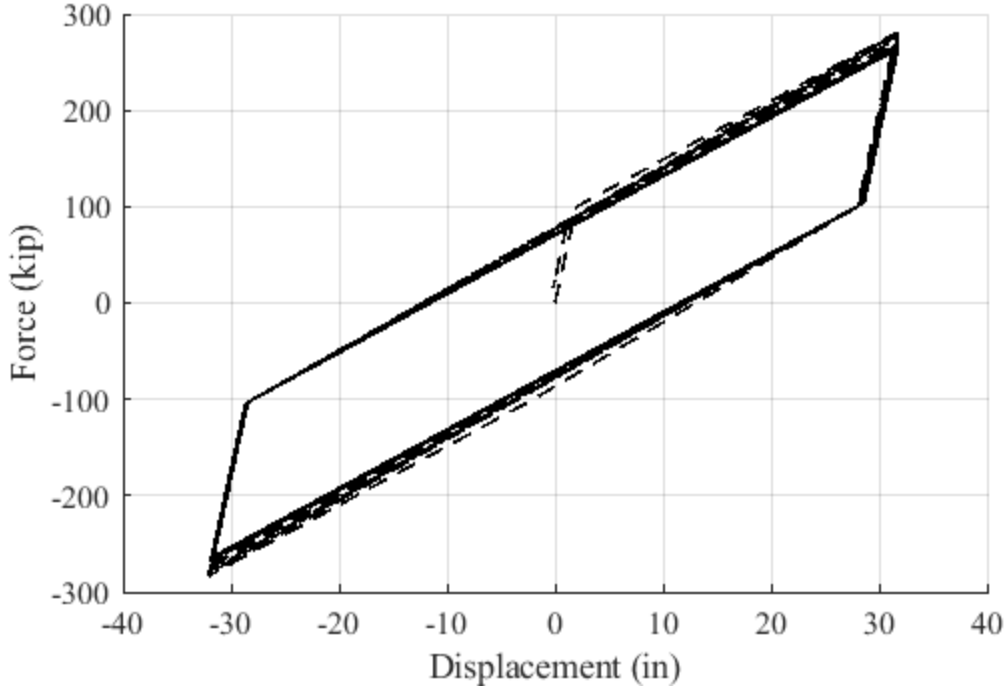

Figure 4.8 Lead rubber bearing model hysteresis.

4.3 DAMAGE ANALYSIS

The purpose of the damage state fragility curves developed in this report is to evaluate the effect of incorporating ground motion duration in the selection of ground motions in IDA. Thus, the fragility curves are not presented as a prediction of the exact bridge performance expected. To determine the damage state of the bridge, the damage states of the components, specifically the piers and isolation bearings, were assessed. Caltrans (2019) Section 1.3 suggests dividing performance into five damage states. This report presents results for two damage states of interest: DS-3 and DS-5, Moderate Damage and Major Damage, respectively. Caltrans defines expected performance; at DS-3 bridge repair is likely, but bridge replacement is unlikely, while at DS-5 bridge replacement is likely. For concrete piers, at DS-3 extensive cracks and spalling of the concrete is expected, while at DS-5 the onset of compressive failure of the core concrete is expected.

Currently there is no formal definition for bearing damage states; for the purpose of this report two bearing damage states are defined. The moderate damage state (DS-3) is defined as the bearing shear strain that leads to reaching the buckling limit under the isolator axial load using the overlapping are method (Buckle and Liu, 1994), which for this design is 235% shear strain. Calculating the stability limit using this method has been shown to lead to a conservative estimate of the stability limit (Weisman & Warn, 2012). As such, the major damage state (DS-5) is defined as the bearing shear strain under which there is no remaining overlap between the top and bottom of the bearing, which occurs at the displacement equal to the bearing diameter, which for this design is 300% shear strain. Table 15 shows the bearing damage states considered for analysis.

Previous studies on bridge column damage correlate engineering demand parameters with observed damage states. Vosooghi and Saiidi (2010) tested 30 reinforced concrete bridge columns and proposed five damage states. They reported statistics for each damage state for six response parameters: maximum drift ratio, residual drift ratio, frequency ratio, inelasticity index, maximum longitudinal steel strain, and maximum transverse steel strain. They found that piers tested under near-field conditions were able to sustain larger drifts before reaching each damage state than the rest of the columns. Vosooghi and Saiidi (2012) tested two more specimens and averaged the results for all 32 columns in the database to develop fragility curves for the six response parameters. A more recent study (Saini and Saiidi, 2014) expanded the existing database to a total of 38 columns and reported updated mean and logarithmic standard deviation for all six response parameters proposed by Vosooghi and Saiidi (2010) as well as updated damage fragility curves.

This study focuses on generating damage fragility curves using the maximum drift ratio of each column, which is easily obtained from OpenSees analysis, to classify the damage state of the individual piers. Since bidirectional ground motions were considered, the maximum displacement was calculated as the peak resultant displacement of each element. While updated parameters from the Vosooghi and Saiidi 2012 and 2014 studies expand the bridge column database, the lumped statistics do not include the difference in damage under near-field motions. As the major toll bridge is predominantly affected by near-field ground motions, the fragility curves developed using the

data reported for columns tested under near-field motions by Vosooghi and Saiidi (2010) are used. Table 14 shows the pier damage states considered for analysis.

The damage fragility curves are found by counting the percent of the ground motions at each spectral acceleration scale under which the damage state occurs across any of the components. This is a conservative approach since it equates overall bridge performance to individual component performance. The fragility curves are obtained using the maximum likelihood fit per Baker (2015). The reason for using the maximum likelihood method instead of the typical method of moments estimator used to fit a lognormal distribution to IDA analysis is that like the case of the multiple stripes analysis (MSA), the suite of the ground motions selected using the correlated duration may not always present the IM values associated with 100% probability of a given damage state. As described by Baker (2015), the function fits a lognormal cumulative distribution function (CDF) to the observed probability of collapse data using optimization on the likelihood function for the data.

Table 14 Pier Damage Limits.

Damage State	Description	Drift Ratio Threshold
DS-1	Minimal Damage: Flexural Cracks	0.029
DS-2	Minor Damage: minor spalling and possible shear cracks	0.041
DS-3	Moderate damage: extensive cracks and spalling	0.059
DS-4	Moderate damage: visible lateral and/or longitudinal reinforcing bars	0.109
DS-5	Major Damage: imminent failure, onset of compressive failure of core concrete	0.131
DS-6	Failure/Collapse	-

Table 15 Bearing Damage Limits.

Damage State	Description	Shear Strain Threshold
DS-3	Moderate Damage: bearing bucking limit at isolator axial load based on overlapping area.	235%
DS-5	Major Damage: imminent failure	300%

4.4 BRIDGE PERFORMANCE

4.4.1 Non-Correlated Suite of Ground Motions – Fragility curves

The observed fractions of reaching damage state DS-3 are plotted against the scale factor of each suite of ground motions, along with the curve fitted to the data for each element in Figure 4.9, Figure **4.10** and Figure 4.11 for the isolation bearings, the isolated piers, and the non-isolated piers, respectively. Figure 4.9 shows that the bearings on mid-height piers are the first to reach DS-3. For instance, the bearing on Pier 6 reaches the median damage probability at a scale factor of 1.09, while the bearing on Pier 2 reaches the same damage probability at a scale factor of 2.37.

The fragility curves of the piers for DS-3, shown in Figure **4.10**, tend to increase with increasing pier height. The increase in damage probability with pier height is seen by the shift of the fitted curves to the left while maintaining a similar dispersion. For the tall piers, DS-3 is reached at smaller scale factors. The isolated piers reach the median damage at scale factors ranging from 3.3 to 5.3. Comparing these values with the ones obtained from the bearing elements on Figure 4.9, shows that the isolation layer is performing as intended by reducing the pier demands and controlling the response. In Figure 4.11 the same plot is repeated for the non-isolated piers. While these have a larger damage probability that the isolated piers, reaching the median damage probability at scale factors ranging form of 3.3 to 3.9, the LRB fragilities continue to control the performance.

The trend in results for the element-level fragility curves are similar for DS-5, and the figures are included in the Appendix. The overall bridge damage is determined based on the maximum damage of any element at each intensity level. Figure 4.12 shows the data points for observed bridge damage with the fitted logarithmic fragility curves. Using the non-correlated motions, the bridge reached the median probability of DS-3 and DS-5 at scale factors of 1.09 and 1.19 respectively.

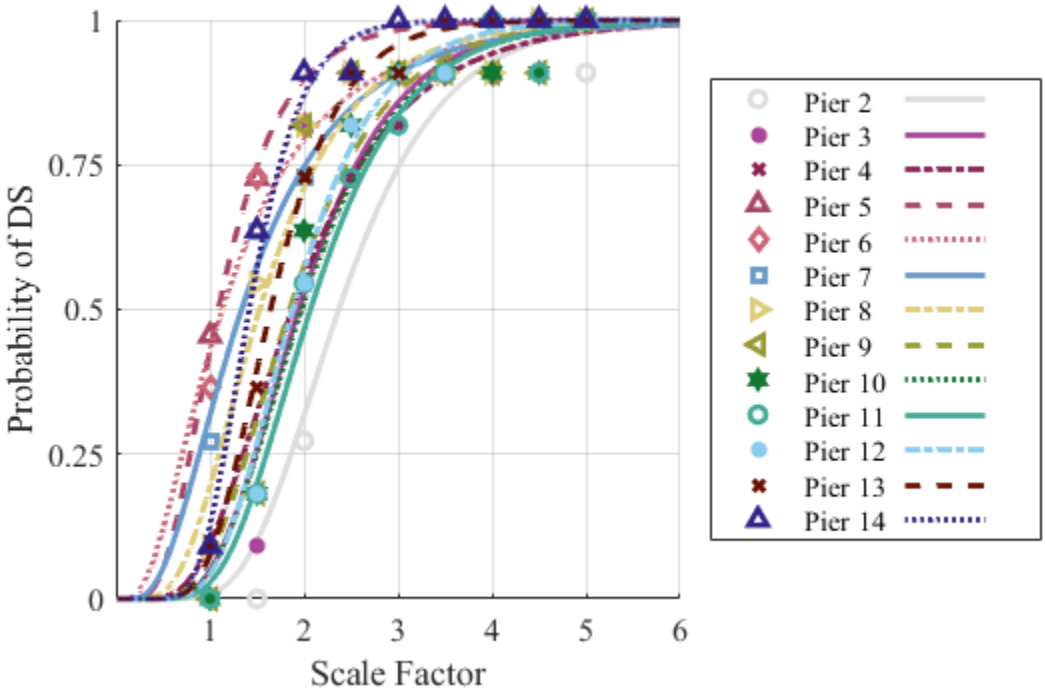

Figure 4.9 DS-3 fitted fragility curves for bearings under non-correlated ground motions.

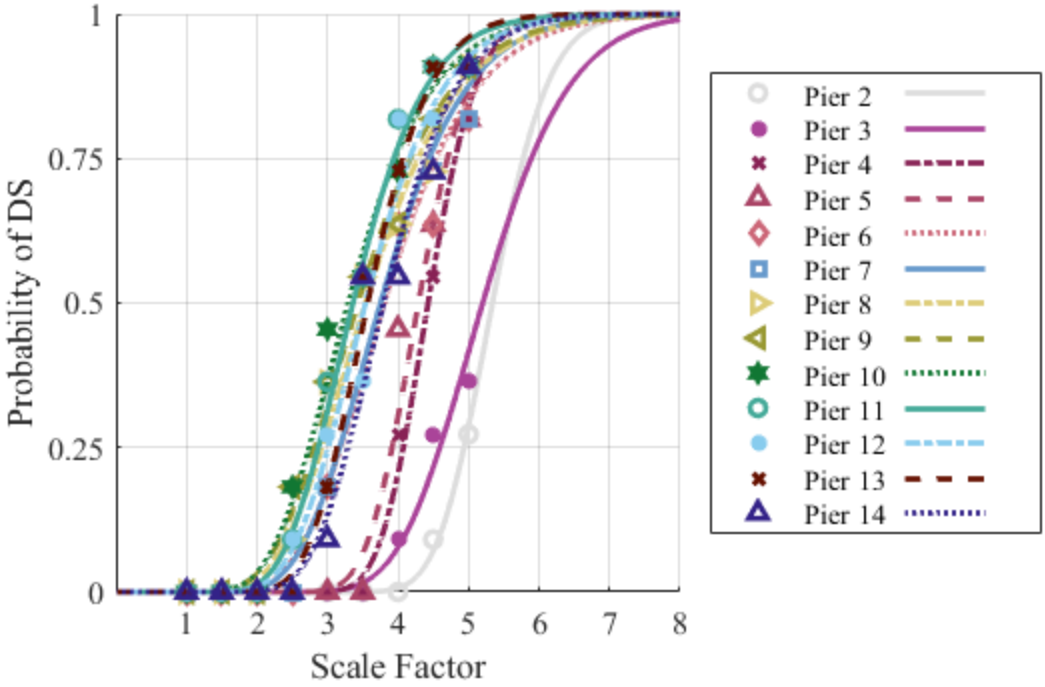

Figure 4.10 DS-3 fitted fragility curves for isolated piers under non-correlated ground motions.

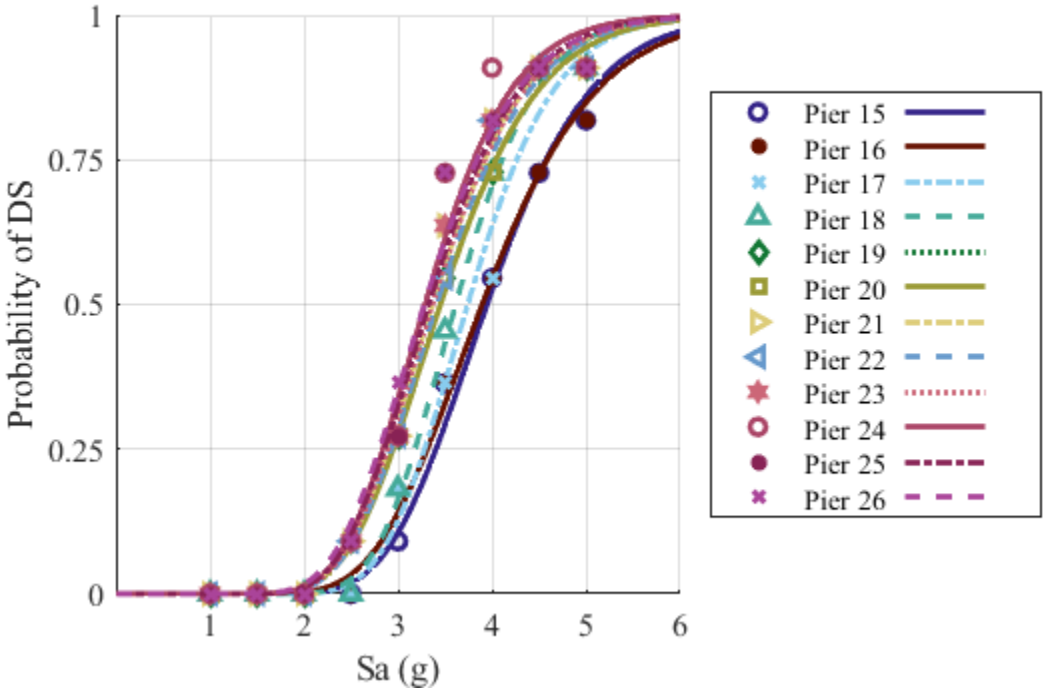

Figure 4.11 DS-3 fitted fragility curves for non-isolated piers under non-correlated ground motions.

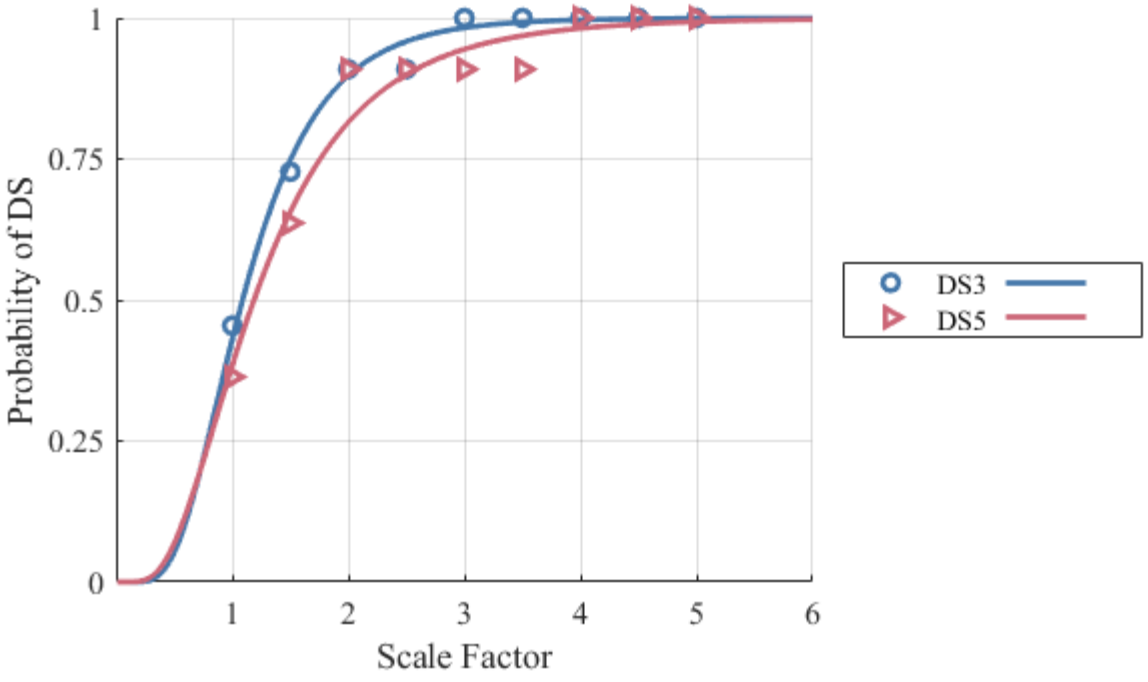

Figure 4.12 Major toll bridge fitted fragility curves for DS-3 and DS-5 under non-correlated ground motions.

4.4.2 Correlated Suite of Ground Motions – Fragilities

For the fragility curves generated using the duration correlated motions, similar trends are observed. There are slight shifts of the fragility curves to the right indicating higher performance is predicted with reduced ground motion duration. In this case the isolation continues to control the response. The bearings observed fractions of reaching DS-3 along with fitted fragility curves are shown in Figure **4.13** reaching the median probability at scale factors of 1.52 and 2.57. Here the bearings mid-height piers 5, and 6 are set apart with a higher damage probability and having a different dispersion from other piers. The fragility curves for the overall bridge are shown in Figure 4.14, the bridge reached the median probability of DS-3 and DS-5 at scale factors of 1.59 and 1.90 respectively. The fragility curves obtained using the duration correlated records presents a slightly larger dispersion than the curves from the non-correlated records. Additional fragility curves are shown in the Appendix.

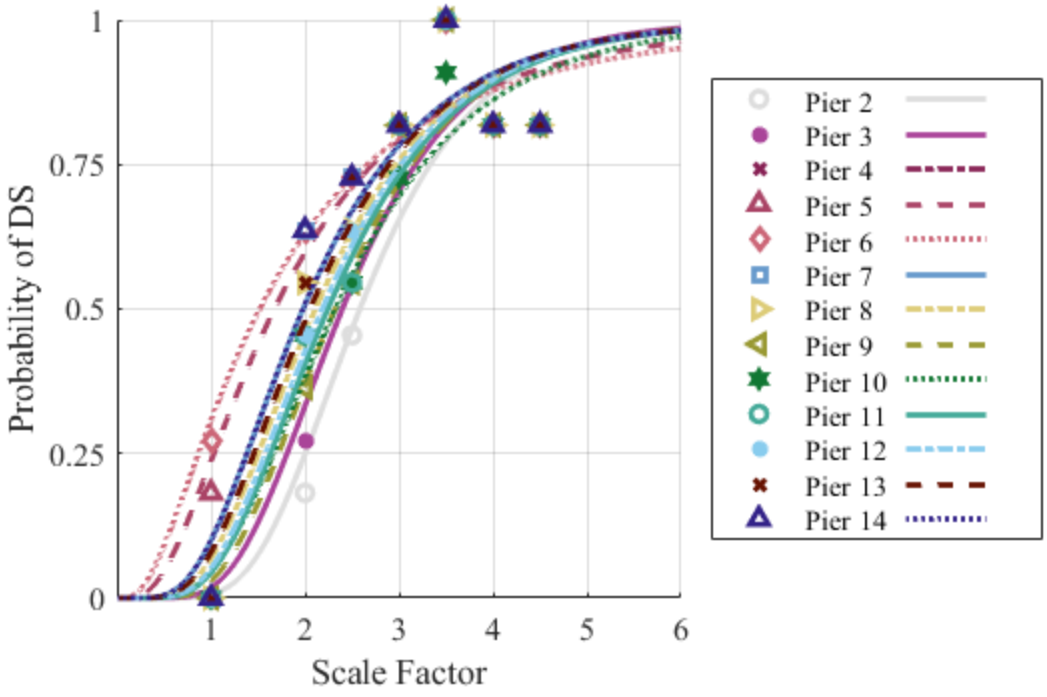

Figure 4.13 DS-3 probability for bearings on each isolated pier with fitted fragility curves under correlated ground motions.

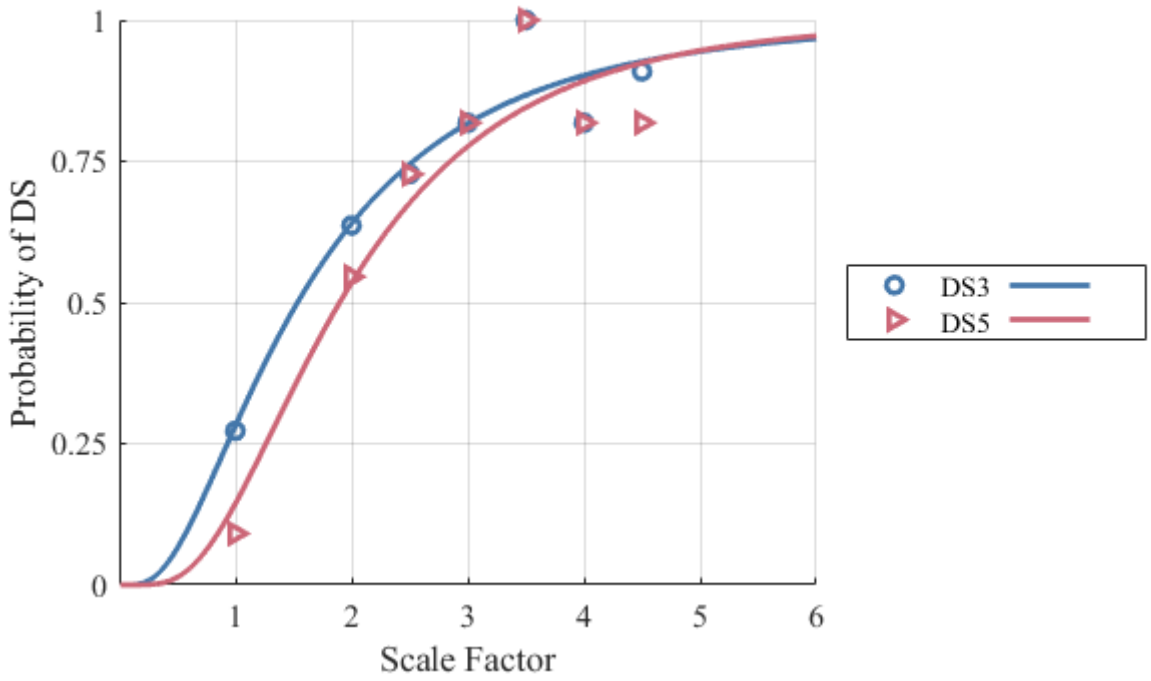

Figure 4.14 Major toll bridge damage probability with fitted fragility curves for DS-3 and DS-5 under correlated ground motions.

4.4.3 Major Toll Bridge Performance Comparison

Comparing the fragility curves developed for both ground motion scaling methodologies, Figure 4.15 shows the fragility curves obtained with the correlated (C) and the non-correlated (NC) data sets for bearings on piers 3, 5 and 14 at DS-3. Here it is seen that the different hazard selection methodologies have different effects on each element. The bearings on Piers 3, 5, and 14, in Figure 4.15, show that under the non-correlated IDA analysis, the median probability of the bearings reaching DS-3 occurs at scale factors of 1.95, 1.09 and 1.42, respectively. However, the fragility curves considering the duration correlated ground motions reach a median DS-3 probability at scale factors of 2.40, 1.68 and 1.98, respectively. These indicate a shift of the median DS-3 fragility curves by 18.8%, 35.1%, and 28.3%. Similarly, Figure 4.16 shows the correlated (C) and the non-correlated (NC) sets for bearings on piers 3, 5 and 14 at DS- 5. The shift in the median DS-5 for bearings on pier 3, 5 and 14 is 9.0%, 38.9% and 20.7%, respectively.

The overall bridge fragility curves obtained from both methodologies are compared in DS-3 and DS-5 and shown in Figure 4.17. The overall performance compared in Figure 4.17 considering all the bridge piers and bearings shows a change in the median probability of 29.2% at DS-3 and 37.4% at DS-5 with changes in dispersion from the non-correlated to the correlated data set. These results show the median probabilities of reaching DS-3 and DS-5 in many cases are lower when the ground motion duration correlation is considered in the analysis.

The average number of cycles at set displacement ranges is calculated and averaged for all 11 ground motions on each suite at scale factors of 1.0, 2.5, and 4.0 to show the effect the duration correlation has on the number of cycles the bearings experienced. The averaged cycle count is presented in Figure 4.18 and Figure 4.19 showing the number of cycles observed in the non-correlated and the correlated cases. The figures show a reduction in the displacement cycles under the duration correlated records as the scale factor increases. This finding supports the original assumption that the number of loading cycles is reduced when ground motion duration correlation is accounted for. This reduction is not the same across elements. For instance, bearing 14 in Figure 4.19 show a larger difference in the number of cycles when compared to bearing 7 in Figure 4.18.

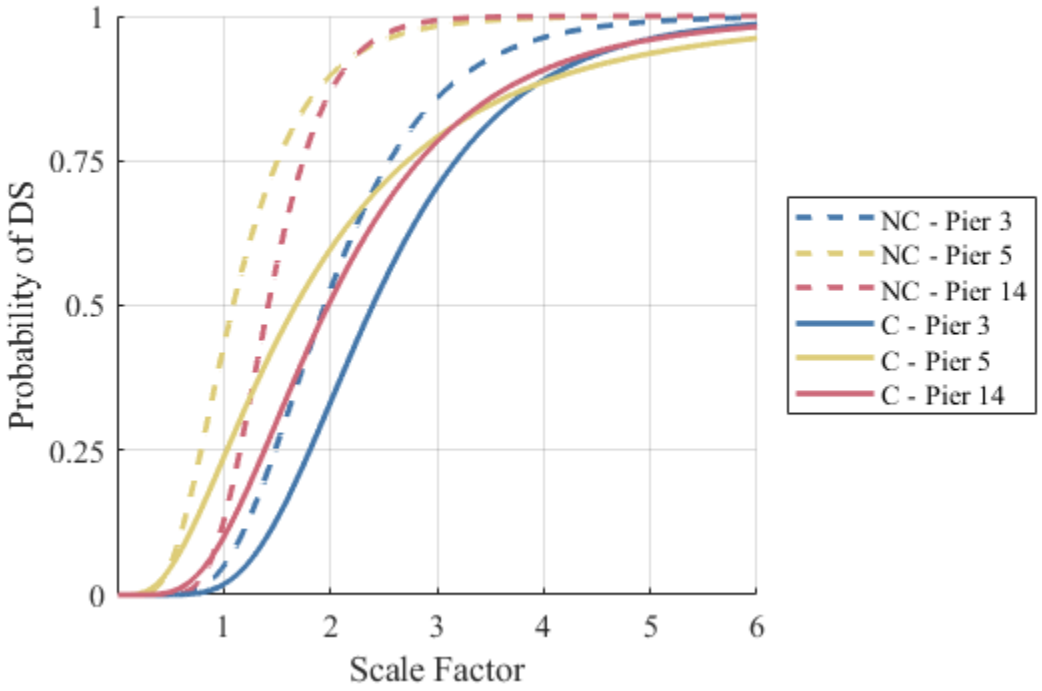

Figure 4.15 Major toll bridge bearings 3, 5, and 14 fragility curves comparison for DS-3.

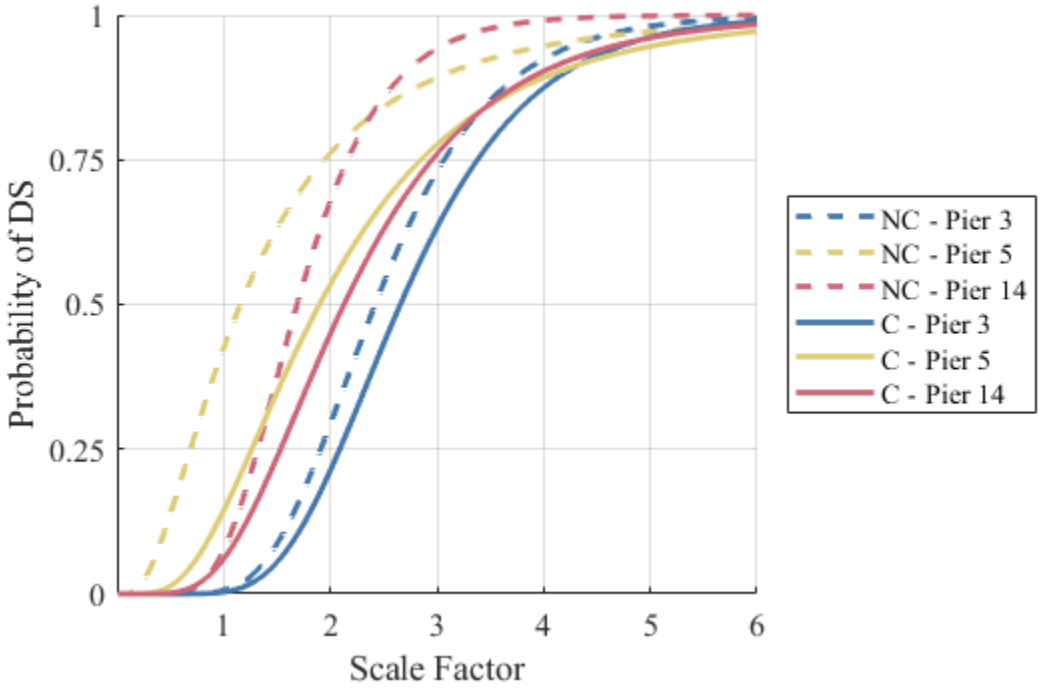

Figure 4.16 Major toll bridge bearings 3, 5, and 14 fragility curves comparison for DS-5.

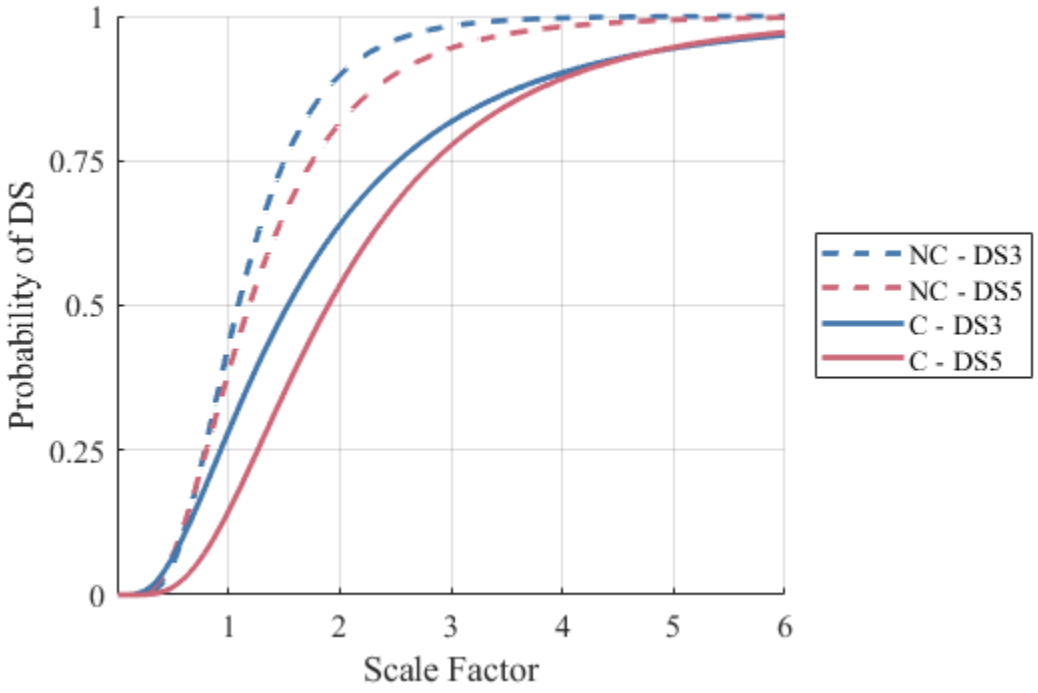

Figure 4.17 Major toll bridge fragility curves comparison.

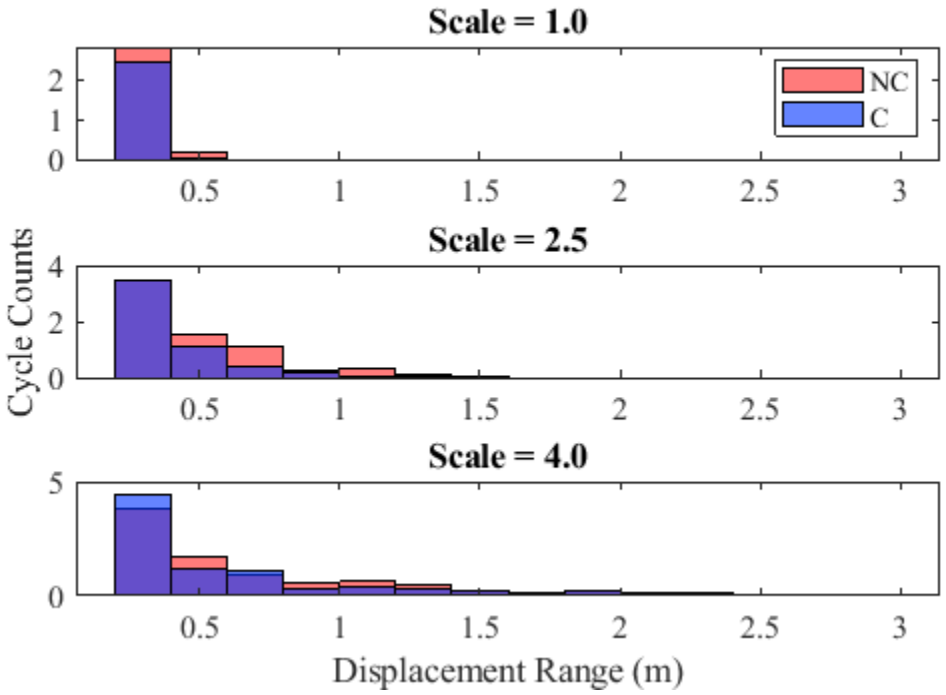

Figure 4.18 Comparison of average number of cycles for bearing 7 over suites of non-correlated (NC) and correlated (C) records at scale factors of 1.0, 2.5, and 4.0.

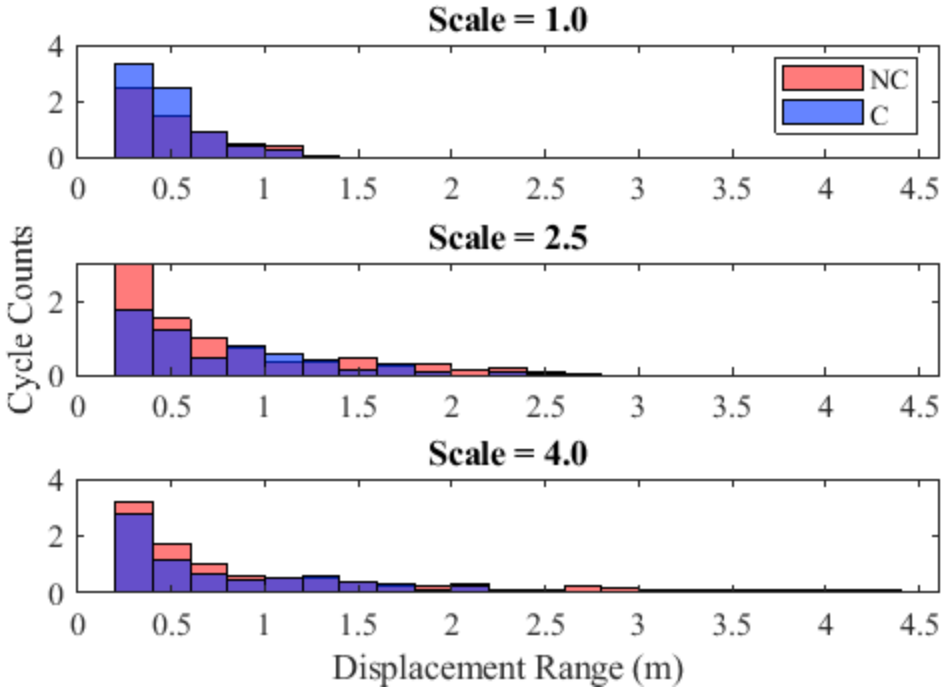

Figure 4.19 Comparison of average number of cycles for bearing 14 over suites of non-correlated (NC) and correlated (C) records at scale factors of 1.0, 2.5, and 4.0.

5 TYPICAL HIGHWAY OVERPASS

For the second case study, a typical highway overpass was selected as these are commonly designed structures and, thus, any changes to understanding of their performance has wide ranging consequences. The overpass has a first period of roughly 0.5 seconds and is located in Northern California, shown in Figure 5.1. This second case study aims to capture different correlation changes due to the change in structural period, particularly for a short period bridge, while the pervious chapter explored a long period bridge. The same methodology as followed in Section 4 is used to examine the effect of including duration correlation in the performance analysis.

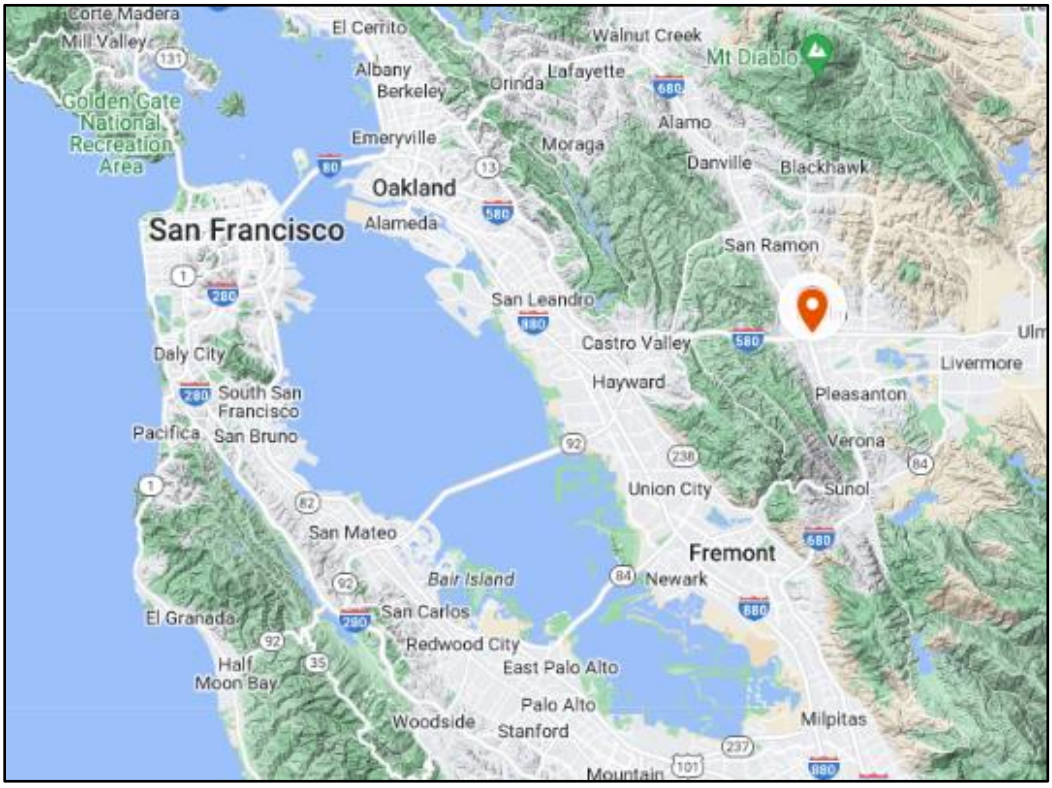

Figure 5.1 Major toll bridge location in Southern California showing curved span on plan view.[10]

[10] Google Maps, 2023

5.1 SELECTION OF GROUND MOTIONS

5.1.1 Hazard Analysis

The UHS for a return period of 2,475 years (corresponding to a 2% probability of exceedance in 50 years) was developed using the method outlined in Section 3.1 and shown in Figure 5.2. Figure 5.3 are the design spectrum and the deaggregation of the PSHA results for a V_{S30} of 250 m/s for the period of the bridge (0.35 seconds). The median magnitude and distance were found to be Mw 7.0 at 10 km. These values were used in the deterministic analysis to calculate the ε for the duration correlation analysis (mentioned later).

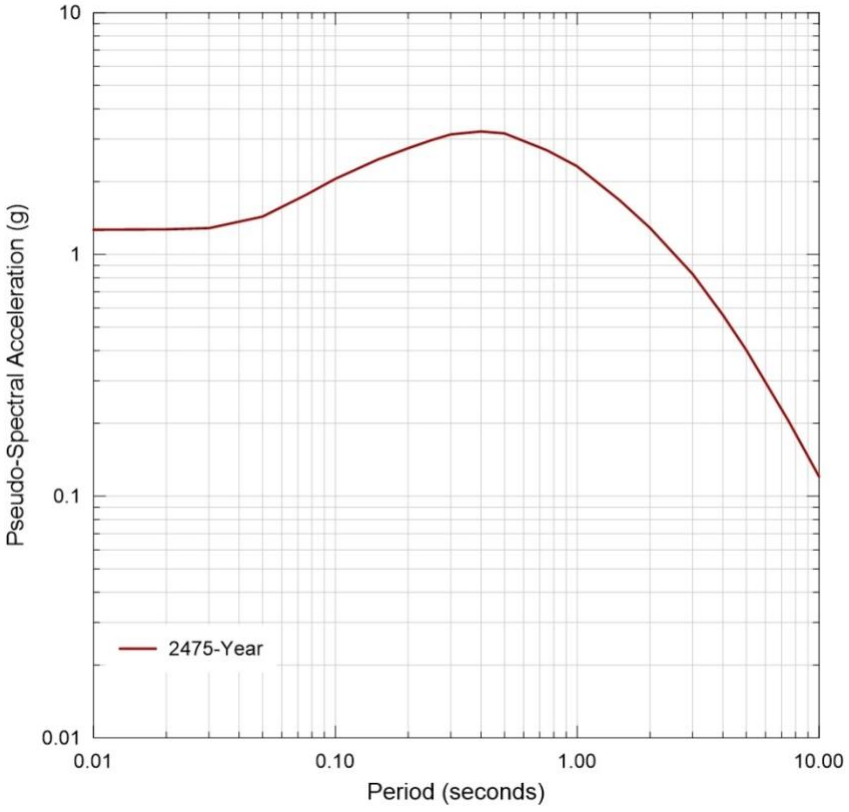

Figure 5.2. Uniform hazard spectra for a return period of 2,475 years (corresponding to a 2% probability of exceedance in 50 years, Maximum Considered Earthquake) for the highway overpass location.

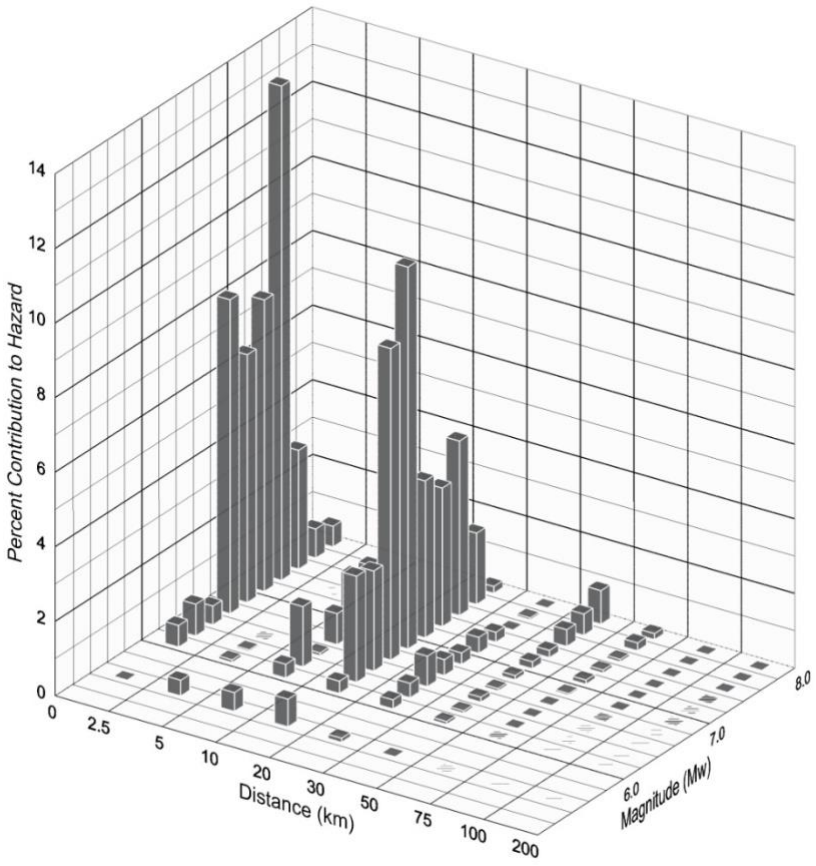

Figure 5.3. 2475-year return period hazard deaggregation at a period of 0.35 second showing near fault contribution.

5.1.2 General Selection of Seed Time Series

The specific earthquake source parameters that represent the dominant earthquake scenario in the seismic hazard were used in the selection of seed time series. Criteria used to sort, prioritize, and select seed time series for the bedrock analysis spectra from the PEER Center NGA-West2 Ground Motion Database included the following for all suites:

- Magnitude (M_w): 7.0 – 8.6;
- Rupture distance: 0 – 50 km;

5.1.3 Selection of Non-correlated Suite

The first suite was selected based on the mean duration values from the DPEs and the other parameters listed above. For the two sites the mean duration values from the DPEs are as follows:

- $D_{5\text{-}75}$: 7.3 seconds
- $D_{5\text{-}95}$: 15.51 seconds

The suite using these duration bounds is shown in Table 16.

Table 16. Non-correlated suite of time histories

RSN	Earthquake Name	Station Name	Mw	$D_{5\text{-}75\%}$ (sec)	$D_{5\text{-}95\%}$ (sec)
728	Superstition Hills-02	Westmorland Fire Sta	6.5	11.9	23.5
806	Loma Prieta	Sunnyvale - Colton Ave.	6.9	9.9	25.3
827	Cape Mendocino	Fortuna - Fortuna Blvd	7.0	11.3	18.7
900	Landers	Yermo Fire Station	7.3	10.9	18.9
1193	Chi-Chi, Taiwan	CHY024	7.6	13.8	27.0
1244	Chi-Chi, Taiwan	CHY101	7.6	13.5	30.4
2114	Denali, Alaska	TAPS Pump Station #10	7.9	9.1	29.5
4859	Chuetsu-oki, Japan	Mitsuke Kazuiti Arita Town	6.8	17.8	29.4
6911	Darfield, New Zealand	HORC	7.0	7.0	9.5
6953	Darfield, New Zealand	Pages Road Pumping Station	7.0	11.2	22.0
8606	El Mayor-Cucapah, Mexico	Westside Elementary School	7.2	10.1	25.3

5.1.4 Selection of Correlated Suites

ε is calculated using the deaggregation results from the PSHA to calculate a deterministic median pseudo-spectral acceleration and standard deviation using the four NGA-West2 GMPEs (shown in Figure 5.4. ε is depicted between the median and 84th percentile deterministic spectra. The UHS (and scaled UHS) are compared to this deterministic scenario to calculate the number of standard deviations from the median, to get the actual ε.

To develop the fragility curves scale factors of 2, 2.5, 3, 3.5, 4, and 4.5 were applied to the UHS, the correlated $D_{5\text{-}75\%}$ and $D_{5\text{-}95\%}$ were calculated, and additional time histories selected. The values of ε used for the correlated duration can be found in Table 17 and the correlated duration values are in Table 18. The time histories for each of the scale factors and sites are outlined in Table 19 through Table 24. The main focus of this selection process was the duration values, so the magnitudes and other parameters of the suites are not as close to the deaggregation results. The difference between the mean duration used for the uncorrelated suite and the mean durations used for the correlated suite increases as scale factor increases.

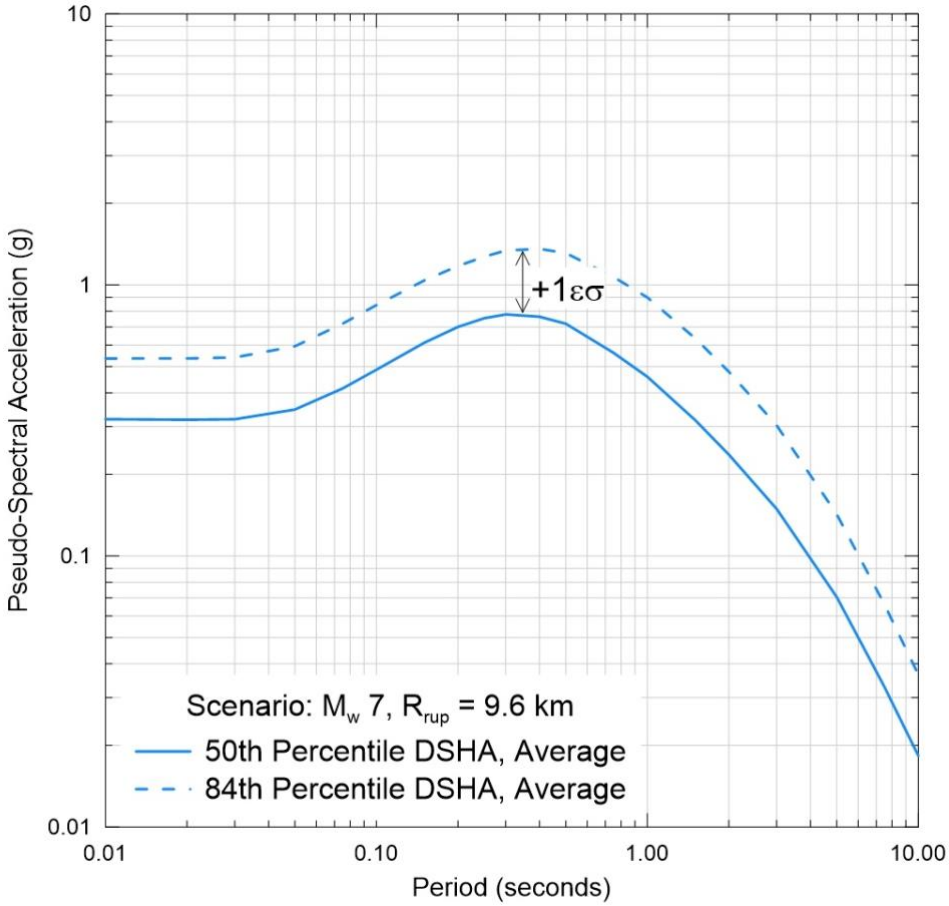

Figure 5.4. Deterministic spectra and depiction of epsilon for the highway overpass

Table 17. ε values (number of standard deviations from deterministic median ground motion) for the Highway Overpass (0.35 sec)

Scale Factor	ε
1	2.53
2	3.77
2.5	4.17
3	4.50
3.5	4.77
4	5.01
4.5	5.22

Table 18 Correlated Duration values for the Highway Overpass Site

Highway Overpass		
Scale Factor	**$D_{5\text{-}75\%}$ (sec)**	**$D_{5\text{-}95\%}$ (sec)**
1	5.02	12.14
2	4.20	10.80
2.5	3.96	10.40
3	3.78	10.09
3.5	3.64	9.83
4	3.52	9.62
4.5	3.41	9.43

Table 19 Suite of time histories for the UHS scale factor of 2, Highway Overpass

RSN	Earthquake Name	Station Name	Mw	$D_{5\text{-}75\%}$ (sec)	$D_{5\text{-}95\%}$ (sec)
173	Imperial Valley-06	El Centro Array #10	6.5	5.3	12.8
181	Imperial Valley-06	El Centro Array #6	6.5	5.3	11.5
778	Loma Prieta	Hollister Differential Array	6.9	4.2	13.3
803	Loma Prieta	Saratoga - W Valley Coll.	6.9	4.1	11.1
1116	Kobe_ Japan	Shin-Osaka	6.9	4.5	11.6
1120	Kobe_ Japan	Takatori	6.9	6.0	11.3
1158	Kocaeli_ Turkey	Duzce	7.5	6.1	11.8
2650	Chi-Chi_ Taiwan-03	TCU116	6.2	4.9	12.3
3748	Cape Mendocino	Ferndale Fire Station	7.0	6.2	13.6
4894	Chuetsu-oki_ Japan	Kashiwazaki NPP_ Unit 1: ground surface	6.8	6.0	10.4
8123	Christchurch_ New Zealand	Christchurch Resthaven	6.2	4.4	11.2

Table 20 Suite of time histories for the UHS scale factor of 2.5, Highway Overpass

RSN	Earthquake Name	Station Name	Mw	$D_{5\text{-}75\%}$ (sec)	$D_{5\text{-}95\%}$ (sec)
173	Imperial Valley-06	El Centro Array #10	6.5	5.3	12.8
181	Imperial Valley-06	El Centro Array #6	6.5	5.3	11.5
803	Loma Prieta	Saratoga - W Valley Coll.	6.9	4.1	11.1
982	Northridge-01	Jensen Filter Plant Administrative Building	6.7	4.0	12.5
1116	Kobe_ Japan	Shin-Osaka	6.9	4.5	11.6
1120	Kobe_ Japan	Takatori	6.9	6.0	11.3
1158	Kocaeli_ Turkey	Duzce	7.5	6.1	11.8
1197	Chi-Chi_ Taiwan	CHY028	7.6	4.8	8.7
2650	Chi-Chi_ Taiwan-03	TCU116	6.2	4.9	12.3
4894	Chuetsu-oki_ Japan	Kashiwazaki NPP_ Unit 1: ground surface	6.8	6.0	10.4
8123	Christchurch_ New Zealand	Christchurch Resthaven	6.2	4.4	11.2

Table 21 Suite of time histories for the UHS scale factor of 3, Highway Overpass

RSN	Earthquake Name	Station Name	Mw	$D_{5\text{-}75\%}$ (sec)	$D_{5\text{-}95\%}$ (sec)
181	Imperial Valley-06	El Centro Array #6	6.5	5.3	11.5
778	Loma Prieta	Hollister Differential Array	6.9	4.2	13.3
803	Loma Prieta	Saratoga - W Valley Coll.	6.9	4.1	11.1
982	Northridge-01	Jensen Filter Plant Administrative Building	6.7	4.0	12.5
1063	Northridge-01	Rinaldi Receiving Sta	6.7	4.3	9.1
1116	Kobe_ Japan	Shin-Osaka	6.9	4.5	11.6
1158	Kocaeli_ Turkey	Duzce	7.5	6.1	11.8
1197	Chi-Chi_ Taiwan	CHY028	7.6	4.8	8.7
2650	Chi-Chi_ Taiwan-03	TCU116	6.2	4.9	12.3
3746	Cape Mendocino	Centerville Beach_ Naval Fac	7.0	4.6	10.6
4115	Parkfield-02_ CA	Parkfield - Fault Zone 12	6.0	4.0	9.7

Table 22 Suite of time histories for the UHS scale factor of 3.5, Highway Overpass

Record Number	Earthquake Name	Station Name	Mw	$D_{5-75\%}$ (sec)	$D_{5-95\%}$ (sec)
181	Imperial Valley-06	El Centro Array #6	6.5	5.3	11.5
803	Loma Prieta	Saratoga - W Valley Coll.	6.9	4.1	11.1
982	Northridge-01	Jensen Filter Plant Administrative Building	6.7	4.0	12.5
1063	Northridge-01	Rinaldi Receiving Sta	6.7	4.3	9.1
1116	Kobe_ Japan	Shin-Osaka	6.9	4.5	11.6
1197	Chi-Chi_ Taiwan	CHY028	7.6	4.8	8.7
2650	Chi-Chi_ Taiwan-03	TCU116	6.2	4.9	12.3
3746	Cape Mendocino	Centerville Beach_ Naval Fac	7.0	4.6	10.6
3943	Tottori_ Japan	SMN015	6.6	3.7	9.9
4115	Parkfield-02_ CA	Parkfield - Fault Zone 12	6.0	4.0	9.7
8123	Christchurch_ New Zealand	Christchurch Resthaven	6.2	4.4	11.2

Table 23 Suite of time histories for the UHS scale factor of 4, Highway Overpass

Record Number	Earthquake Name	Station Name	Mw	$D_{5-75\%}$ (sec)	$D_{5-95\%}$ (sec)
181	Imperial Valley-06	El Centro Array #6	6.5	5.3	11.5
803	Loma Prieta	Saratoga - W Valley Coll.	6.9	4.1	11.1
982	Northridge-01	Jensen Filter Plant Administrative Building	6.7	4.0	12.5
1063	Northridge-01	Rinaldi Receiving Sta	6.7	4.3	9.1
2650	Chi-Chi_ Taiwan-03	TCU116	6.2	4.9	12.3
2655	Chi-Chi_ Taiwan-03	TCU122	6.2	3.3	9.0
3746	Cape Mendocino	Centerville Beach_ Naval Fac	7.0	4.6	10.6
3943	Tottori_ Japan	SMN015	6.6	3.7	9.9
4115	Parkfield-02_ CA	Parkfield - Fault Zone 12	6.0	4.0	9.7
4131	Parkfield-02_ CA	Parkfield - Vineyard Cany 1W	6.0	4.3	8.7
8123	Christchurch_ New Zealand	Christchurch Resthaven	6.2	4.4	11.2

Table 24 Suite of time histories for the UHS scale factor of 4.5, Highway Overpass

Record Number	Earthquake Name	Station Name	Mw	$D_{5\text{-}75\%}$ (sec)	$D_{5\text{-}95\%}$ (sec)
181	Imperial Valley-06	El Centro Array #6	6.5	5.3	11.5
802	Loma Prieta	Saratoga - Aloha Ave	6.9	4.1	9.4
803	Loma Prieta	Saratoga - W Valley Coll.	6.9	4.1	11.1
982	Northridge-01	Jensen Filter Plant Administrative Building	6.7	4.0	12.5
1085	Northridge-01	Sylmar - Converter Sta East	6.7	3.8	7.4
2655	Chi-Chi_ Taiwan-03	TCU122	6.2	3.3	9.0
3744	Cape Mendocino	Bunker Hill FAA	7.0	3.6	13.4
3746	Cape Mendocino	Centerville Beach_ Naval Fac	7.0	4.6	10.6
3943	Tottori_ Japan	SMN015	6.6	3.7	9.9
4115	Parkfield-02_ CA	Parkfield - Fault Zone 12	6.0	4.0	9.7
4131	Parkfield-02_ CA	Parkfield - Vineyard Cany 1W	6.0	4.3	8.7

5.2 OPENSEES MODEL

The typical highway bridge model is based on a typical Caltrans bridge located in Northern California. The bridge has a single concrete pier and a concrete box girder deck of two spans supported by concrete seat abutments. A schematic of the bridge, reflecting the numerical modeling layout in OpenSees, is shown in Figure 5.5. The deck is modeled using an elastic-beam column element and the pier is modeled using a beam with hinges element to capture the nonlinear behavior of the pier. A cross-section of the pier is presented in Figure 5.6. The concrete and steel reinforcement materials are modeled using Concrete02 and Steel02 to capture material degradation. The concrete compressive strength is 4 ksi, while the steel expected yield strength is defined as 69 ksi. A fiber section including core confinement, unconfined cover and longitudinal steel bars is defined for the plastic hinge section of the pier. The length of the plastic hinge, $\boldsymbol{L_p}$, is calculated using Equation (**4.1**) proposed by Priestley and Park (1987).

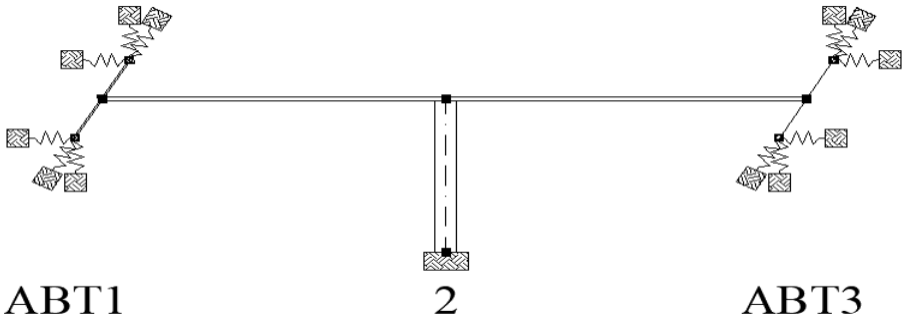

Figure 5.5 Typical highway bridge damage model

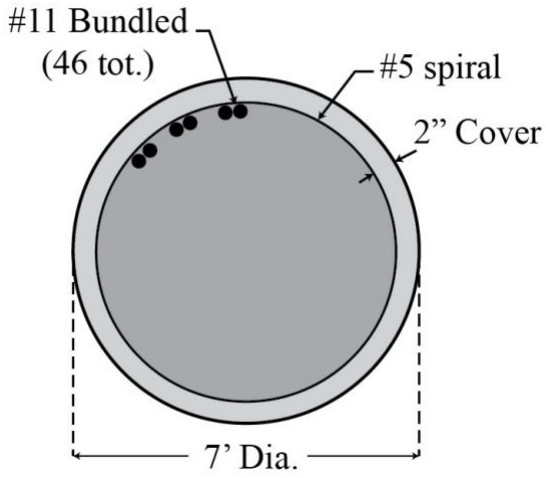

Figure 5.6 Typical highway bridge pier cross-section.

The abutments are modeled using a simplified abutment model as described in Caltrans (2019) Section 6. The abutment backwall is modeled with a rigid beam perpendicular to the span, supported by three springs at each end of the beam. The longitudinal behavior is modeled using two materials, a compression-only springs in parallel with an elastic perfectly-plastic gap spring and an elastic spring based on the bearings, combined in parallel. The transverse behavior of the abutments is modeled using an elastic-perfectly plastic material by modifying the longitudinal stiffness and load capacity using wall effectiveness and participation coefficients, $C_L = 2/3$, and $C_W = 4/3$ (Maroney and Chai, 1994). The vertical behavior is modeled with a compression-only elastic spring and a very large stiffness. The abutment modeling parameters are calculated following Caltrans (2019) Section 6 and equations are replicated here for reference. The stiffness and yielding force of the longitudinal spring, K_{abl} and P_{abl}, is calculated using Equation 5.1 and 4.2, where w_{bw} and h_{bw} are the width and the height of the abutment backwall, and R_{sk} is the skew reduction factor due to the skew angle, θ. The Transverse stiffness and yielding force, K_{abt}

and P_{abt}, are calculated using Equation 5.4 and 5.5. Table 25 shows the summary of model parameters and a schematic of the abutment springs is presented in Figure 5.7 for clarity.

$$K_{abl} = w_{bw}\ (5.5h_{bw} + 20)R_{sk} \tag{5.1}$$

$$P_{abl} = w_{bw}\ \left(\frac{5.5{h_{bw}}^{2.5}}{1+2.37h_{bw}}\right)R_{sk} \tag{5.2}$$

$$R_{sk} = e^{\frac{-\theta}{45}} \tag{5.3}$$

$$K_{abt} = 1\ /\ 3 \times C_L \times C_W \times K_{abl} \tag{5.4}$$

$$P_{abt} = 1\ /\ 3 \times C_L \times C_W \times P_{abl} \tag{5.5}$$

Table 25 Typical Highway Bridge Properties.

Bearing Property	
Backwall width, w_{bw} (ft)	47.3
Backwall Length , h_{bw} (ft)	5.5
skew angle, θ (deg)	25
Skew reduction factor, R_{sk}	0.64
Longitudinal bearing stiffness, K_{ab_brg} (kip/in)	57.6
Longitudinal gap, Δ_{gap} (in)	1.5
Longitudinal stiffness, K_{abl} (kip/in)	131,500
Longitudinal yield force, P_{abl} (kip)	425,200
Transverse stiffness, K_{abt} (kip/in)	39,030
Transverse yield force, P_{abt} (kip)	126,000
Plastic hinge length, L_p (in)	20

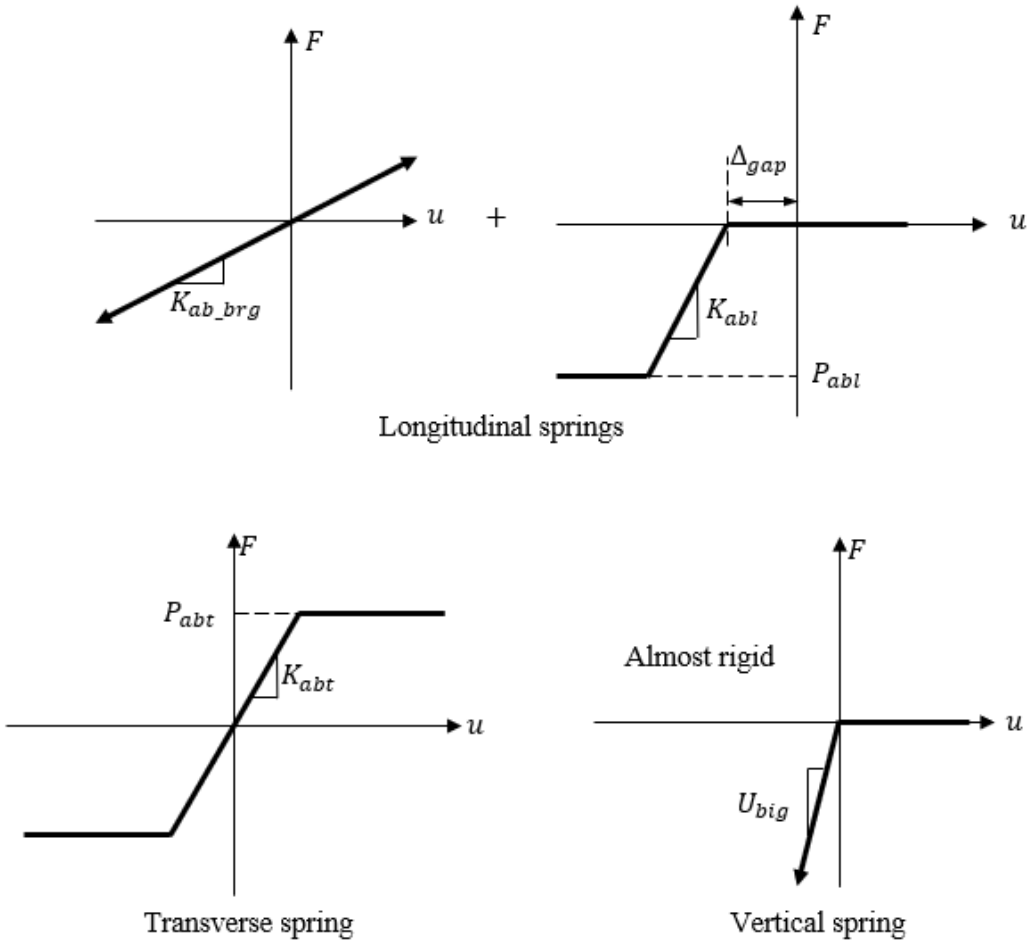

Figure 5.7 Typical highway bridge – Abutment model springs.

5.3 TYPICAL HIGHWAY BRIDGE PERFORMANCE

The performance of the typical highway overpass is evaluated by the same process described in Chapter 4.3 by calculating the damage probability for pier 1. The overall bridge performance for the typical highway bridge focuses solely on the pier drift for the purpose of comparing both ground motion selection methodologies. The typical bridge pushover curve of the overpass bridge, with the occurrence of damage states is shown in Figure 5.8, showing the pier strength degradation with increasing drift. The observed fractions of damage states resulting from the numerical analysis of both ground motion sets are presented along with the fitted fragility curve for the bridge pier. Figure 5.9 shows the fragility curves resulting from the non-correlated data set while Figure 5.10 shows the pier fragility curves resulting from the correlated ground motions. In the case of the correlated ground motions, there is high number of observations of DS-3 even at a scale of 1.0, as such there is not an adequate spread of data to generate a fragility curve, and the curve shown should not be used to derive statistics of performance.

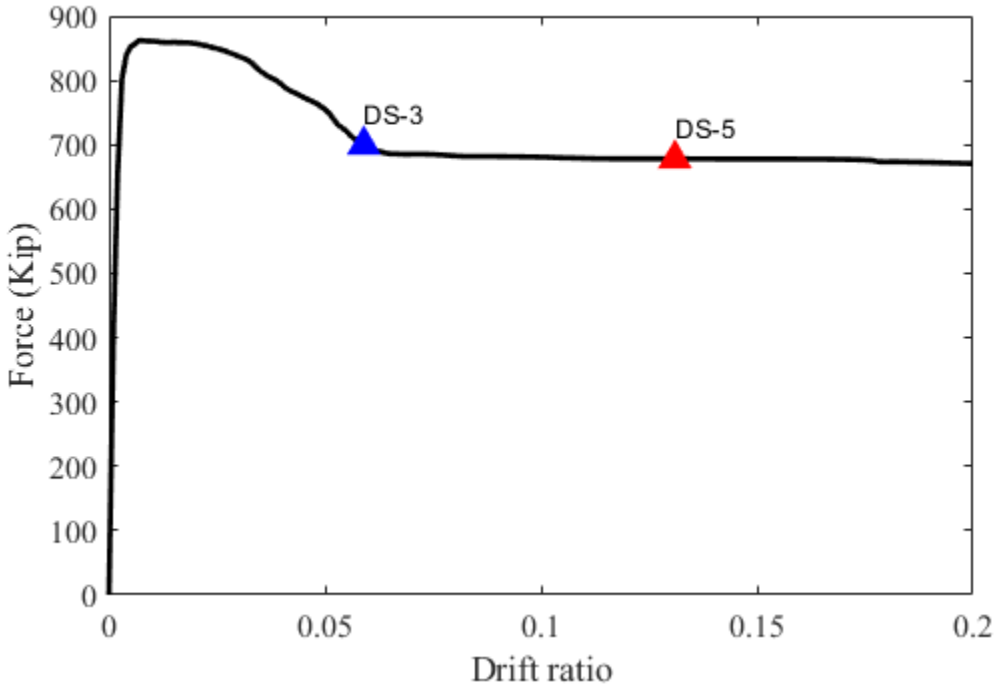

Figure 5.8 Typical highway bridge pushover curve showing DS-3 and DS-5.

A comparison of the fragility curves developed for both ground motion sets is presented in Figure 5.11. For DS-5, the analysis considering the duration correlated ground motions leads to reaching the median damage probability at a scale factor of 1.68 as compared to a scale factor of 1.39 for the non-correlated IDA analysis. This shift is a 17.3% increase in the intensity expected to reach the median DS-5 probability and shows that considering ground motion duration correlation in the scaling reduces the damage expected in the structure for the typical highway overpass. For DS-3, however, due to the lack of data to get an accurate dispersion of the correlated set no significant changes to the median probability of collapse can be observed. The average number of cycles is calculated over the non-correlated and correlated suites at scale factors of 1.0, 2.0, and 3.0 and presented in Figure 5.12. Here there is a clear reduction in the number of cycles the pier experiences with increasing scale factor. As such, the reduction in damage probability from the non-correlated to the correlated data set is attributed to this reduction in the number of cycles the structure experiences.

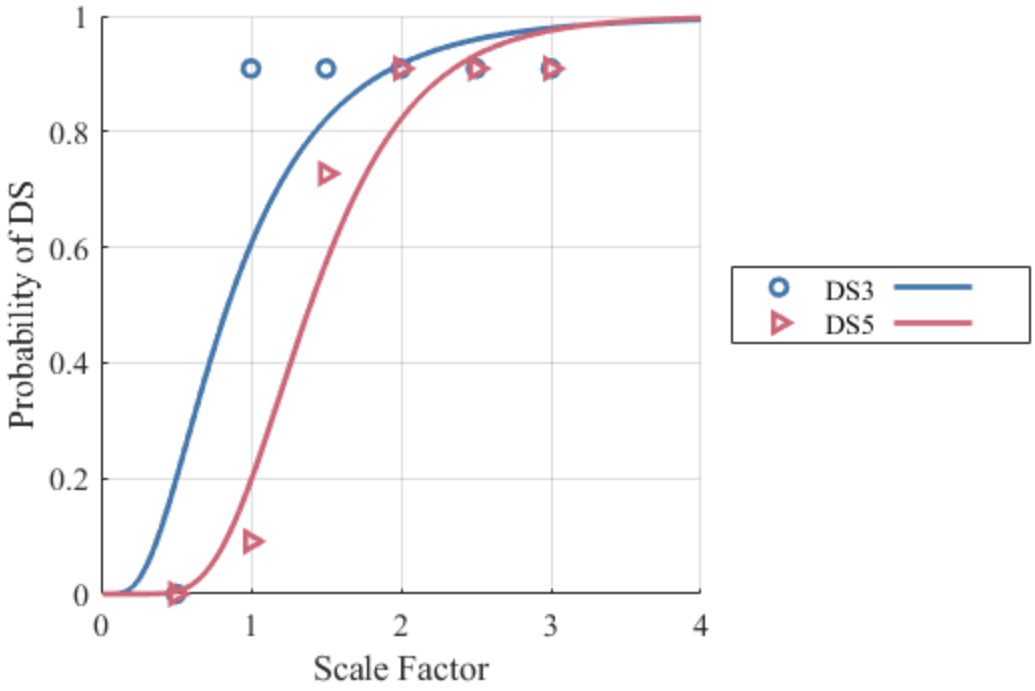

Figure 5.9 Typical bridge, DS-3 and DS-5 probability with fitted fragility curves under non-correlated ground motions.

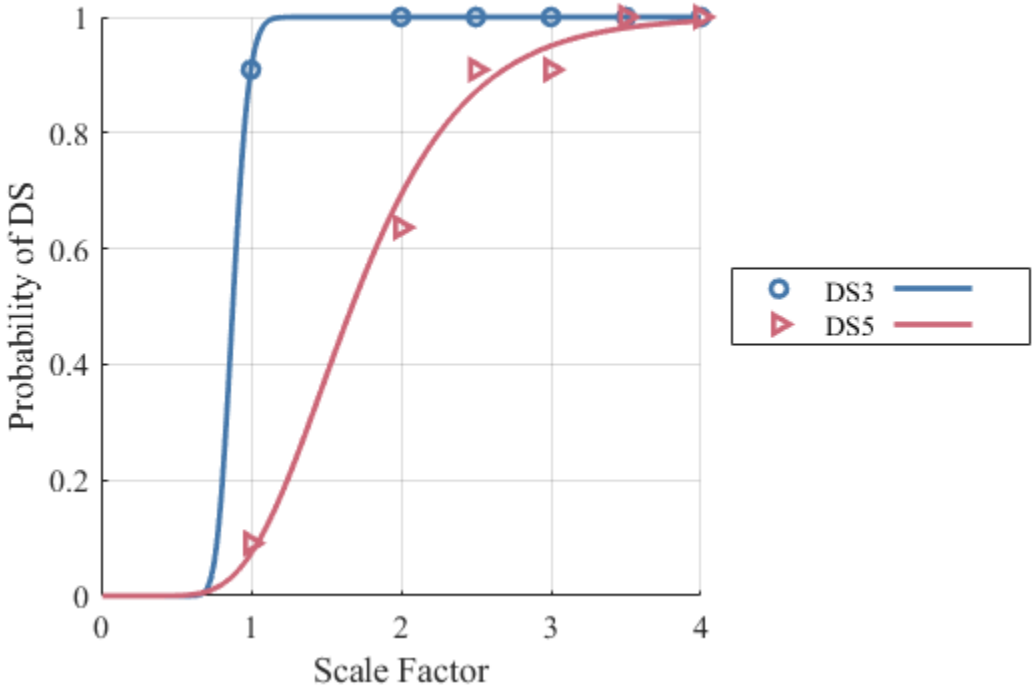

Figure 5.10 Typical bridge, DS-3 and DS-5 probability with fitted fragility curves for under correlated ground motions.

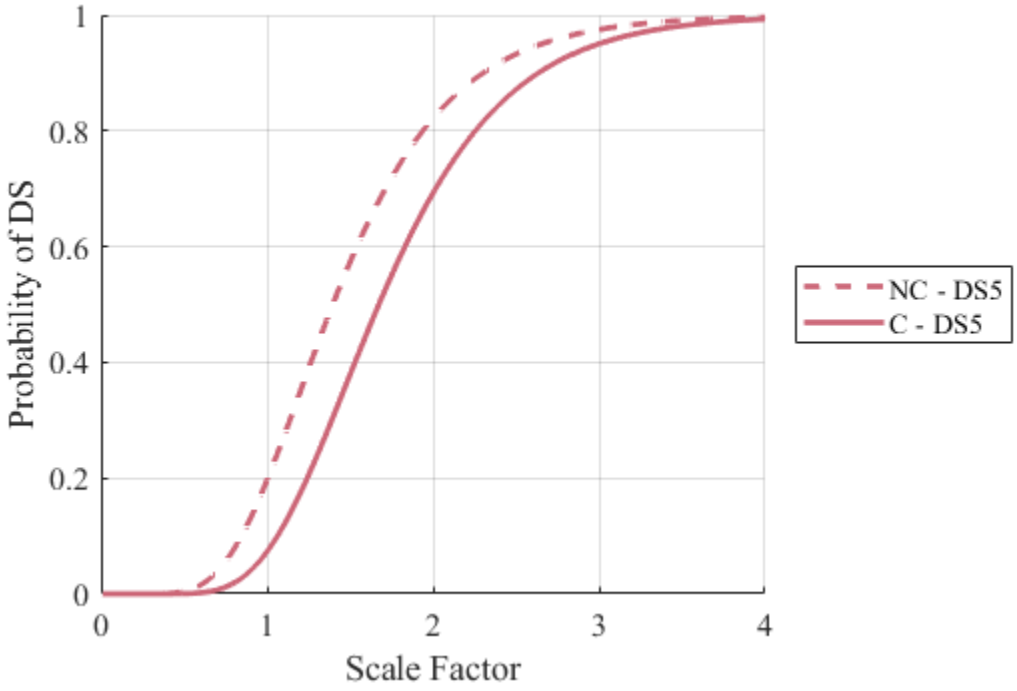

Figure 5.11 Typical bridge damage fragility curves for DS-5 under non-correlated and correlated ground motions.

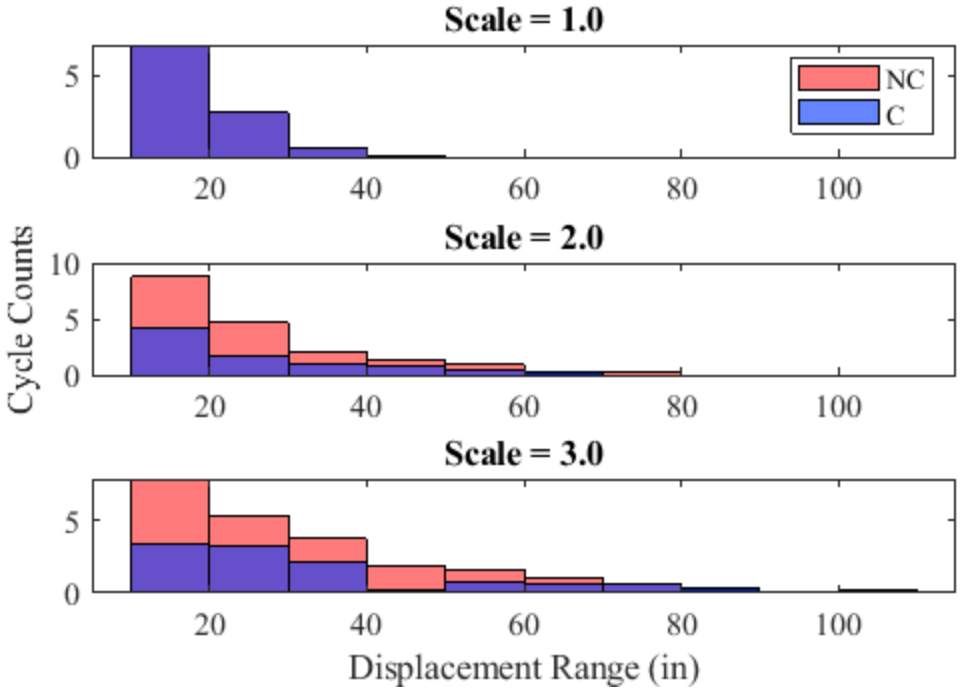

Figure 5.12 Comparison of average number of cycles under non-correlated (NC) and correlated (C) records at scale factors of 1.0, 2.0, 3.0.

6 CONCLUSIONS

This report focuses on developing fragility curves, with and without considering duration correlation, for a major toll bridge with a period of 1.6 seconds and a typical overpass with a period of 0.5 seconds. The first objective is to determine if considering duration correlation in ground motion selection appreciably changes the hazard input for analysis. Given this hazard change, the second goal is to evaluate changes in the fragility damage curves for the two bridges.

Ground motion duration is negatively correlated to intensity in the hazard analysis. The duration correlation is largest at shorter structural periods and decreases with increasing structural period. Multiple suites of ground motions were selected both with and without accounting for duration correlated to spectral acceleration. The first suite was chosen using magnitude, distance, other secondary earthquake parameters, and non-correlated durations and then scaled directly with values of 2, 2.5, 3, 3.5, 4, and 4.5. The second set of ground motions was formed by selecting six additional suites based on scaled hazard spectra considering the duration correlation. The bridge performance was compared using the fragility curves resulting from these sets of ground motions to assess the effect of correlation coefficients on the probability of reaching DS-3 and DS-5 for a major toll bridge and a typical highway overpass located in Southern California and in Northern California.

The performance of the bridges was evaluated by comparing the fragility curves of the model subject to the non-correlated and the duration correlated ground motions. The major toll bridge resulted in the median probability of reaching DS-3 and DS-5 at intensity values 29.2% and 37.4% larger when subject to the correlated suite of ground motions than those with the non-correlated suite. The overall bridge performance is based on a single worst-case component. However, the figures in section 4.4.3 show that other individual components follow the same trend and generally have lower damage probability when duration correlation is accounted in the hazard selection process. The performance of the typical highway bridge was evaluated by comparing the fragility curves for the model subject to the non-correlated suite of ground motion and the duration correlated ground motions. From the fragility curves, the median probability of DS-5 using the correlated ground motions occurs at a 17.3% higher scale factor than traditional IDA. This shift in the median probability shows that the non-correlated traditional IDA leads to an underestimation of the bridge performance at the major damage state.

The difference in the duration correlation for both bridges can be observed by comparing the correlated duration values in Table 4 and Table 18. The major toll bridge has a small reduction in duration with each increasing scale, due to a large fundamental period, with a -0.66 seconds difference in $D_{5\text{-}95}$ from a scale of 1.0 to scale of 4.5. The typical highway overpass, however, has a larger reduction of -2.71 seconds in $D_{5\text{-}95}$ from a scale of 1.0 to a scale of 4.5. The effect of this difference in duration correlation can be directly observed in the structural response by comparing Figure 4.18 and Figure 4.19 of the major toll bridge with Figure 5.12 of the typical highway bridge.

The difference in the number of cycles is significantly larger in the case of the typical highway overpass.

The case studies of both the major toll bridge and the typical highway overpass indicates a reduction in the damage probability when considering duration correlations. This suggests IDA without considering duration correlation underestimates the performance of both structural systems. A summary of the effects of both case studies is summarized in Table 26. Both sites have similar seismicity and soil type but differ in period and structural behavior. While the longer period of the toll bridge leads to smaller changes in duration when considering the correlation, it has lead rubber bearings which have strength deterioration with larger number of cycles. This results in both bridges having a change in performance. The typical highway overpass is influenced by the large duration correlation at its period while the major toll bridge with even a small correlation is heavily influenced by its structural behavior. This study shows that, while the magnitude of effects of incorporating ground motion duration correlation is influenced by both period and structural response, it is nontrivial in location with large ground motions.

Table 26 Increase in median DS intensity measure when duration correlation is considered for both case study bridges.

Damage state	Major toll bridge	Typical bridge
DS-3	29.2%	-
DS-5	37.4%	17.3%

REFERENCES

Abrahamson, N. (1992). Non-stationary spectral matching. *Seismological research letters,* 63**,** 30

Abrahamson, N. A. & Silva, W. J. (1996). Empirical ground motion models. *Report to Brookhaven National Laboratory,*

Abrahamson, N. A., Silva, W. J. & Kamai, R. (2014). Summary of the ASK14 Ground Motion Relation for Active Crustal Regions. *Earthquake Spectra,* 30**,** 1025-1055.10.1193/070913eqs198m

Afshari, K. & Stewart, J. P. (2016). Physically Parameterized Prediction Equations for Significant Duration in Active Crustal Regions. *Earthquake Spectra,* 32**,** 2057-2081.10.1193/063015eqs106m

Ancheta, T. D., Darragh, R. B., Stewart, J. P., Seyhan, E., Silva, W. J., Chiou, B. S.-J., Wooddell, K. E., Graves, R. W., Kottke, A. R., Boore, D. M., Kishida, T. & Donahue, J. L. (2014). NGA-West2 Database. *Earthquake Spectra,* 30**,** 989-1005.10.1193/070913eqs197m

Baker, J. W. (2015). Efficient Analytical Fragility Function Fitting Using Dynamic Structural Analysis. *Earthquake Spectra,* 31**,** 579-599.10.1193/021113eqs025m

Baker, J. W. & Jayaram, N. (2008). Correlation of Spectral Acceleration Values from NGA Ground Motion Models. *Earthquake Spectra,* 24**,** 299-317.10.1193/1.2857544

Barbosa, A. R., Ribeiro, F. L. A. & Neves, L. a. C. (2017). Influence of earthquake ground-motion duration on damage estimation: application to steel moment resisting frames. *Earthquake Engineering & Structural Dynamics,* 46**,** 27-49.https://doi.org/10.1002/eqe.2769

Bommer, J. J., Stafford, P. J. & Alarcón, J. E. (2009). Empirical Equations for the Prediction of the Significant, Bracketed, and Uniform Duration of Earthquake Ground Motion. *Bulletin of the Seismological Society of America,* 99**,** 3217-3233.10.1785/0120080298

Boore, D. M., Stewart, J. P., Seyhan, E. & Atkinson, G. M. (2014). NGA-West2 Equations for Predicting PGA, PGV, and 5% Damped PSA for Shallow Crustal Earthquakes. *Earthquake Spectra,* 30**,** 1057-1085.10.1193/070113eqs184m

Buckle, I. G. & Liu, H. Critical loads of elastomeric isolators at high shear strain. Proceedings of the third US-Japan Workshop on Earthquake Protective Systems for Bridges, 1994. 4-85, 4-99.

Caltrans (2019). Seismic Design Criteria - Version 2.0. *California Department of Transportation (Caltrans),*

Campbell, K. W. & Bozorgnia, Y. (2014). NGA-West2 Ground Motion Model for the Average Horizontal Components of PGA, PGV, and 5% Damped Linear Acceleration Response Spectra. *Earthquake Spectra,* 30**,** 1087-1115.10.1193/062913eqs175m

Chandramohan, R., Baker, J. W. & Deierlein, G. G. (2016). Quantifying the Influence of Ground Motion Duration on Structural Collapse Capacity Using Spectrally Equivalent Records. *Earthquake Spectra,* 32**,** 927-950.10.1193/122813eqs298mr2

Chiou, B. S.-J. & Youngs, R. R. (2014). Update of the Chiou and Youngs NGA Model for the Average Horizontal Component of Peak Ground Motion and Response Spectra. *Earthquake Spectra,* 30**,** 1117-1153.10.1193/072813eqs219m

Cornell, C. A. (1968). Engineering seismic risk analysis. *Bulletin of the Seismological Society of America,* 58**,** 1583-1606.10.1785/bssa0580051583

Fema-P695 2009. *Quantification of Building Seismic Performance Factors, FEMA-P695, prepared by the Applied Technology Council for the Federal Emergency Council,* Washington, D.C., nehrp.

Field, E. H., Biasi, G. P., Bird, P., Dawson, T. E., Felzer, K. R., D.D., J., K.M., J., Jordan, T. H., Madden, C., Michael, A. J., Milner, K. R., Page, M. T., Parsons, T., Powers, P. M., Shaw, B. E., Thatcher, W. R., Weldon, R. J. I. & Zeng, Y. 2013. Uniform California earthquake rupture forecast, version 3 (UCERF3) — The time-independent model. U.S. Geological Survey Open-File Report 2013–1165, 97 p., California Geological Survey Special Report 228, and Southern California Earthquake Center Publication 1792.

Hale, C., Abrahamson, N. & Bozorgnia, Y. 2018. Probabilistic Seismic Hazard Analysis Code Verification. *PEER Report 2018-03.* Pacific Earthquake Engineering Research Center, University of California, Berkeley, CA.

Hancock, J. & Bommer, J. J. (2006). A State-of-Knowledge Review of the Influence of Strong-Motion Duration on Structural Damage. *Earthquake Spectra,* 22**,** 827-845.10.1193/1.2220576

Hancock, J. & Bommer, J. J. (2007). Using spectral matched records to explore the influence of strong-motion duration on inelastic structural response. *Soil Dynamics and Earthquake Engineering,* 27**,** 291-299.https://doi.org/10.1016/j.soildyn.2006.09.004

Hassan, A. L. & Billah, A. H. M. M. (2020). Influence of ground motion duration and isolation bearings on the seismic response of base-isolated bridges. *Engineering Structures,* 222**,** 111129.https://doi.org/10.1016/j.engstruct.2020.111129

Iervolino, I., Manfredi, G. & Cosenza, E. (2006). Ground motion duration effects on nonlinear seismic response. *Earthquake Engineering & Structural Dynamics,* 35**,** 21-38.https://doi.org/10.1002/eqe.529

Kelly, J. M. & Konstantinidis, D. 2011. *Mechanics of rubber bearings for seismic and vibration isolation,* John Wiley & Sons.

Lilhanand, K. & Tseng, W. S. Development and application of realistic earthquake time histories compatible with multiple-damping design spectra. Proceedings of the 9th world conference on earthquake engineering, 1988. 819-824.

Maroney, B. H. & Chai, Y. H. Seismic Design and Retrofi tting of Reinforced Concrete Bridges. 2nd International Workshop, Earthquake Commission of New Zealand, 1994 Queenstown, New Zealand.

Mckenna, F., Scott, M. H. & Fenves, G. L. (2010). Nonlinear Finite-Element Analysis Software Architecture Using Object Composition. 24**,** 95-107.doi:10.1061/(ASCE)CP.1943-5487.0000002

Moehle, J. & Deierlein, G. G. A framework methodology for performance-based earthquake engineering. 13th World Conference on Earthquake Engineering, 2004.

Priestley, M. & Park, R. (1987). Strength and ductility of concrete bridge columns under seismic loading. *Structural Journal,* 84**,** 61-76

Raghunandan, M. & Liel, A. B. (2013). Effect of ground motion duration on earthquake-induced structural collapse. *Structural Safety,* 41**,** 119-133.https://doi.org/10.1016/j.strusafe.2012.12.002

Saini, A. & Saiidi, M. 2014. *Probabilistic damage control approach for seismic design of bridge columns*, California Department of Transportation.

Shome, N., Cornell, C. A., Bazzurro, P. & Carballo, J. E. (1998). Earthquakes, Records, and Nonlinear Responses. *Earthquake Spectra,* 14**,** 469-500.10.1193/1.1586011

Tremblay, R. (2003). Achieving a stable inelastic seismic response for multi-story concentrically braced steel frames. *Engineering Journal,* 40**,** 111-129

Vamvatsikos, D. & Cornell, C. A. (2002). Incremental dynamic analysis. *Earthquake Engineering & Structural Dynamics,* 31**,** 491-514.https://doi.org/10.1002/eqe.141

Vosooghi, A. & Saiidi, M. S. (2010). Seismic damage states and response parameters for bridge columns. *Special Publication,* 271**,** 29-46

Vosooghi, A. & Saiidi, M. S. (2012). Experimental fragility curves for seismic response of reinforced concrete bridge columns. *ACI Structural Journal,* 109**,** 825

APPENDIX A

A.1 INDIVIDUAL CORRELATION RELATIONSHIPS

This section includes supplementary figures to Chapter 2 for individual normalized correlation coefficients.

Table A.1.1. Coefficients for calculating duration correlation for ASK14 between the three DPE's

Coefficient	AS96			B09			AS16	
	$D_{5\text{-}75\%}$	$D_{5\text{-}95\%}$ (T < 0.2 sec)	$D_{5\text{-}95\%}$ (T ≥ 0.2 sec)	$D_{5\text{-}75\%}$	$D_{5\text{-}95\%}$ (T < 0.2 sec)	$D_{5\text{-}95\%}$ (T ≥ 0.2 sec)	$D_{5\text{-}75\%}$	$D_{5\text{-}95\%}$
T_2	0.2	0.2		0.2	0.2	0.2	0.02	0.02
T_3	0.2	0.4		0.04	0.4		11	0.2
ρ_0	-0.28514	-0.204103		-0.281047	-0.242399		-0.515151	-0.491436
x_1	0.3295	0.517949643	0.3396	0.312	0.5101	0.3521	0.4623	0.3329
x_2	0.068727949	0.065	0.0341	0.0715	0.064	0.0547	0.2256	0.2242
x_3	0.105	0.105	0.105	0.105	0.105	0.105	0.1132	0.15
x_4	100	100	100	100	100	100	192.3409	229.889
x_5	5	5	5	5	5	5	8.6857	4.5895
x_6	0.0099	0.0099	0.0099	0.0099	0.0099	0.0099	0.0283	-0.0398
x_7	0.2	0.2	0.2	0.2	0.2	0.2	0.20005	0.20005
x_8	0.8	0.25	0.5	0.6	0.601	0.852	0.0448	-0.75

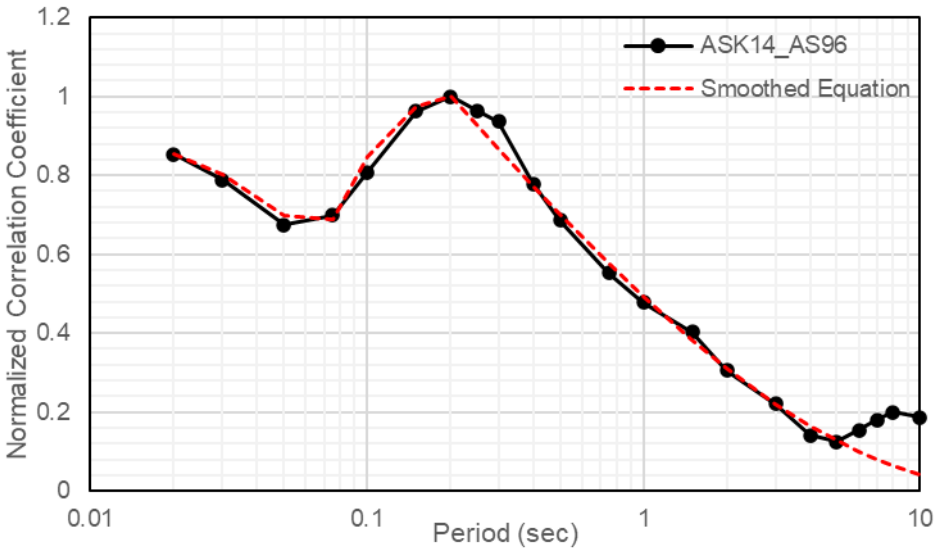

Figure A.1.1. ASK14 and AS96 correlation for $D_{5\text{-}75\%}$

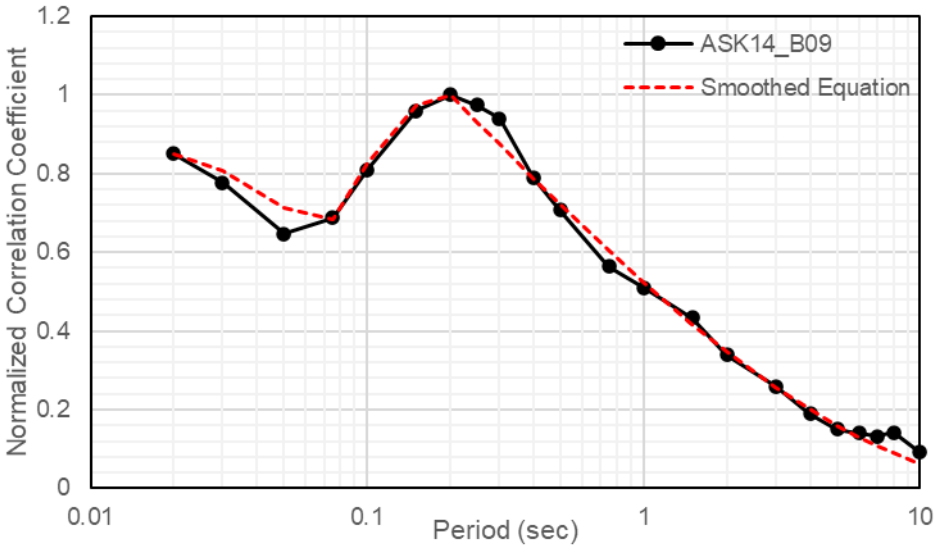

Figure A.1.2. ASK14 and B09 correlation for $D_{5\text{-}75\%}$

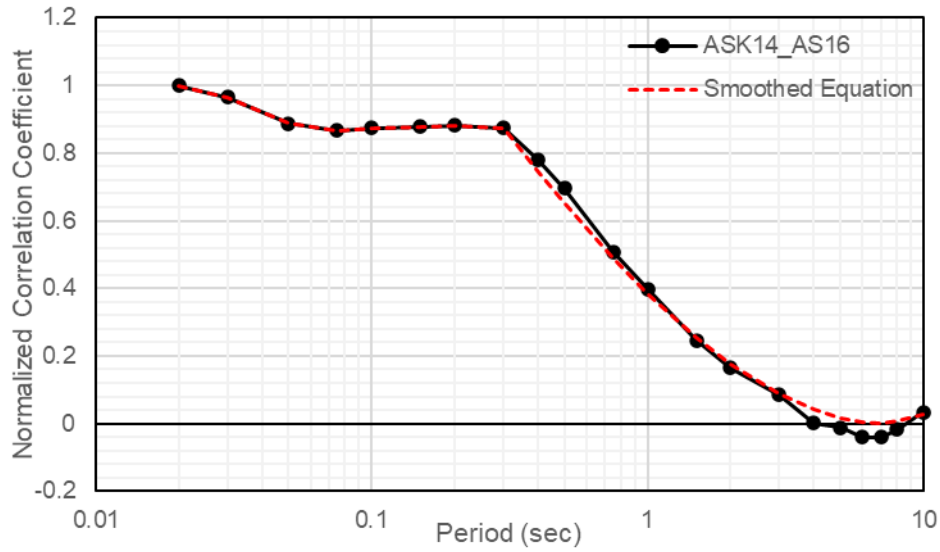

Figure A.1.3. ASK14 and AS16 correlation for $D_{5\text{-}75\%}$

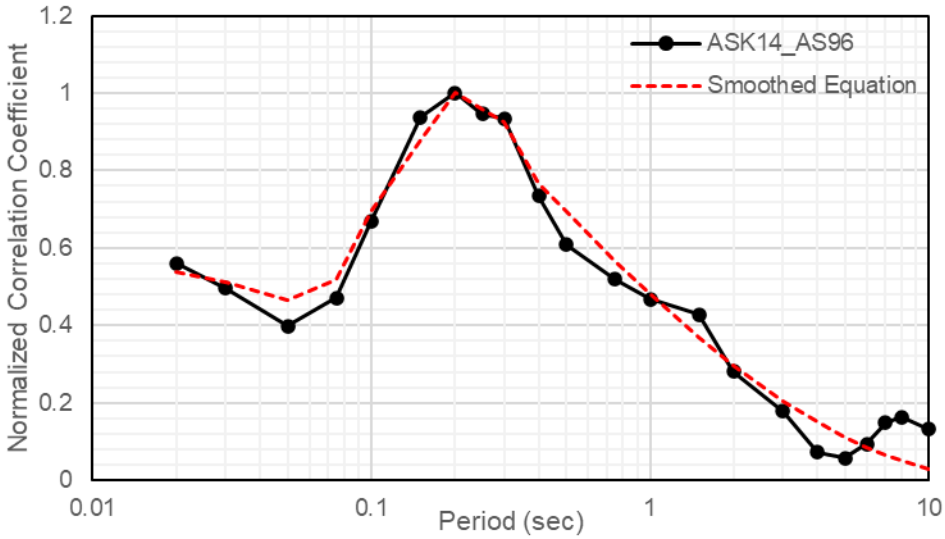

Figure A.1.4. ASK14 and AS96 correlation for $D_{5\text{-}95\%}$

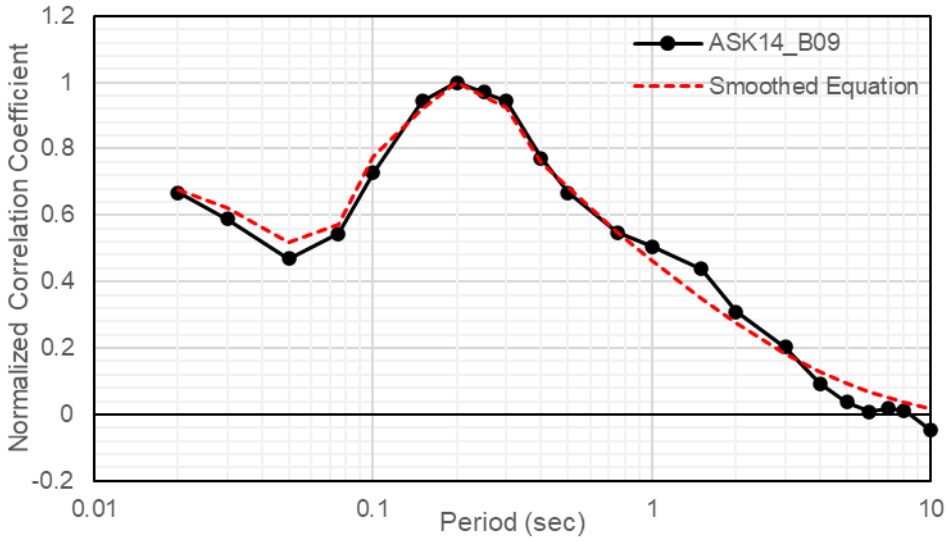

Figure A.1.5. ASK14 and B09 correlation for $D_{5\text{-}95\%}$

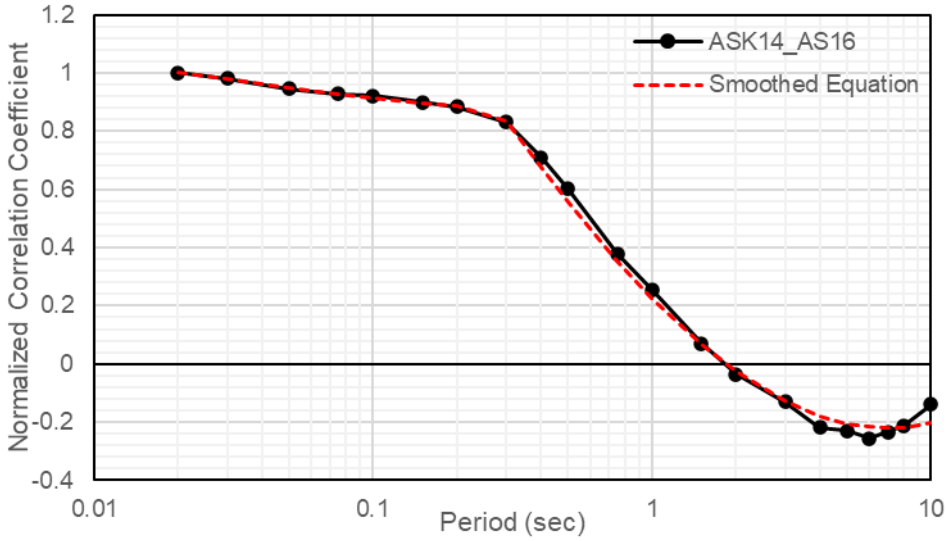

Figure A.1.6. ASK14 and AS16 correlation for D5-95%

Table A.1.2. Coefficients for calculating duration correlation for BSSA14 between the three DPE's

Coefficient	AS96		B09		AS16			
	$D_{5\text{-}75\%}$	$D_{5\text{-}95\%}$ ($T \leq 0.2$ sec)	$D_{5\text{-}75\%}$	$D_{5\text{-}95\%}$ ($T \leq 0.2$ sec)	$D_{5\text{-}75\%}$ ($T < 0.3$ sec)	$D_{5\text{-}75\%}$ ($T \geq 0.3$ sec)	$D_{5\text{-}95\%}$ ($T < 0.3$ sec)	$D_{5\text{-}95\%}$ ($T \geq 0.3$ sec)
T_2	0.01	0.01	0.01	0.04	0.01		0.02	
T_3	0.2	0.075	0.2	0.4	0.75		0.2	
ρ_0	-0.2434	-0.1123	-0.2792	-0.1978	-0.420438		-0.420438	
x_1	0.0244	0.3000	0.3630	0.3000	0.29	0.29	0.324	0.324
x_2	0.1577	0.0919	0.1815	0.0950	0.21	0.26	0.24	0.27
x_3	0.1715	0.2700	0.1535	0.2600	0.094	0.094	0.095	0.095
x_4	104.2162	46.2400	138.5398	60.0000	547	547	163.058	163.058
x_5	4.6886	2.8838	7.0838	5.0000	28.42	28.42	8.085	8.085
x_6	0.0167	0.0148	0.0187	0.0147	0.039932	0.025	0.0188	0
x_7	0.2001	0.2100	0.2001	0.2100	0.21	0.21	0.21	0.21
x_8	-11.7363	-0.0175	0.0089	-0.0170	-0.545	-0.545	-0.883	-0.883

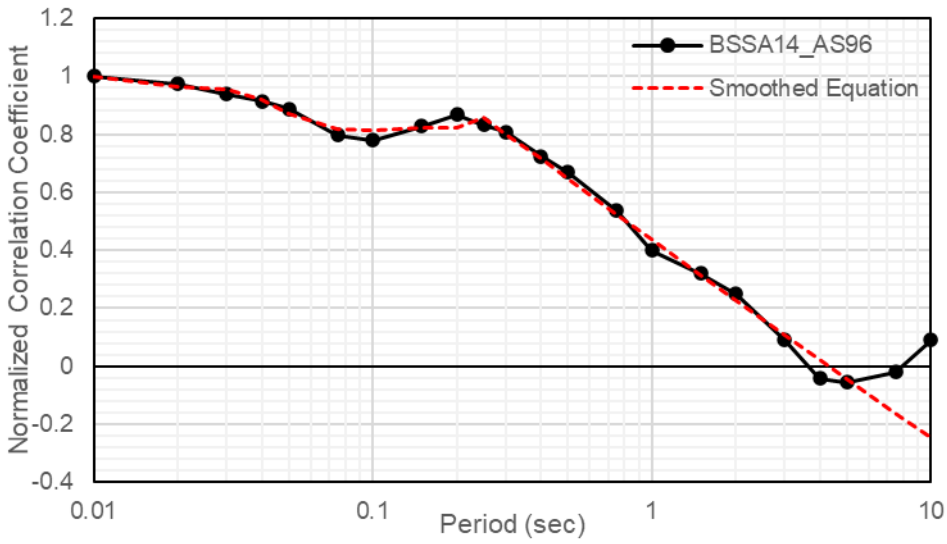

Figure A.1.7. BSSA14 and AS96 correlation for $D_{5\text{-}75\%}$

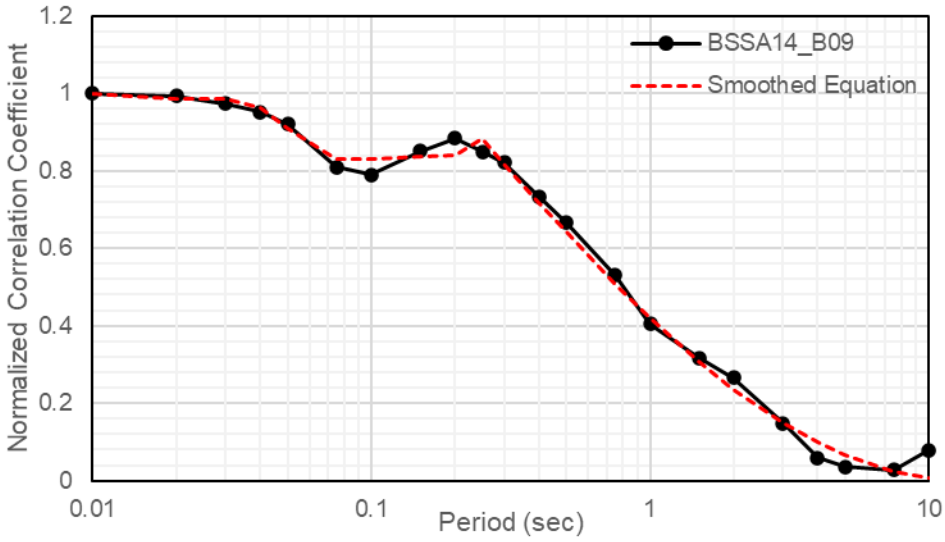

Figure A.1.8. BSSA14 and B09 correlation for $D_{5\text{-}75\%}$

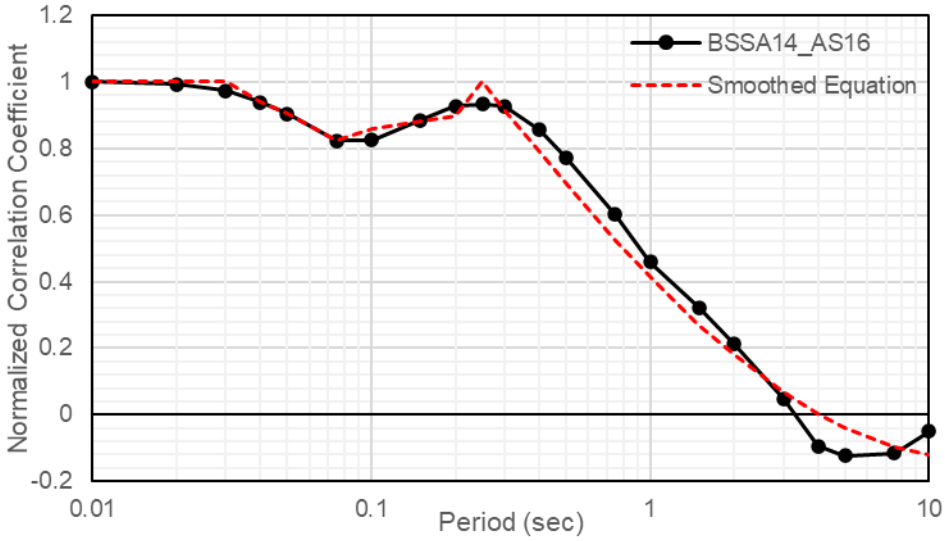

Figure A.1.9. BSSA14 and AS16 correlation for $D_{5\text{-}75\%}$

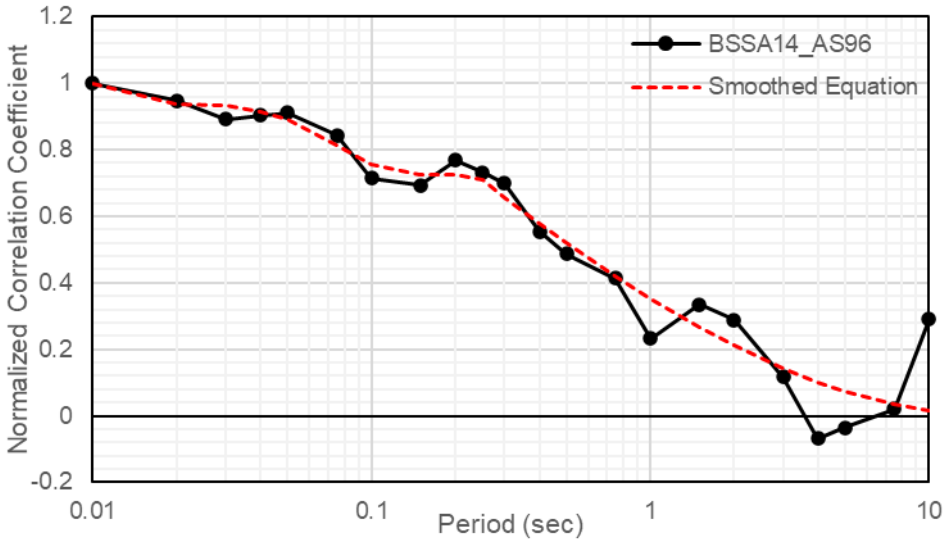

Figure A.1.10. BSSA14 and AS96 correlation fo $D_{5\text{-}95\%}$

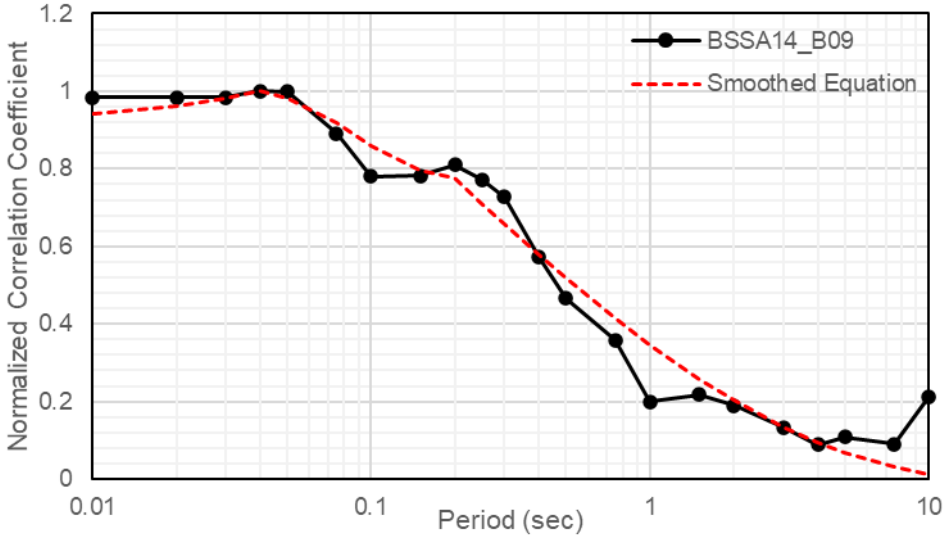

Figure A.1.11. BSSA14 and B09 correlation for $D_{5\text{-}95\%}$

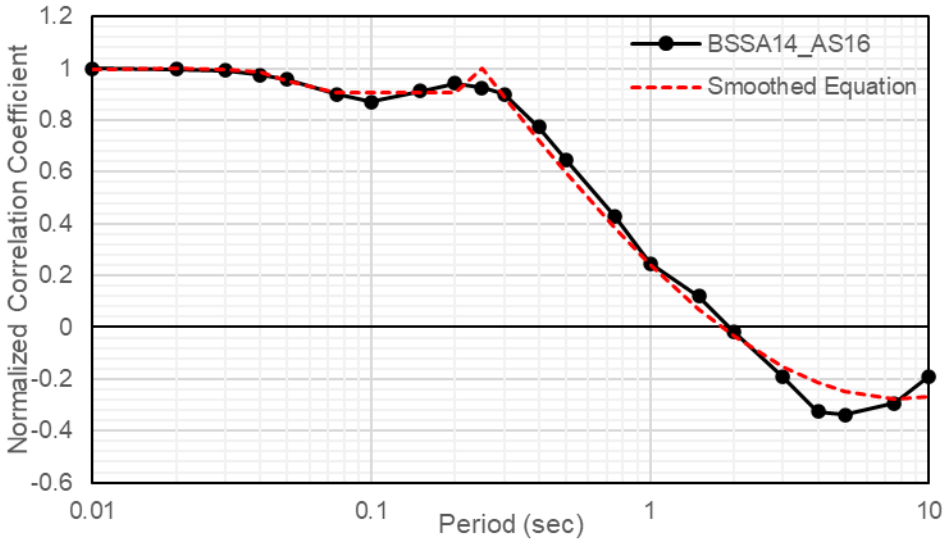

Figure A.1.12. BSSA14 and AS16 correlation for $D_{5\text{-}95\%}$

Table A.1.3. Coefficients for calculating duration correlation for BSSA14 between the three DPE's

Coefficient	AS96			B09			AS16	
	$D_{5\text{-}75\%}$ ($T < 1$ sec)	$D_{5\text{-}75\%}$ ($T \geq 1$ sec)	$D_{5\text{-}95\%}$ ($T \leq 0.2$ sec)	$D_{5\text{-}75\%}$ ($T < 1$ sec)	$D_{5\text{-}75\%}$ ($T \geq 1$ sec)	$D_{5\text{-}95\%}$	$D_{5\text{-}75\%}$	$D_{5\text{-}95\%}$
T_2	0.01		0.01	0.01		0.01	0.01	0.01
T_3	0.2		0.075	0.2		0.075	10	0.4
ρ_0	-0.336155		-0.203799	-0.322126		-0.255674	-0.562385	-0.255674
x_1	0.4688	0.1601	0.4260	0.4514	0.1524	0.3600	0.3188	0.4600
x_2	0.2079	0.0098	0.1870	0.1968	0.0046	0.1570	0.1550	0.1770
x_3	0.0715	0.1000	0.0539	0.0753	0.0790	0.0630	0.0939	0.0780
x_4	1408	1400	1398	1410	1400	1506	1497	186
x_5	50.8939	51.1183	51.3400	46.7987	51.1400	46.4900	46.4224	8.3000
x_6	0.0300	0.0000	0.0300	0.0297	0.0300	0.0240	0.0238	0.0276
x_7	0.5000	0.0001	0.2100	0.2001	0.2100	0.2100	0.2001	0.2100
x_8	0.0010	0.0000	0.0011	0.0009	0.0011	0.0009	0.0009	0.1750

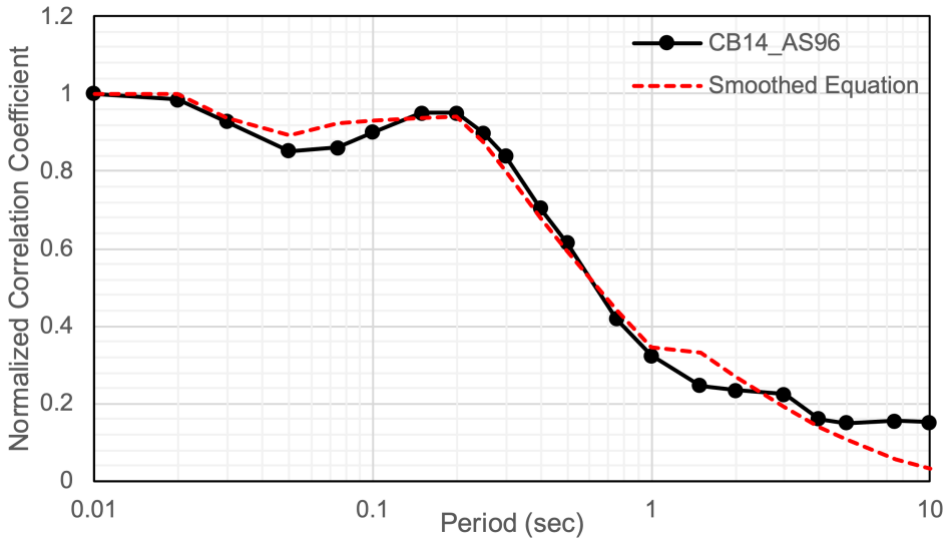

Figure A.1.13. CB14 and AS96 correlation for $D_{5\text{-}75\%}$

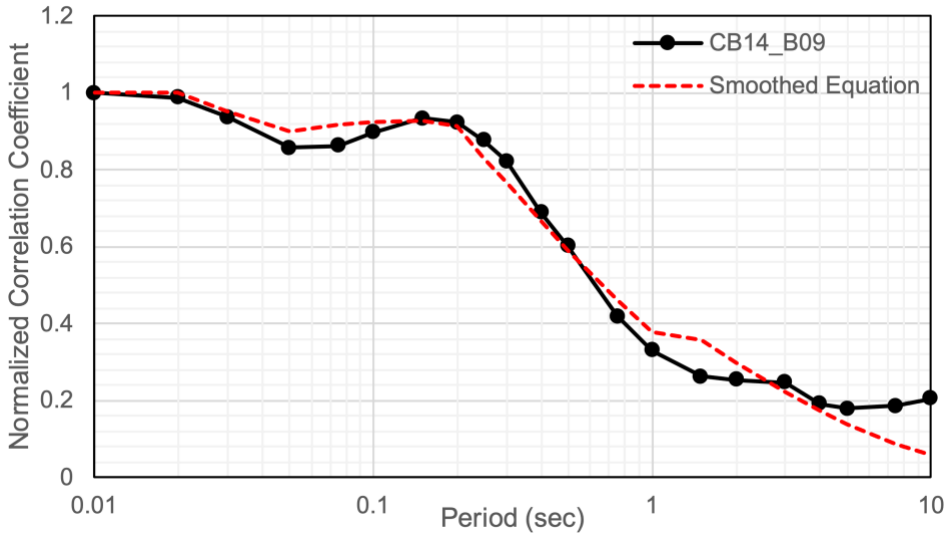

Figure A.1.14. CB14 and B09 correlation for $D_{5\text{-}75\%}$

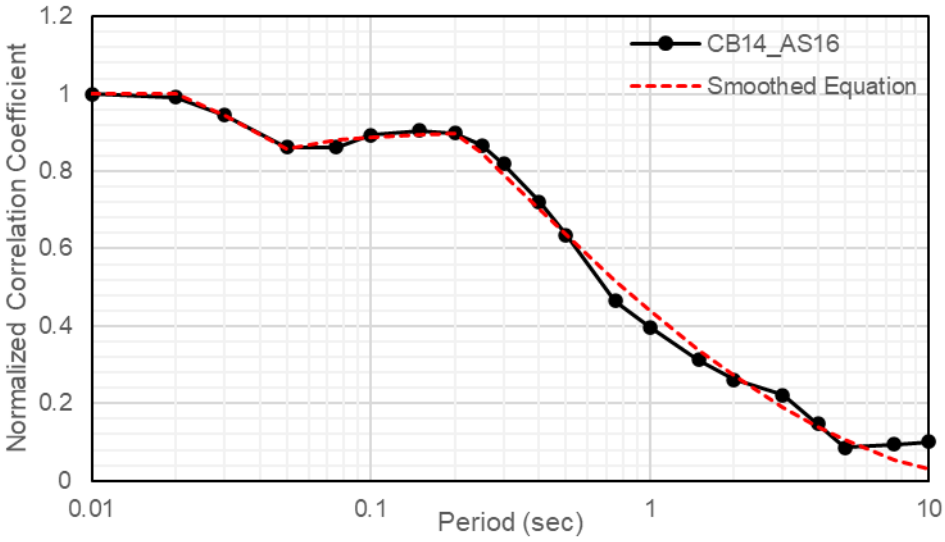

Figure A.1.15. CB14 and AS16 correlation for $D_{5\text{-}75\%}$

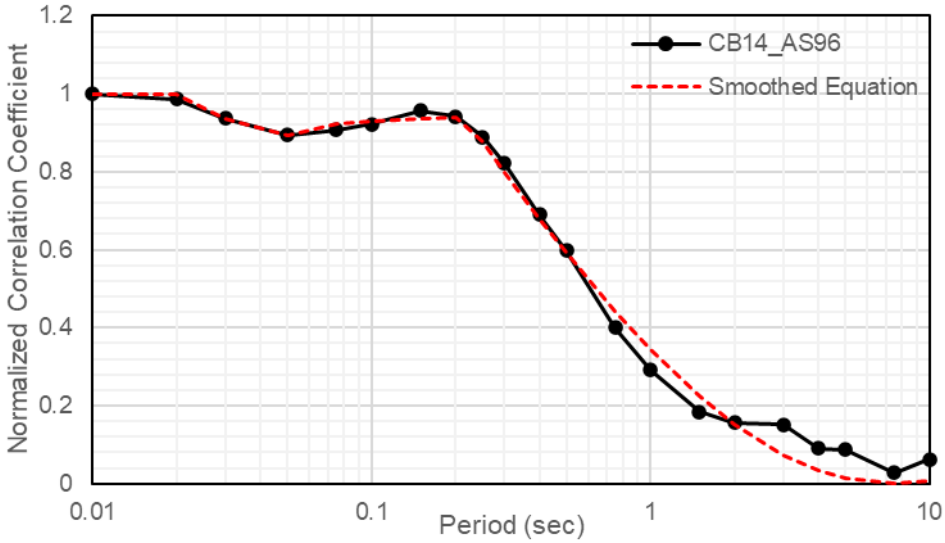

Figure A.1.16. CB14 and AS96 correlation for $D_{5\text{-}95\%}$

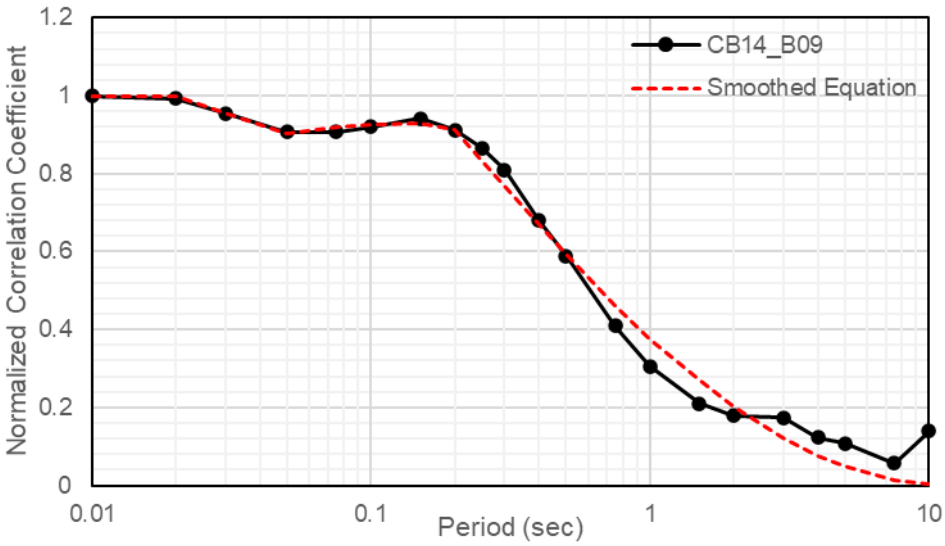

Figure A.1.17. CB14 and B09 for $D_{5\text{-}95\%}$

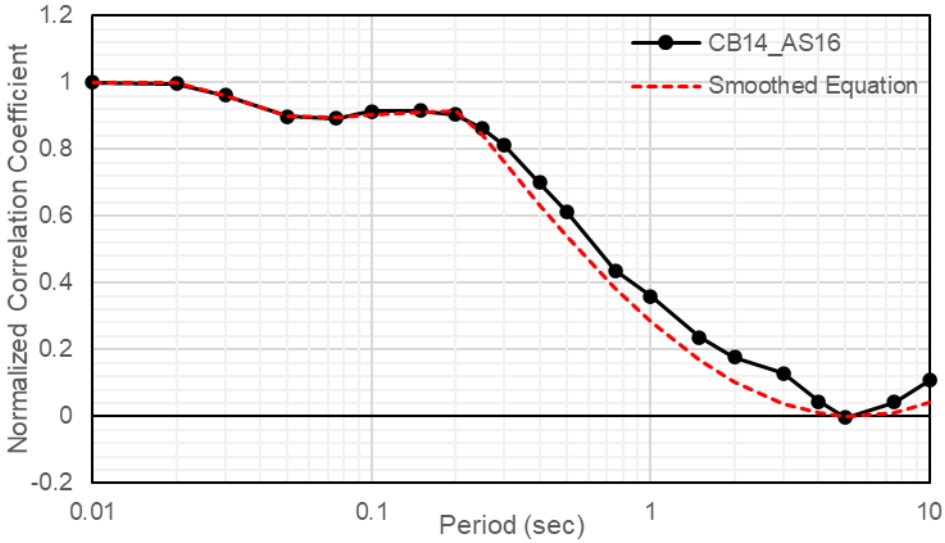

Figure A.1.18. CB14 and AS16 correlation for $D_{5\text{-}95\%}$

Table A.1.4. Coefficients for calculating duration correlation for BSSA14 between the three DPE's

Coefficient	AS96			B09			AS16			
	$D_{5\text{-}75\%}$ ($T < 7.5$ sec)	$D_{5\text{-}75\%}$ ($T \geq 7.5$ sec)	$D_{5\text{-}95\%}$	$D_{5\text{-}75\%}$ ($T < 5$ sec)	$D_{5\text{-}75\%}$ ($T \geq 5$ sec)	$D_{5\text{-}95\%}$ ($T > 0.2$ sec)	$D_{5\text{-}75\%}$ ($T < 0.3$ sec)	$D_{5\text{-}75\%}$ ($T \geq 0.3$ sec)	$D_{5\text{-}95\%}$ ($T < 1.5$sec)	$D_{5\text{-}95\%}$ ($T \geq 1.5$ sec)
T_2	0.01		0.01	0.01		0.01	0.01		0.01	
T_3	0.01		0.075	0.01		0.075	0.1		0.75	
ρ_0	-0.26283		-0.1496	-0.269975		-0.2105	-0.515948		-0.516563	
x_1	0.4159	0.4819	0.4570	0.4159	0.4819	0.4580	0.4160	0.4780	0.4580	0.4890
x_2	0.1858	0.1200	0.2200	0.1858	0.1200	0.2200	0.1860	0.2500	0.2200	0.4630
x_3	0.0949	0.0949	0.0580	0.0949	0.0987	0.0630	0.0950	0.1080	0.0630	0.0630
x_4	1345.8630	1345.8630	382.0000	1345.8630	374.0900	382.0000	1345.0000	345.0000	382.0000	382.0000
x_5	53.1738	53.1738	12.9800	53.1738	12.5176	12.9800	53.1700	17.3500	12.9800	12.9800
x_6	0.0184	0.0184	0.0140	0.0184	0.0195	0.0190	0.0184	0.0250	0.0190	0.0190
x_7	0.2001	0.2001	0.2001	0.2001	0.2001	0.2100	0.2100	0.2100	0.2100	0.2100
x_8	-0.0037	-0.0037	-0.2200	-0.0037	0.2055	-0.2204	-0.0040	0.0230	-0.2200	-0.8590

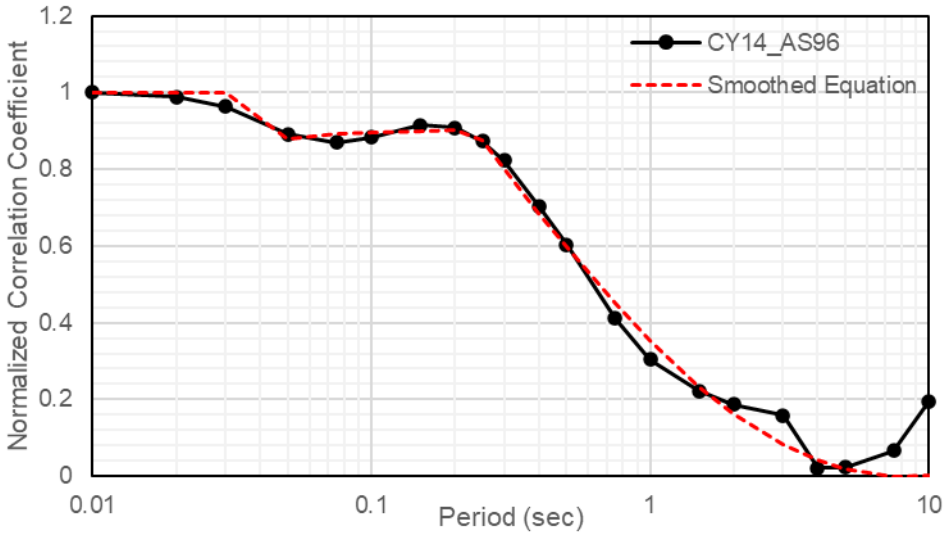

Figure A.1.19. CY14 and AS95 correlation for $D_{5\text{-}75\%}$

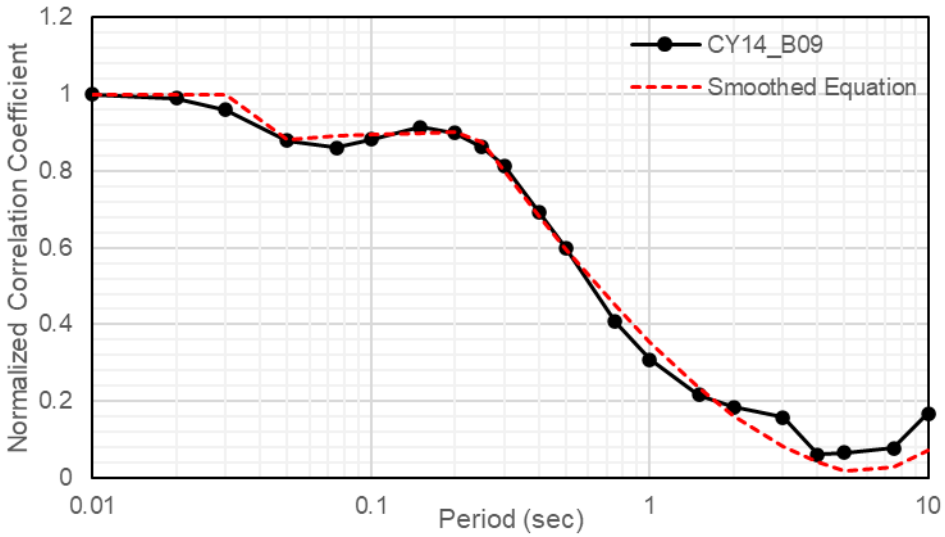

Figure A.1.20. CY14 and B09 correlation for $D_{5\text{-}75\%}$

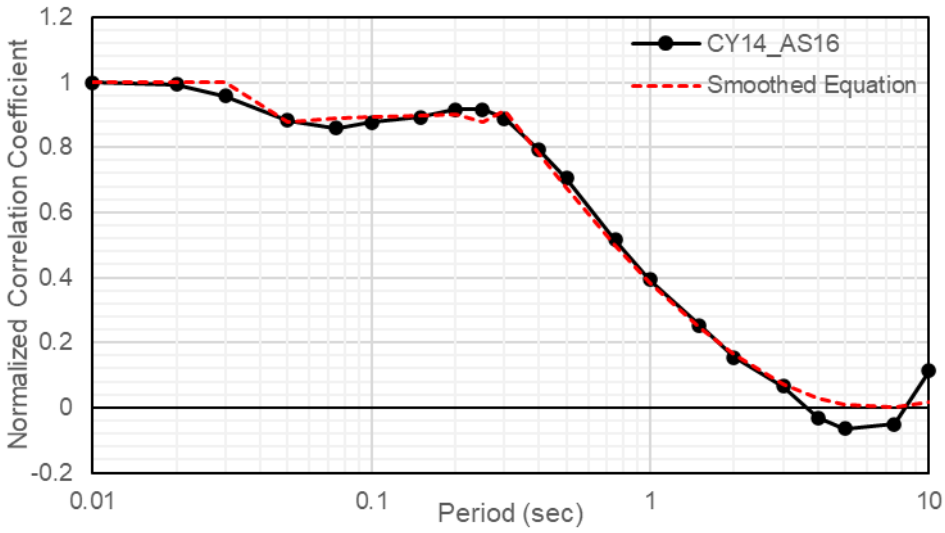

Figure A.1.21. CY14 to AS16 correlation for $D_{5\text{-}75\%}$

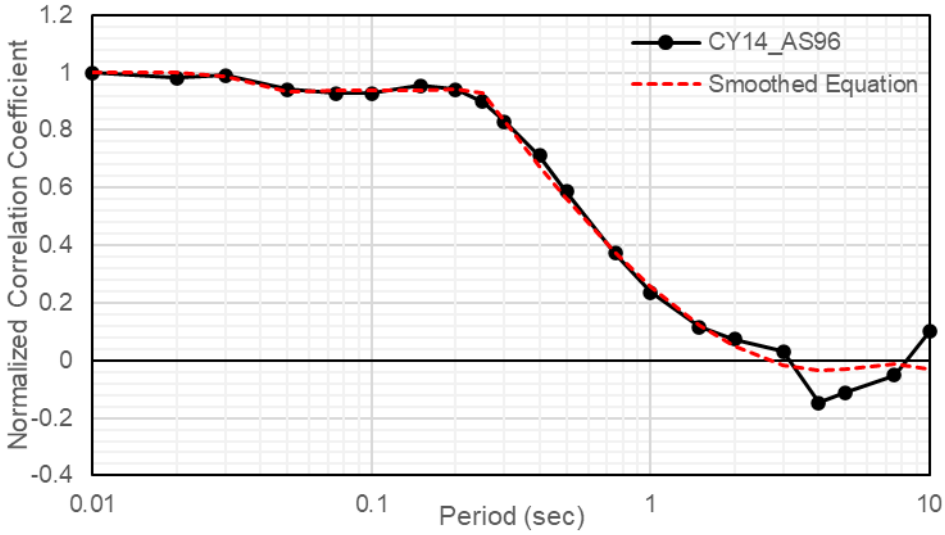

Figure A.1.22. CY14 and AS96 correlation for $D_{5\text{-}95\%}$

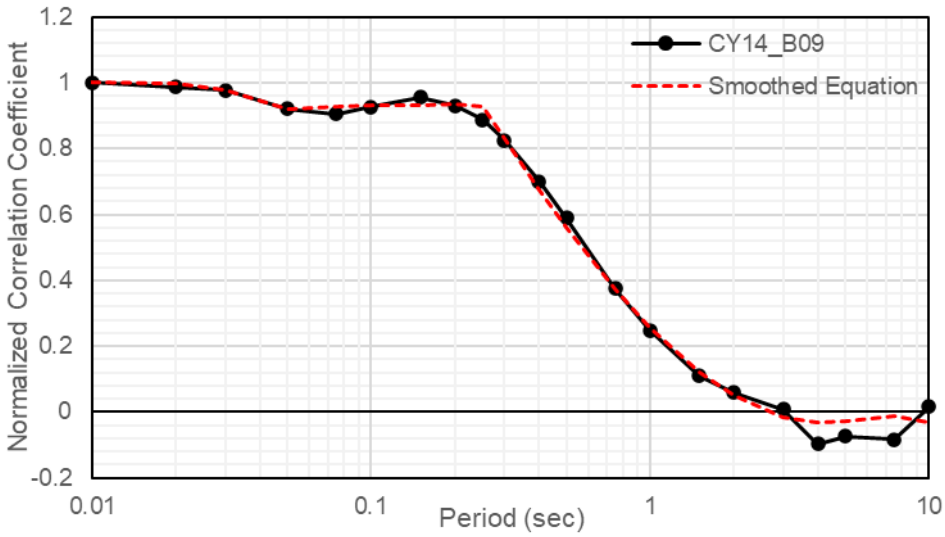

Figure A.1.23. CY14 and B09 correlation for $D_{5\text{-}95\%}$

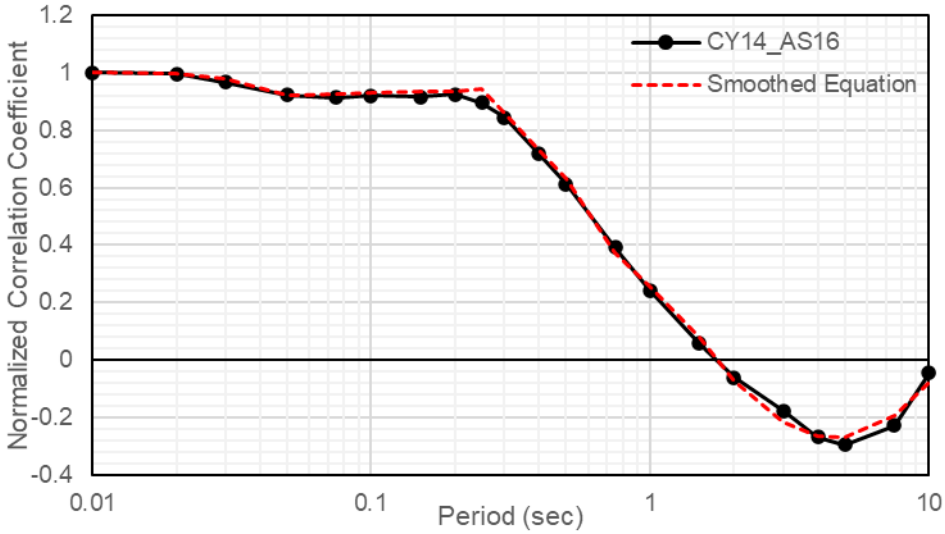

Figure A.1.24. CY14 and AS16 correlation for $D_{5\text{-}95\%}$

A.2 GROUND MOTION TABLES

The tables here show a summary of the ground motion records used in the correlated and non-correlated suites for analysis at each hazard level.

Table A.2.1 Non-correlated suite of ground motions for 2475-year hazard.

RSN	Earthquake Name	Station Name	Mw
828	Cape Mendocino	Petrolia	7
1158	Kocaeli_ Turkey	Duzce	7.5
1509	Chi-Chi_ Taiwan	TCU074	7.6
1787	Hector Mine	Hector	7.1
3748	Cape Mendocino	Ferndale Fire Station	7
3934	Tottori_ Japan	SMN002	6.6
3965	Tottori_ Japan	TTR008	6.6
4031	San Simeon_ CA	Templeton - 1-story Hospital	6.5
5818	Iwate_ Japan	Kurihara City	6.9
6890	Darfield_ New Zealand	Christchurch Cashmere High School	7
8063	Christchurch_ New Zealand	Christchurch Botanical Gardens	6.2

Table A.2.2 Correlated suite of ground motions for 2475 -year scale of 2.0 hazard.

RSN	Earthquake Name	Station Name	Mw
173	Imperial Valley-06	El Centro Array #10	**6.5**
1116	Kobe_ Japan	Shin-Osaka	**6.9**
1120	Kobe_ Japan	Takatori	**6.9**
1158	Kocaeli_ Turkey	Duzce	**7.5**
1492	Chi-Chi_ Taiwan	TCU052	**7.6**
3748	Cape Mendocino	Ferndale Fire Station	**7**
4874	Chuetsu-oki_ Japan	Oguni Nagaoka	**6.8**
4894	Chuetsu-oki_ Japan	Kashiwazaki NPP_ Unit 1: ground surface	**6.8**
6962	Darfield_ New Zealand	ROLC	**7**
8063	Christchurch_ New Zealand	Christchurch Botanical Gardens	**6.2**
8118	Christchurch_ New Zealand	Papanui High School	**6.2**

Table A.2.3 Correlated suite of ground motions for 2475 -year scale of 2.5 hazard.

RSN	Earthquake Name	Station Name	Mw
173	Imperial Valley-06	El Centro Array #10	**6.5**
1116	Kobe_ Japan	Shin-Osaka	**6.9**
1120	Kobe_ Japan	Takatori	**6.9**
1158	Kocaeli_ Turkey	Duzce	**7.5**
1492	Chi-Chi_ Taiwan	TCU052	**7.6**
3748	Cape Mendocino	Ferndale Fire Station	**7**
4229	Niigata_ Japan	NIGH12	**6.6**
4874	Chuetsu-oki_ Japan	Oguni Nagaoka	**6.8**
4894	Chuetsu-oki_ Japan	Kashiwazaki NPP_ Unit 1: ground surface	**6.8**
8063	Christchurch_ New Zealand	Christchurch Botanical Gardens	**6.2**
8118	Christchurch_ New Zealand	Papanui High School	**6.2**

Table A.2.4 Correlated suite of ground motions for 2475 -year scale of 3.0 hazard.

RSN	Earthquake Name	Station Name	Mw
173	Imperial Valley-06	El Centro Array #10	**6.5**
1116	Kobe_ Japan	Shin-Osaka	**6.9**
1120	Kobe_ Japan	Takatori	**6.9**
1158	Kocaeli_ Turkey	Duzce	**7.5**
1492	Chi-Chi_ Taiwan	TCU052	**7.6**
3964	Tottori_ Japan	TTR007	**6.6**
4229	Niigata_ Japan	NIGH12	**6.6**
4874	Chuetsu-oki_ Japan	Oguni Nagaoka	**6.8**
4894	Chuetsu-oki_ Japan	Kashiwazaki NPP_ Unit 1: ground surface	**6.8**
8063	Christchurch_ New Zealand	Christchurch Botanical Gardens	**6.2**
8118	Christchurch_ New Zealand	Papanui High School	**6.2**

Table A.2.5 Correlated suite of ground motions for 2475 -year scale of 3.5 hazard.

RSN	Earthquake Name	Station Name	Mw
173	Imperial Valley-06	El Centro Array #10	**6.5**
1116	Kobe_ Japan	Shin-Osaka	**6.9**
1120	Kobe_ Japan	Takatori	**6.9**
1158	Kocaeli_ Turkey	Duzce	**7.5**
1492	Chi-Chi_ Taiwan	TCU052	**7.6**
3964	Tottori_ Japan	TTR007	**6.6**
4117	Parkfield-02_ CA	Parkfield - Fault Zone 15	**6**
4228	Niigata_ Japan	NIGH11	**6.6**
4874	Chuetsu-oki_ Japan	Oguni Nagaoka	**6.8**
4894	Chuetsu-oki_ Japan	Kashiwazaki NPP_ Unit 1: ground surface	**6.8**
8063	Christchurch_ New Zealand	Christchurch Botanical Gardens	**6.2**

Table A.2.6 Correlated suite of ground motions for 2475 -year scale of 4.0 hazard.

RSN	Earthquake Name	Station Name	Mw
173	Imperial Valley-06	El Centro Array #10	**6.5**
1111	Kobe_ Japan	Nishi-Akashi	**6.9**
1116	Kobe_ Japan	Shin-Osaka	**6.9**
1158	Kocaeli_ Turkey	Duzce	**7.5**
1492	Chi-Chi_ Taiwan	TCU052	**7.6**
3964	Tottori_ Japan	TTR007	**6.6**
4117	Parkfield-02_ CA	Parkfield - Fault Zone 15	**6**
4228	Niigata_ Japan	NIGH11	**6.6**
4874	Chuetsu-oki_ Japan	Oguni Nagaoka	**6.8**
4894	Chuetsu-oki_ Japan	Kashiwazaki NPP_ Unit 1: ground surface	**6.8**
8063	Christchurch_ New Zealand	Christchurch Botanical Gardens	**6.2**

Table A.2.7 Correlated suite of ground motions for 2475 -year scale of 4.5 hazard.

RSN	Earthquake Name	Station Name	Mw
173	Imperial Valley-06	El Centro Array #10	**6.5**
768	Loma Prieta	Gilroy Array #4	**6.9**
1111	Kobe_ Japan	Nishi-Akashi	**6.9**
1116	Kobe_ Japan	Shin-Osaka	**6.9**
1158	Kocaeli_ Turkey	Duzce	**7.5**
3964	Tottori_ Japan	TTR007	**6.6**
4117	Parkfield-02_ CA	Parkfield - Fault Zone 15	**6**
4228	Niigata_ Japan	NIGH11	**6.6**
4874	Chuetsu-oki_ Japan	Oguni Nagaoka	**6.8**
4894	Chuetsu-oki_ Japan	Kashiwazaki NPP_ Unit 1: ground surface	**6.8**
8063	Christchurch_ New Zealand	Christchurch Botanical Gardens	**6.2**

A.3 MAJOR BRIDGE - NON-CORRELATED SETS – FRAGILITY CURVES

Supplementary fragility curves to section 4 are presented resulting from the non-correlated data set. The plots show the observed fractions of reaching a damage state against the scale factor of each suite of ground motions, along with the curve fitted to the data for each element. Included here fragility curves for isolated piers and non-isolated piers at DS-5.

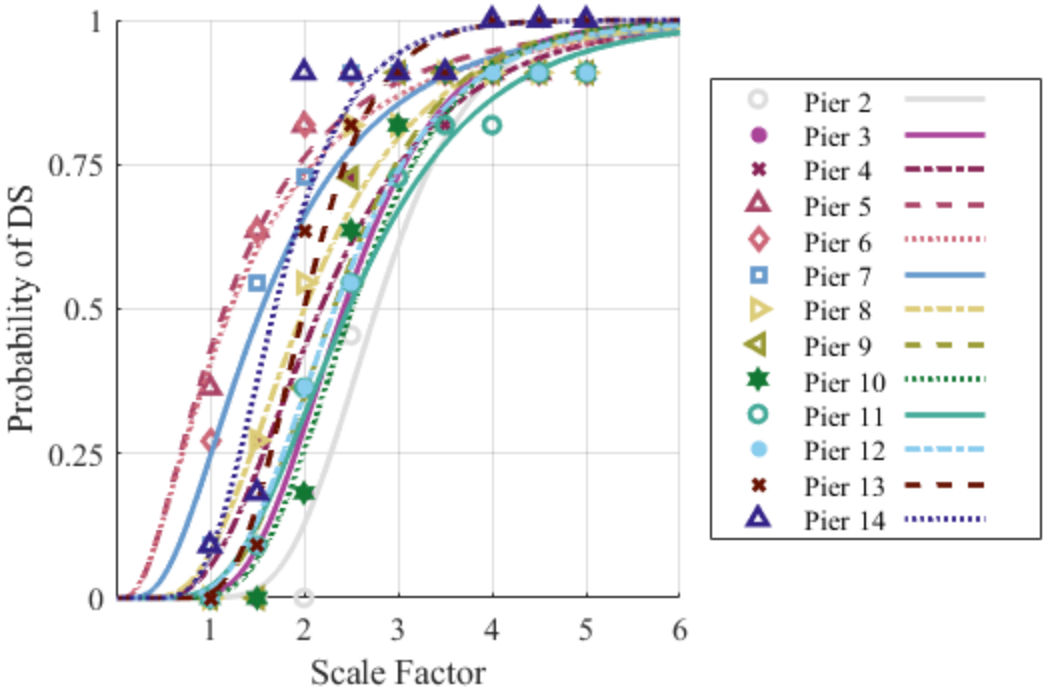

Figure A.3.1 DS-5 probability for bearings on each isolated pier with fitted fragility curves under non-correlated ground motions.

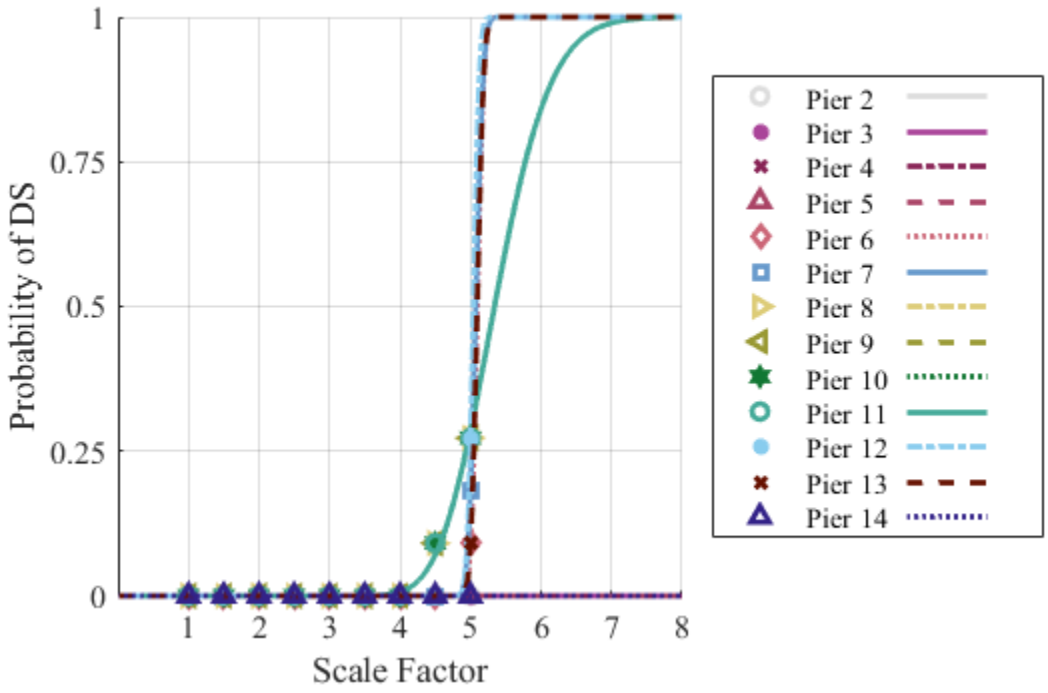

Figure A.3.2 Major toll bridge, isolated piers damage probability with fitted fragility curves for DS-5 under non-correlated ground motions.

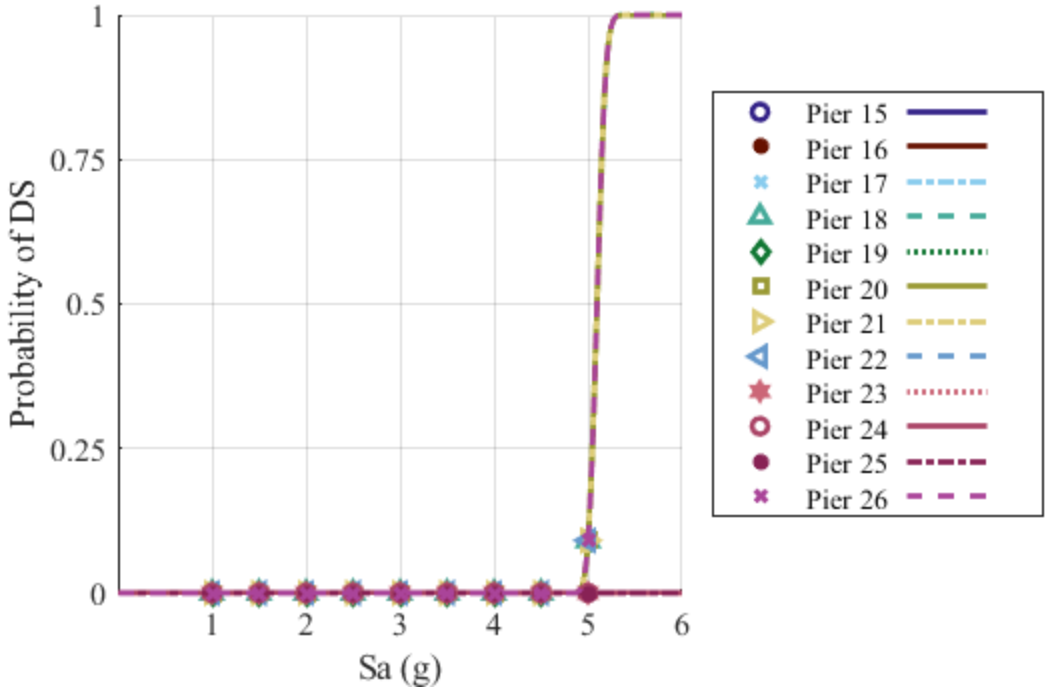

Figure A.3.3 Major toll bridge, non-isolated piers damage probability with fitted fragility curves for DS-5 under non-correlated ground motions.

A.4 MAJOR BRIDGE - CORRELATED SETS – FRAGILITY CURVES

Supplementary fragility curves to section 4 are presented resulting from the correlated data set. The plots show the observed fractions of reaching a damage state against the scale factor of each suite of ground motions, along with the curve fitted to the data for each element. Included here fragility curves for isolated piers and non-isolated piers at DS-3 and all fragility curves for DS-5.

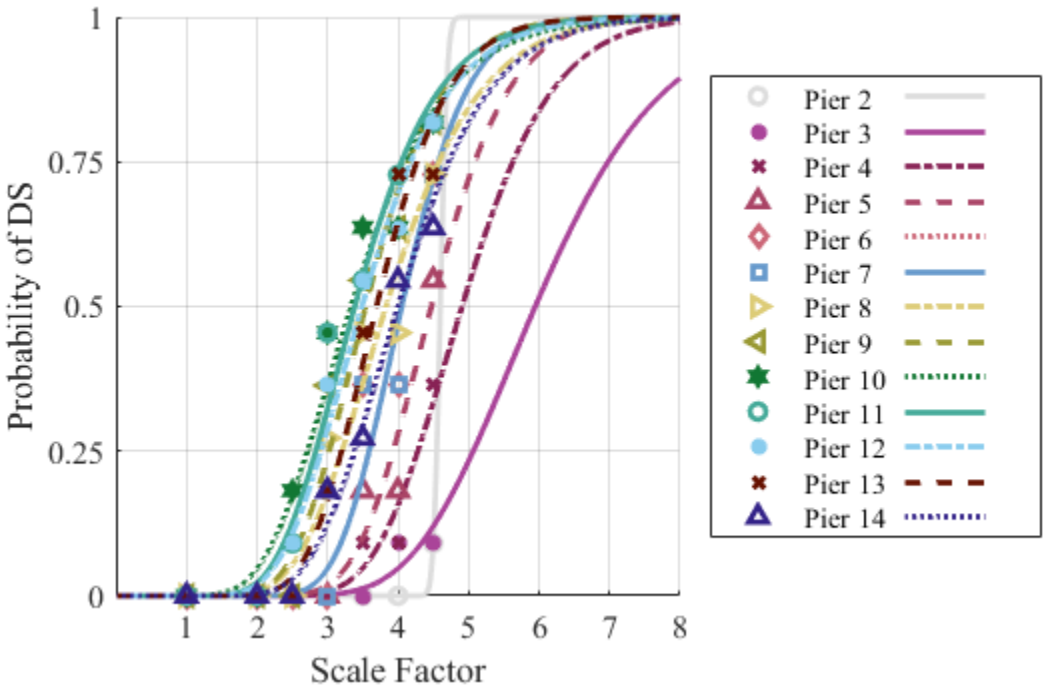

Figure A.4.1 Major toll bridge, isolated piers damage probability with fitted fragility curves for DS-3 under correlated ground motions.

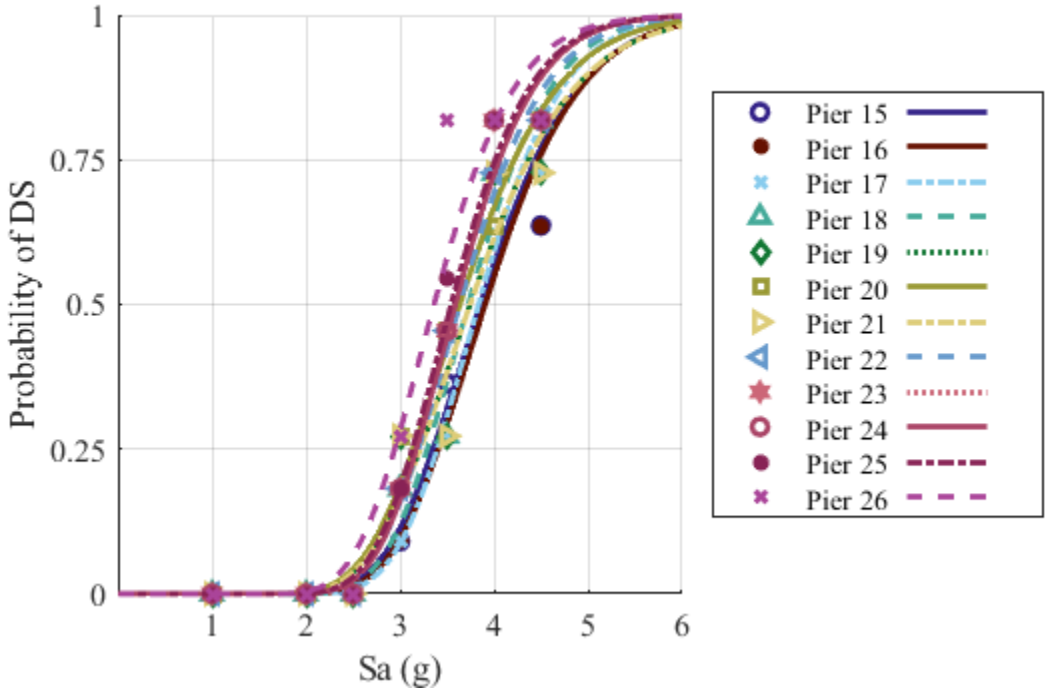

Figure A.4.2 Major toll bridge, non-isolated piers damage probability with fitted fragility curves for DS-3 under correlated ground motions.

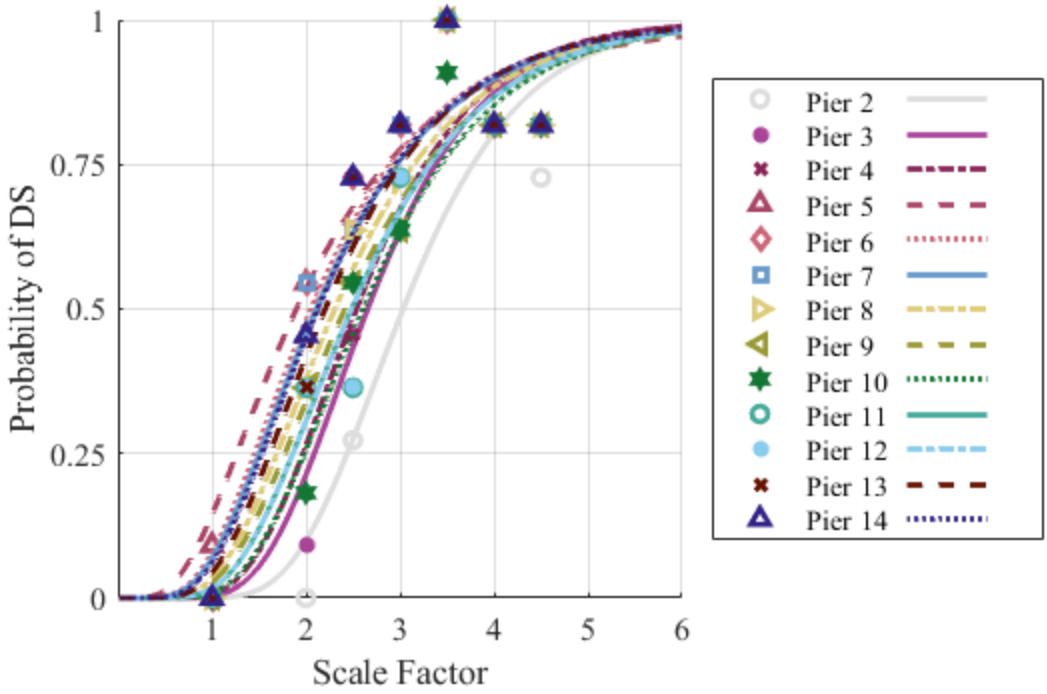

Figure A.4.3 Major toll bridge, bearings on each isolated piers with fitted fragility curves for DS-5 under correlated ground motions.

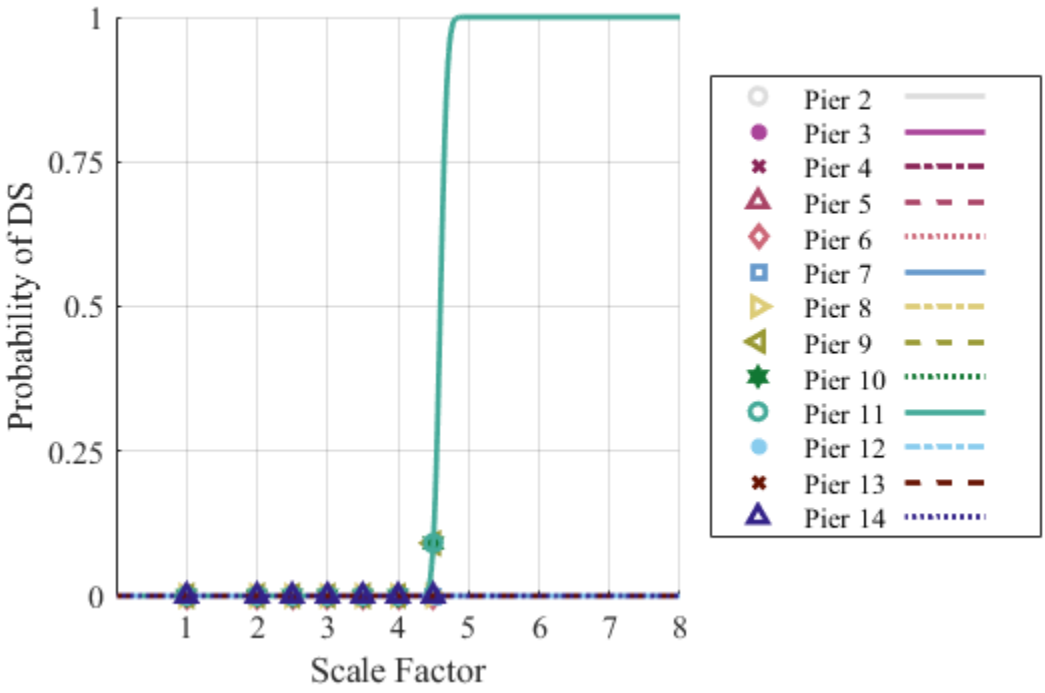

Figure A.4.4 Major toll bridge, isolated piers damage probability with fitted fragility curves for DS-5 under correlated ground motions.

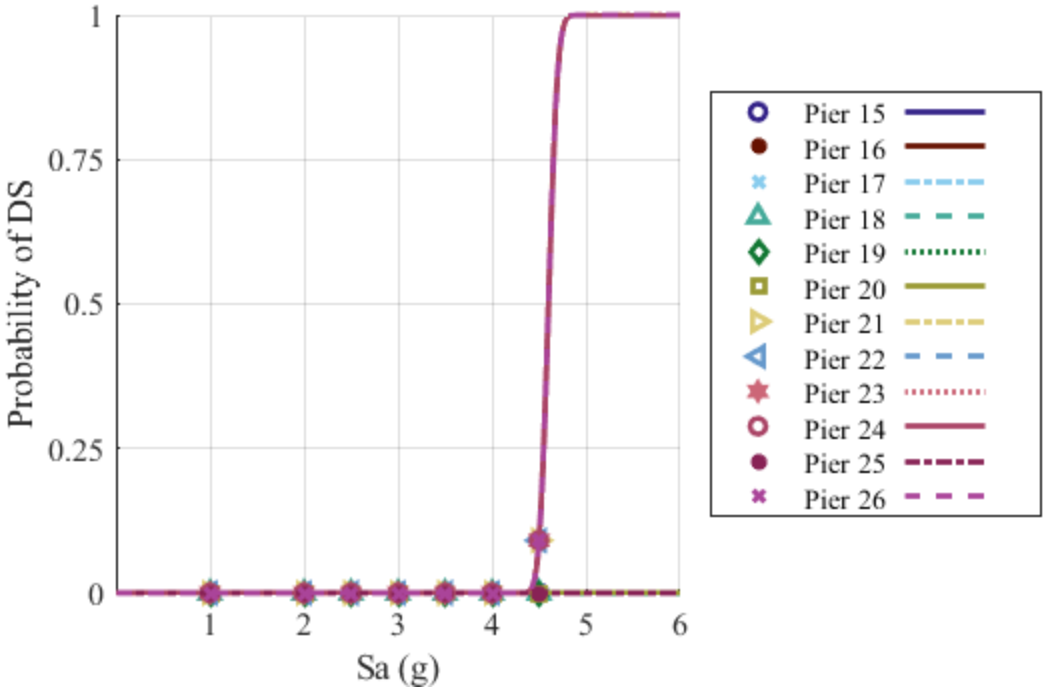

Figure A.4.5 Major toll bridge, non-isolated piers damage probability with fitted fragility curves for DS-5 under correlated ground motions.

The Pacific Earthquake Engineering Research Center (PEER) is a multi-institutional research and education center with headquarters at the University of California, Berkeley. Investigators from over 20 universities, several consulting companies, and researchers at various state and federal government agencies contribute to research programs focused on performance-based earthquake engineering.

These research programs aim to identify and reduce the risks from major earthquakes to life safety and to the economy by including research in a wide variety of disciplines including structural and geotechnical engineering, geology/seismology, lifelines, transportation, architecture, economics, risk management, and public policy.

PEER is supported by federal, state, local, and regional agencies, together with industry partners.

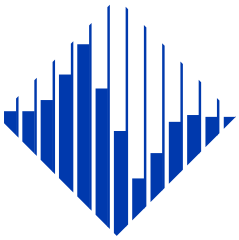

PEER Core Institutions

University of California, Berkeley (Lead Institution)
California Institute of Technology
Oregon State University
Stanford University
University of California, Davis
University of California, Irvine
University of California, Los Angeles
University of California, San Diego
University of Nevada, Reno
University of Southern California
University of Washington

Pacific Earthquake Engineering Research Center
University of California, Berkeley
325 Davis Hall, Mail Code 1792
Berkeley, CA 94720-1792
Tel: 510-642-3437
Email: peer_center@berkeley.edu

ISSN 2770-8314
https://doi.org/10.55461/PJPA6337